Chapter 16

WATER VAPOR, PRECIPITATION, CLOUDS, AND FOG

Section 16.1   D.D. Grantham, I.I. Gringorten, and A.J. Kantor
Section 16.2   R.M. Dyer, I.I. Gringorten, and P. Tattelman
Section 16.3   A.A. Barnes, E.A. Bertoni, I.D. Cohen, Capt. M. Glass, D.D. Grantham, I.I. Gringorten,
                 K.R. Hardy, Y. Izumi, A.J. Kantor, and J.I. Metcalf
Section 16.4   H.A. Brown and B.A. Kunkel

One of the most important constituents of the atmosphere is that all-pervasive substance, water, which appears in the solid state as snow, hail, frost, and cloud particles; in the liquid state as rain, clouds, fog, and dew; and in the gaseous state as water vapor. In addition to water, the atmosphere contains in suspension many types and sizes of aerosols of varying composition, including ions, salt, dust, smoke particles and other contaminants. This chapter deals with a variety of conditions or events that are related to atmospheric water content, including surface rainfall rates; the vertical distribution of precipitation intensity; drop-size distributions in rain, clouds and fog; types of cloud data; and water and water-vapor content in and out of clouds.

16.1 ATMOSPHERIC WATER VAPOR

There are various ways to express the water vapor content of the atmosphere. The *dew point* is the temperature to which a parcel of air, at constant pressure and water vapor content, must be cooled for saturation to occur. Further cooling produces condensation to liquid water. Condensation could be delayed as the parcel is cooled below the dew point, in which case the air becomes supersaturated. When the air is supersaturated, the condensation of water vapor can take place abruptly and the released latent heat of vaporization will raise the air temperature. If the water vapor content is low enough, then the parcel of air might be cooled below 273 K until saturation with respect to ice occurs, at which point there usually is sublimation directly from water vapor into ice crystals. This temperature is called the *frost point*. Sometimes the air can be cooled below 273 K, to as low as 233 K without sublimation, but there could be condensation onto existing supercooled water drops. Because the saturation vapor pressure over water is greater than that over ice, the dew point for a given water vapor content is always less than the frost point. The frost point-dewpoint difference, although essentially zero at 273 K, becomes increasingly large as the temperature lowers.

Several other measures of water vapor content are related

in a one-to-one correspondence to the dew point. Table 16-1 shows this correspondence between dew point and frost point, vapor pressure, and mixing ratio. The table also gives the absolute humidity (vapor density) corresponding to the other measures when the air is saturated.

In a unit volume of air, the water vapor exerts a *vapor pressure*, which in itself is another measure of the water vapor content of the air. When the air is saturated, the vapor pressure is a direct function of air temperature.

The *absolute humidity* is the mass of water vapor in a unit volume of air; it is actually the water vapor density within the air. The Gas Law shows that at a given air temperature, there is a *saturation water vapor content* per unit volume that the air can hold, which roughly doubles for each 10 K increase of air temperature. As a consequence of the Gas Law, an isobaric increase of the temperature will decrease the absolute humidity (vapor density) while the other measures in Table 16-1 remain the same.

If the mass of water vapor is given in proportion to the mass of the ambient dry air, typically in grams per kilogram, the resulting measure is called the *mixing ratio*. To relate mixing ratio to the other measures of water vapor content, the atmospheric pressure must be given. When the mixing ratio remains constant, as it does in adiabatic lifting of unsaturated air, the dew point will decrease with increasing altitude.

Relative humidity is the ratio of the actual vapor pressure of the air to the saturation vapor pressure at the ambient air temperature; it is given in percent. Relative humidity can be derived with sufficient accuracy as the corresponding ratio of the mixing ratio to saturation mixing ratio. At a relative humidity of 100% the dew point is equal to the ambient temperature. This can occur by the addition of moisture into the air and/or by the decrease of temperature to the dew point. Thus, relative humidity usually varies considerably during the course of a day, increasing during the cool of the night and decreasing in the heat of the day.

Precipitable water, W, is the amount of water contained in a vertical air column of unit cross-section extending between two specified levels. While the physical unit is the

Table 16-1. The correspondence between the several measures of water vapor content (based on Smithsonian Meteorological Tables [List, 1968]).

Dew Point (K)	Frost Point (K)	Vapor Pressure (mb)	Absolute‡ Humidity (g/m³)	Mixing Ratio (g/kg) 1000 mb	850 mb	700 mb	500 mb	400 mb	100 mb	50 mb	10 mb	1 mb
313		7.378+1	5.119+1	4.98+1	5.941+1	7.361+1	1.080+2	1.411+2	*	*	*	*
308		5.624+1	3.963+1	3.725+1	4.427+1	5.456+1	7.910+1	1.020+2	8.008+2	*	*	*
303		4.243+1	3.038+1	2.769+1	3.282+1	4.029+1	5.786+1	7.399+1	4.590+2	*	*	*
298		3.167+1	2.305+1	2.044+1	2.417+1	2.959+1	4.219+1	5.363+1	2.886+2	*	*	*
293		2.337+1	1.730+1	1.495+1	1.766+1	2.156+1	3.059+1	3.870+1	1.899+2	5.462+2	*	*
288		1.704+1	1.283+1	1.083+1	1.278+1	1.557+1	2.201+1	2.775+1	1.279+2	3.217+2	*	*
283		1.227+1	9.399	7.762	9.146	1.113+1	1.569+1	1.973+1	8.707+1	2.024+2	*	*
278		8.719	6.797	5.495	6.471	7.870	1.107+1	1.389+1	5.946+1	1.314+2	*	*
273	273.0	6.108	4.847	3.839	4.519	5.492	7.710	9.664	4.049+1	8.659+1	9.764+2	*
268	268.6	4.215	3.407	2.644	3.112	3.780	5.300	6.637	2.739+1	5.728+1	4.533+2	*
263	264.1	2.863	2.358	1.794	2.110	2.562	3.590	4.492	1.834+1	3.779+1	2.495+2	*
258	259.6	1.912	1.605	1.197	1.408	1.709	2.393	2.993	1.213+1	2.474+1	1.470+2	*
253	255.1	1.2540	1.074	7.847−1	9.227−1	1.120	1.568	1.960	7.903	1.601+1	8.919+1	*
248	250.5	8.070−1	7.047−1	5.048−1	5.936−1	7.204−1	1.008	1.260	5.603	1.021+1	5.461+1	*
243	245.8	5.088−1	4.534−1	3.182−1	3.742−1	4.540−1	6.352−1	7.938−1	3.183	6.397	3.335+1	6.443+2
238	241.2	3.139−1	2.856−1	1.963−1	2.308−1	2.801−1	3.918−1	4.896−1	1.960	3.931	2.016+1	2.846+2
233	236.5	1.891−1	1.757−1	1.183−1	1.390−1	1.687−1	2.360−1	2.948−1	1.179	2.362	1.199+1	1.450+2
273.0	273	6.107	4.847	3.839	4.518	5.492	7.709	9.668	4.048+1	8.658+1	9.759+2	*
267.3	268	4.015	3.246	2.518	2.963	3.599	5.047	6.322	2.604+1	5.433+1	4.722+2	*
261.8	263	2.597	2.139	1.627	1.913	2.324	3.255	4.075	1.660+1	3.409+1	2.182+2	*
256.2	258	1.652	1.387	1.034	1.216	1.476	2.067	2.592	1.045+1	2.126+1	1.231+2	*
250.8	253	1.032	8.835−1	6.456−1	7.592−1	9.214−1	1.289	1.613	6.490	1.311+1	7.158+1	*
245.3	248	6.323−1	5.521−1	3.955−1	4.650−1	5.643−1	7.895−1	9.872−1	3.961	7.969	4.199+1	*
239.9	243	3.798−1	3.385−1	2.375−1	2.792−1	3.388−1	4.740−1	5.926−1	2.373	4.763	2.456+1	3.809+2
234.6	238	2.233−1	2.032−1	1.396−1	1.642−1	1.993−1	2.787−1	3.483−1	1.393	2.791	1.42+1	1.788+2
229.3	233	1.283−1	1.192−1	8.026−2	9.434−2	1.144−1	1.600−1	2.001−1	7.996−1	1.601	8.084	9.154+1
224.1	228	7.198−2	6.836−2	4.503−2	5.293−2	6.422−2	8.981−2	1.122−1	4.483−1	8.970−1	4.510	4.824+1
	223	3.935−2	3.821−2	2.463−2	2.895−2	3.512−2	4.910−2	6.135−2	2.450−1	4.901−1	2.457	2.548+1
	218	2.092−2	2.078−2	1.309−2	1.539−2	1.867−2	2.611−2	3.261−2	1.302−1	2.604−1	1.304	1.329+1
	213	1.080−2	1.098−2	6.761−3	7.947−3	9.640−3	1.347−2	1.684−2	6.723−2	1.344−1	6.725−1	6.791
	208	5.006−3	5.627−3	3.386−3	3.979−3	4.826−3	6.749−3	8.427−3	3.365−2	6.728−2	3.362−1	3.381
	203	2.615−3	2.784−3	1.639−3	1.926−3	2.336−3	3.265−3	4.076−3	1.628−2	3.254−2	1.627−1	1.631
	198	1.220−3	1.334−3	7.646−4	8.986−4	1.090−3	1.524−3	1.902−3	7.593−3	1.518−2	7.590−2	7.597−1
	193	5.472−4	6.138−4	3.423−4	4.023−4	4.882−4	6.828−4	8.530−4	3.406−3	6.810−3	3.404−2	3.405−1
	188	2.353−4	2.710−4	1.472−4	1.730−4	2.099−4	2.936−4	3.668−4	1.465−3	2.928−3	1.464−2	1.464−1
	183	9.672−5	1.144−4	6.051−5	7.111−5	8.629−5	1.207−4	1.508−4	6.020−4	1.204−3	6.016−3	6.016−2

‡At saturation only.
*Atmospheric saturation is not possible at this ambient temperature and pressure.

mass per unit area, it is commonly reported as the height at which the liquid would stand if it were all condensed in a vessel of the same unit cross-section as the air column. For example, a height of 1 cm corresponds to 1 gm/cm² of precipitable water.

A programmable computer can use a set of equations or algorithms to generate the numbers given in Table 16-1. Where T_D represents dew point (K), T_F frost point (K), e vapor pressure (mb), p atmospheric pressure (mb), ρ_v abso-lute humidity (g/m³) and r mixing ratio (g/kg), then in terms of the frost point, the vapor pressure is approximated by

$$\log_{10} e = -2485.0/T_F + 3.5665 \log_{10} T_F$$

$$- 0.0032098\ T_F + 2.0702 \quad (16.1)$$

In terms of the dew point, the vapor pressure is approximated by

$$\log_{10}e = -2949.1/T_D$$

$$- 5.0281 \log_{10}T_D + 23.832 \quad (16.2)$$

In terms of the vapor pressure and the air temperature T(K), the absolute humidity (g/m^3) is approximated by

$$\rho_v = 216.68 \ e/T . \quad (16.3)$$

This will be the same as in Table 16-1 for saturated air only.

In terms of the vapor pressure (mb) and the atmospheric pressure (mb), the mixing ratio (g/kg) is approximately by

$$r = 621.97 \ e/(p-e) . \quad (16.4)$$

16.1.1 Surface

Water vapor at the earth's surface has a range of more than three orders of magnitude. The maximum amount of water vapor that the atmosphere can contain is regulated by its temperature. However, the amount actually present in the atmosphere is a complex function of various atmospheric and geophysical features. The highest value of atmospheric water vapor, observed in the Persian Gulf, is a dew point of 307 K, translating to 38 g/m^3 of water vapor or a mixing ratio of about 35 g water vapor per kg dry air. For extremely cold air (213 K) the moisture content, at best, can be no more than 0.02 g/m^3, or, at sea level, 0.01 g water vapor per kg dry air. Even this amount, however, can be important in the transmission of infrared radiation over long path lengths.

Information on the distribution of water vapor in the northern hemisphere was collected in the *Atmospheric Humidity Atlas* [Gringorten et al., 1966], which maps surface mixing ratios and dew points from the 5th to the 95th percentile for the midseason months. Two atlases, for the northern and southern hemispheres [Crutcher and Meserve, 1970; Taljaard et al., 1969] have been published that include mean monthly dew points and standard deviations of the monthly averages.

Figure 16-1, taken from the *Atmospheric Humidity Atlas*, presents 95th percentile surface dew points in July to illustrate high values of dew points over the northern hemisphere. The peak values are found in the Persian Gulf above exceptionally warm waters. Over deserts the water vapor content is lower, and coupled with high temperatures, the relative humidity drops to as low as 5% or less. Figure 16-2, also from the *Atlas*, presents 5th percentile surface dew points in January to illustrate low moisture content during the coldest time of the year. As expected, the dew point is lowest in polar and subpolar regions, but it is also low on high mountains. On the other hand, relative humidity can be high since it would not require much moisture to saturate the air at low temperatures.

World-wide extremes of humidity and the diurnal cycles of humidity in several distinctive climates are presented in

Table 16-2. Diurnal cycle of dew point, temperature, relative humidity, and solar insolation associated with the 1% high operational extreme of moisture content (dew point 304 K) in a coastal desert location.

Time (LST)	Dew Point (K)	Temperature (K)	R.H. (%)	Insolation L/h
0000	302	304	88	0
0300	302	304	88	0
0600	302	304	88	4
0900	304	310	73	68
1200	304	313	63	93
1500	304	314	60	61
1800	304	310	69	1
2100	303	306	85	0

a Department of Defense Military Standard, *Climatic Extremes for Military Equipment* [U.S. DOD, 1973] and are further discussed in the background studies document [Sissenwine and Cormier, 1974]. Table 16-2 gives details of the diurnal cycle of humidity, temperature, and solar insolation associated with the upper 1% dew point (304 K) in a hot coastal climate. In this kind of weather the dew point remains nearly constant throughout 24 hours, while the relative humidity changes from nearly 90% to 60%, respectively, as the temperature climbs from 304 K in the morning to 314 K in the afternoon. Table 16-3 presents a repeated diurnal cycle for an extreme moisture-laden case of 30 days duration. The conditions are maritime, with temperatures 300 K to 303 K, dew points 299 K to 301 K and relative humidity at 91% to 94%. Table 16-4 presents a diurnal cycle that has high relative humidity associated with high temperature. This case differs from that in Table 16-2 by having less absolute humidity, less insolation and lower temperature, but greater relative humidity throughout the 24 hours. Relative humidity varies from 75% to a more persistent 100% as the temperature varies from an afternoon maximum of 308 K to a nighttime minimum of 299 K. Table 16-5 depicts the persistent high relative humidity of a steaming jungle or rain forest. While the temperature

Table 16-3. A repeated diurnal cycle during a month of sustained extreme sustained moisture content in August at Belize City, Belize.

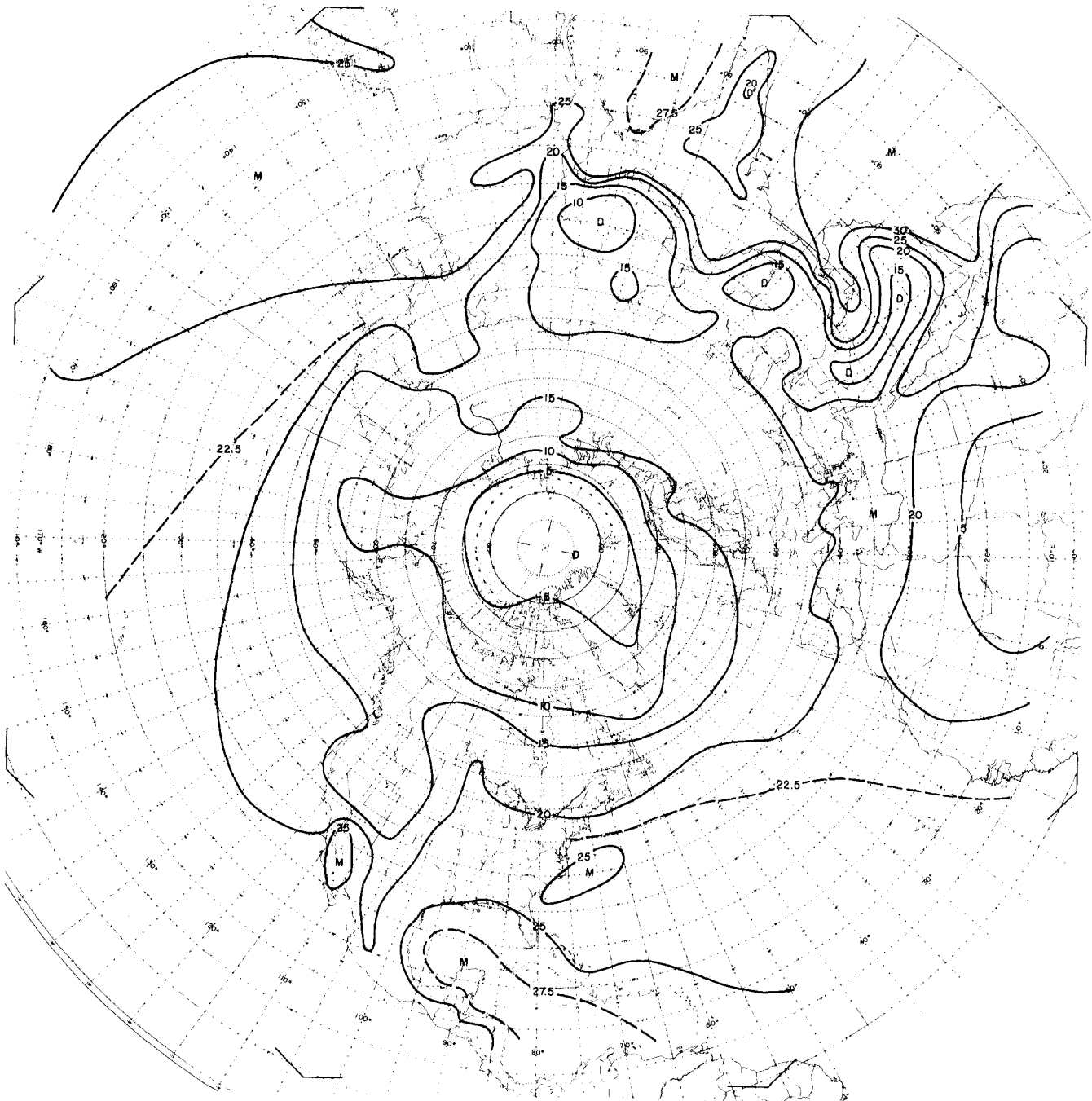| Time (LST)	Dew Point (K)	Temperature (K)	R.H. (%)	Insolation L/h
0000	300	301	91	0
0300	299	301	92	0
0600	299	300	94	4
0900	300	302	92	54
1200	301	303	91	83
1500	301	302	91	68
1800	300	302	91	20
2100	300	302	91	0

Figure 16-1.   Dew point (K-273) at the surface in July, 95th percentile [Gringorten et al., 1966].

consistently remains moderate at 297 K, the relative humidity persists above 95%. Such conditions may prevail several days a month throughout the year.

16.1.2 Troposphere

Climatic humidity data are relatively plentiful for altitudes up to 7 or 8 km (approximately 400 mb). Information on the distribution of water vapor at these levels in the northern hemisphere is provided in the *Atmospheric Humidity Atlas* [Gringorten et al., 1966]. Dew points aloft are mapped at 850, 700, 500 and 400 mb in percentiles from 5th to 95th for mid-season months. Also, two northern and southern hemispheric atlases [Crutcher and Meserve, 1970; Taljaard et al., 1969] have been published showing mean monthly dew points and standard deviations of the monthly averages for altitudes up to 500 mb.

Aloft, relative humidities of 100% can occur at any altitude below the tropopause over the entire globe. How-
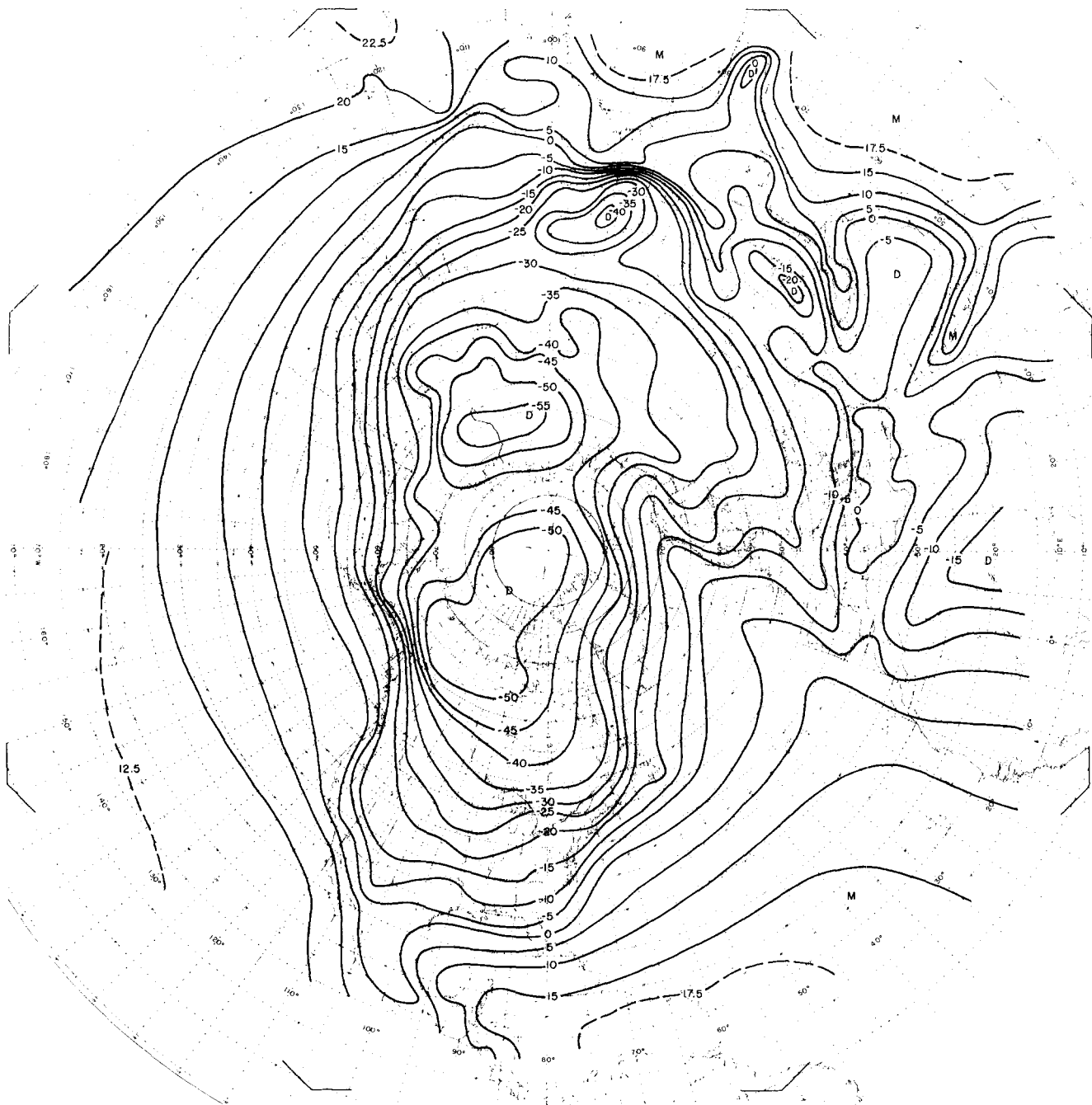
Figure 16-2. Dew point (K-273) at the surface in January, 5th percentile [Gringorten et al., 1966].

ever, the greatest moisture content is imbedded in the monsoonal flow over northern India. Table 16-6 presents high dewpoints with 1%, 5%, 10%, and 20% estimated probabilities in July from 1 to 8 km over northwestern India. Table 16-7 presents the low frost points with 1%, 5%, 10%, and 20% estimated probabilities in January from 1 to 8 km in the Canadian Northwest Territories.

Water vapor measurements above radiosonde humidity altitudes (roughly 8 km) are not made on a regular basis because of a lack of radiosonde instruments capable of sen-

sing low concentrations. Consequently, it is not possible at this time to describe spatial and temporal variations of water vapor in the upper troposphere in a manner comparable to that given for altitudes below 8 km.

For altitudes from 8 km up to the tropopause, atmospheric moisture can be estimated using information obtained from several different experimental sensors. In the upper troposphere the median mixing ratio appears to decrease approximately logarithmically with increasing altitude up to the tropopause. As a result, median dewpoints, given at 400

Table 16-4. A diurnal cycle associated with temperature and high relative humidity in the rainy tropics.

Time (LST)	Dew Point (K)	Temperature (K)	R.H. (%)	Insolation L/h
0000	300	300	100	0
0300	299	299	100	0
0600	299	299	100	4
0900	300	304	82	54
1200	302	307	75	83
1500	302	308	74	68
1800	302	305	82	20
2100	300	301	95	0

Table 16-5. A typical diurnal cycle in a tropical jungle with high relative humidity. (Such conditions may occur several days a month throughout the year.)

Time (LST)	Dew Point (K)	Temperature (K)	R.H. (%)
0000	297	297	100
0300	297	297	100
0600	297	297	100
0900	296	297	95
1200	296	297	95
1500	296	297	95
1800	296	297	95
2100	297	297	100

Table 16-6. High absolute humidity (dew point) extremes, 1 to 8 km aloft (typical of northern India in July).

Altitude (km)	Dew Point (K)			
	1% Probable	5%	10%	20%
1	302	300	299	298
2	297	295	294	293
4	289	286	283	282
6	276	273	272	271
8	265	262	261	260

Table 16-7. Low absolute humidity (dew point) extremes, 1 to 8 km aloft (typical of Canadian Northwest Territories in January).

Altitude (km)	Frost Point (K)			
	1% Probable	5%	10%	20%
1	223	231	233	236
2	222	228	231	234
4	217	221	222	224
6	208	212	213	214
8	202	202	204	205

mb (7 to 8 km) in the *Atmospheric Humidity Atlas* [Gringorten et al., 1966], can be converted to median mixing ratios and extended upward logarithmically to medians of 2 to 4 ppmm (parts per million by mass) at the appropriate tropopause height. The altitude of the tropopause ranges from 16 or 17 km in the tropics to 9 or 10 km near the pole [Cole and Kantor, 1978]. Estimated median mixing ratios at various latitudes are shown in Table 16-8.

World maps of the mean precipitable water above the surface and above 850, 700, and 500 mb have been published for the midseason months [Bannon and Steele, 1960]. More recently, reports on "Precipitable Water Over the United States" were compiled by the National Weather Service [Lott, 1976; Ho and Riedel, 1979]. Based on radiosonde observations, the range of the maximum precipitable water content over the contiguous United States is about 1 cm over the Rocky Mountains to nearly 7 cm along the Gulf of Mexico in the surface-to-400 mb layer. Table 16-9 presents mean monthly maximum precipitable water content for Key West, Florida and Lander, Wyoming.

16.1.3 Stratosphere and Mesosphere

Water vapor measurements in the stratosphere and mesosphere are not made at regular intervals because standard instrumentation is not available for use at these altitudes. Measurements at very low concentrations typical of the stratosphere can be made only with research quality instruments. Such sensors include frost point hygrometers, optical devices (such as spectrometers, radiometers), cryogenic air samplers and absorption devices. Roughly two dozen investigators have each provided from a few to over 100 observations during the last 35 years, with the bulk of stratospheric humidity measurements coming since 1965.

The earliest measurements, made by British aircraft [Brewer, 1949], provided evidence that the tropopause acts as a cap to water vapor, preventing it from penetrating into the stratosphere. General atmospheric circulation theory indicates that tropospheric air passes into the stratosphere over equatorial regions from where it moves northward. It sinks back into the troposphere at higher latitudes, closing the cycle. Tropical tropospheric air following this route into the stratosphere would have to pass through the very cold tropopause of the tropics (193 K) where the water vapor density would be forced to extremely low concentrations due to condensation and sublimation. As this air continues upward from this level, the mixing ratio in the stratosphere must remain constant if there is neither source nor condensation/sublimation of water vapor. The mixing ratio that most closely depicted these British findings is 2 mg per kg which may be interpreted as 2 ppmm. Some investigators report their measurements in terms of volume mixing ratio, denoted as ppmv. The relationship between ppmv and ppmm is ppmv = 1.607 ppmm. Other possible sources that have been suggested for water vapor to be introduced into the

Table 16-8. Estimated distribution of median mixing ratios in the upper troposphere.

Altitude (km)	15°N (ppmm) Jan	15°N (ppmm) Jul	30°N (ppmm) Jan	30°N (ppmm) Jul	45°N (ppmm) Jan	45°N (ppmm) Jul	60°N (ppmm) Jan	60°N (ppmm) Jul	75°N (ppmm) Jan	75°N (ppmm) Jul
400 mb*	433*	1050*	295*	722*	155*	540*	90.1*	401*	63.4*	295*
7	—	—	—	—	148	—	57.5	—	34.2	—
8	346	1010	213	510	38.5	368	11.3	48.7	8.3	24.6
9	205	513	130	239	9.8	136	2.0	13.2	2.0	2.0
10	122	250	80.0	113	2.5	50		2.0		
11	71.2	119	49.0	52.5		18.3				
12	42.0	57.2	29.8	24.6		6.7				
13	24.6	27.5	18.3	11.5		2.5				
14	14.5	13.2	11.2	5.4						
15	8.6	6.3	6.8	2.5						
16	5.3	3.0	4.1							
17	3.0		2.5							

*400-mb mixing ratios calculated from Gringorten et al. [1966].

stratosphere are the transport of tropospheric air upward through the overlapping tropical and polar tropopauses, cumulonimbus clouds penetrating the tropopause, and chemical reactions such as the oxidation of methane. The extent to which such mechanisms influence the stratospheric humidity regime continues to be debated. However, the combined effects of the Hadley cell circulation and tropical thunderstorms, both of whose inputs of moisture into the stratosphere must penetrate the tropical "cold trap," are responsible for the bulk of stratospheric mixture. In fact, most investigators agree that all other sources are smaller by a factor of 5 to 10.

In the early 1960s there was a significant controversy concerning the amount and distribution of water vapor in the stratosphere [Gutnick, 1961]. Much uncertainty continues, but the extent of uncertainty has narrowed. The bulk of credible observations of stratospheric mixing ratio now range from about 0.5 to 5 ppmm. The stratospheric water vapor measurements made over the previous decade or so have been summarized in two recent articles [Harris, 1976 and Penndorf, 1978]. The conclusions are that the mean midlatitude stratospheric mixing ratio is 2.5 ± 0.7 ppmm and is nearly constant with altitude up to at least 30 km. There is some evidence that from 30 km the mean may gradually increase to 3 ppmm at 45 km. This increase could be the result of an increase in water vapor due to the oxidation of methane in the middle atmosphere. There is also limited evidence for the existence of weak, shallow layers

of water vapor with mixing ratios up to about 4 ppmm occurring in 1- to 2-km layers at altitudes up to about 30 km.

Based on three independent series of field measurements, an annual cycle for stratospheric water vapor has been suggested, in which the amplitude of the seasonal variation is largest in the lowest part of the stratosphere, about 0.4 ppmm at 15 km, and decreases with altitude to about 0.1 ppmm above 20 km. The phase of the annual cycle also changes with altitude, with the maximum occurring in November at 15 km and in April at 20 km. This annual cycle may be related to the annual variations in the temperature and altitude of the tropical tropopause.

In the lower stratosphere (below 20 km) there seems to be a small but discernible latitudinal variation in mixing ratio, with higher values, about 3 ppmm, occurring near the equator and decreasing with latitude to somewhat less than 2 ppmm near 45° latitude in both hemispheres. The lack of data in polar regions does not allow estimates of variation at higher latitudes.

There have been even fewer observations of water vapor in the mesosphere than in the stratosphere; consequently, these distributions and variations continue to be controversial. However, there does seem to be reasonably consistent hypotheses of the general envelope of the vertical profile of mixing ratio from the stratopause to the mesopause. Deguchi and Muhleman [1982] compared their ground-based radio telescope measurements to rocket measurements by Scholz

Table 16-9. Mean monthly maximum precipitable water content—two extremes.

Station	Month	Layer, Surface to 850 mb	Layer, Surface to 700 mb	Layer, Surface to 500 mb	Layer, Surface to 400 mb
Key West, Fla.	Sep	2.7 cm	4.2 cm	5.2 cm	5.4 cm
Lander, Wyo.	Jan	—	0.4	0.7	0.8

CHAPTER 16

et al. [1970], Ehhalt et al. [1975] and Rogers et al. [1977]; airborne measurements by Farmer et al. [1980] and Waters et al. [1977]; and current photochemical models by Crutzen [1974] and Allen et al. [1981]. A concensus of these observations and models provides a midlatitude mesospheric water vapor profile of 4 to 5 ppmm at 50 km decreasing logarithmically with altitude to roughly 1 ppmm at 90 km. Such a profile is consistent with microphysical observations of noctilucent clouds. An experiment in which noctilucent cloud particles, captured by a rocket at the 80 km mesopause level included ice [Soberman, 1963, and Michaels, 1965], implies the existence of water vapor through a layer at this high altitude. Such clouds are not found at tropical latitudes and rarely found at middle latitudes where temperatures are seldom colder than 173 K [Cole and Kantor, 1978] at this level. They are normally seen at high latitudes in the summer where extremely cold mesopause temperatures prevail. During one experiment [Anonymous, 1963] in which such clouds were physically sampled, the temperature observed was 130 K. During another sampling, when the clouds had dissipated, a temperature of 153 K was measured. Assuming the temperature and pressure structure of the *Air Force Reference Atmospheres* [Cole and Kantor, 1978], frost points of 130 K and 153 K at 80 km convert to saturation mixing ratios of about 0.01 ppmv and 6 ppmv, respectively.

It is interesting to note that there is a region of the middle atmosphere, roughly 40 to 65 km, in which the combined temperature and pressure structure does not support the existence of clouds [Schilling, 1964]. The relatively warm temperature structure at these altitudes requires a saturation vapor pressure greater than the total atmospheric pressure—an obvious impossibility. This condition is denoted by the asterisk entries in Table 16-1.

16.2 PRECIPITATION

Knowledge of the frequency of occurrence of given rates of precipitation and associated vertical distributions of precipitation particles is important to the design and operation of many types of equipment. It is a critical input for evaluating and deploying systems which employ surveillance radar, and for the selection of microwave frequencies used in communicatins systems. The frequency and intensity of rainfall must also be considered in the design and operation of helicopter rotor blades, and leading edges of aircraft and missiles which are subject to erosion by precipitation particles. Water ingested by jet engines can cause flame-outs and penetrate protective coverings of exposed electronic and mechanical material. Precipitation in the form of hail is a serious hazard for aircraft, whereas snow loads and ice accretion on surface structures can destroy towers, radomes, and buildings. This section contains examples of the type of precipitation information available.

16.2.1 Surface Rates of Rainfall

Frequency distributions of various rainfall rates from actual data are available for only a small number of meteorological stations. Precipitation data for most areas of the world are limited mainly to average monthly and annual totals, and to the number of days on which precipitation fell. Clock hourly precipitation data (totals on the hour every hour) are available for numerous stations in the United States and Europe, but for only a few stations elsewhere. Monthly tabulations of the amounts of precipitation which fall in 5 to 180 min periods are also available for National Weather Service first-order stations in the United States and its island possessions. Special 1-, 2-, and 4-min rainfall rates have been taken at a number of locations in Southwest Asia, Europe and the United States.

These data have been used by scientists to develop mathematical models for estimating the frequency of occurrence of various duration-rainfall rates at locations where only routine rainfall observations are available. Some selected methods for estimating clock hour and instantaneous (1 min) rainfall rates are presented in the following sections.

16.2.1.1 Clock Hourly Rates. Several researchers have used available clock-hour rainfall data to derive methods for estimating the number of hours that specific rates occur at other locations. In 1965, Cole et al., [1965] presented three linear equations for determining the frequency of 3 clock-hour precipitation rates (1.5, 3.0, and 4.6 mm/h) vs an index of rainfall intensity. The index is the average per day of measurable precipitation obtained by dividing the total annual precipitation by the number of days with measurable precipitation of ≥ 0.25 mm. Winner [1968] elaborated on this and other earlier studies to develop techniques for estimating clock-hours of rainfall at rates of trace, 0.25, 0.5, 2.5, 6.4, 12.7, 25.4 and 50.8 mm/h, based on data from 123 National Weather Service stations with 5 to 10 year periods of record. The technique incorporates a moisture index, Y, where

$$Y = 100 \left[\frac{P/25.4}{PE} - 1 \right] \qquad (16.5)$$

P is the mean annual rainfall in mm, and PE is the mean annual potential evapotranspiration determined by the method developed by Thornthwaite et al. [1958].

Figures 16-3, 16-4, and 16-5 are nomograms for estimating the mean annual clock-hours per year that a rainfall rate of 6.4, 12.7, and 25.4, mm/h is equaled or exceeded in temperate latitudes. Potential evapotranspiration data for Equation (16.5) can be calculated using Thornwaite et al., [1958]. It is desirable to use the same period of record for all variables in the nomograms. If these publications are not available, clock-hour estimates of more limited value can be made by assuming Y to be zero.
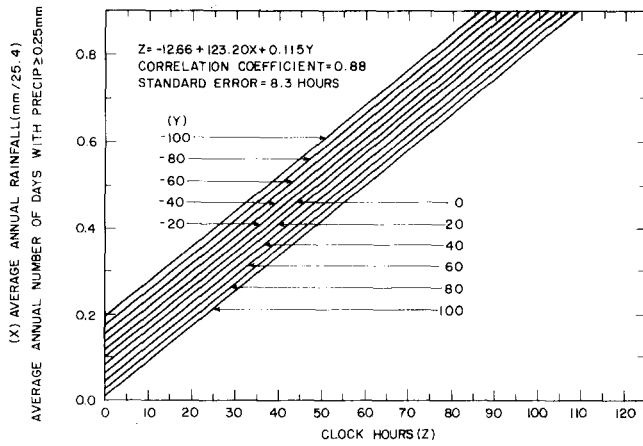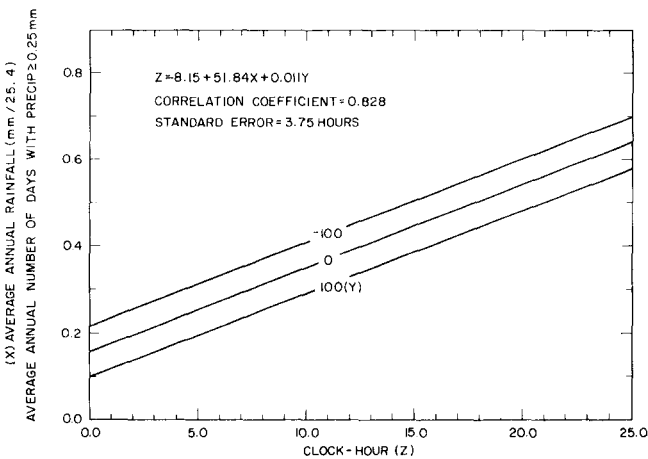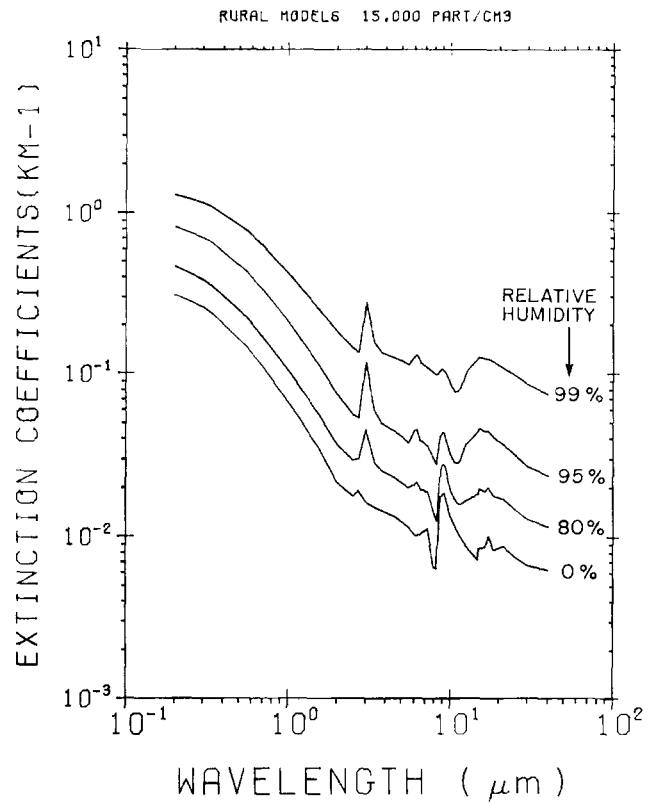
Figure 16-3. Nomogram for determining average number of clock hours per year a rainfall rate of 6.4 mm/h is equaled or exceeded.

The ratio of the average annual rainfall to the number of days with precipitation ≥0.25 mm for a location is then obtained from climatic data. Knowing this value and the value for Y, the number of clock-hours can be determined from the nomogram.

The technique described above provided poor results when applied on independent data from tropical locations. Therefore, Winner [1968] developed an alternate method for use in the tropics using data from 32 stations in the Panama Canal Zone. The best results were obtained from a linear correlation of the annual rainfall vs the number of clock-hours at specified rates. Figure 16-6 presents the clock-hours per year that rates of 6.4, 12.7, 19, and 25.4 mm/h are equaled or exceeded in the tropics.

16.2.1.2 Instantaneous Rates. For most applications, the distribution of rainfall rates for short periods, usually for 1 min, are of the greatest importance since these can greatly

Figure 16-5. Nomogram for determining average number of clock hours per year a rainfall rate of 25.4 mm/h is equaled or exceeded.

Figure 16-4. Nomogram for determining average number of clock hours per year a rainfall rate of 12.7 mm/h is equaled or exceeded.
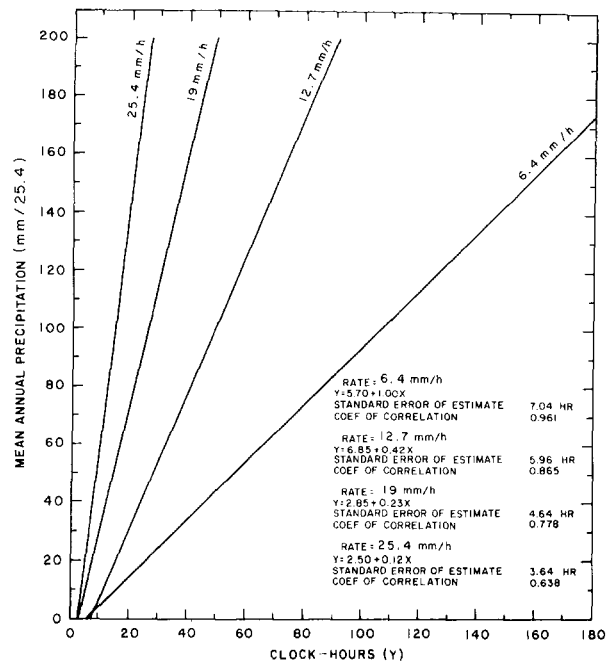
Figure 16-6. Nomogram for use in tropical regions to determine mean number of clock hours occurrence of a specified precipitation rate when the mean annual precipitation amount is known.

Table 16-10. Percent contribution of instantaneous precipitation rate to clock-hour precipitation rates for Urbana, Illinois (annual).

Clock-hour Rates mm/h*	Instantaneous Rates (mm/h)*									Tot No Clock-h
	0.00 – 0.76	1.0 – 2.3	2.5 – 6.1	6.4 – 12.4	12.7 – 25.1	25.4 – 50.5	50.8 – 126.7	127 – 254	>254	
Trace	96.02	3.43	0.51	0.04	0.0	0.0	0.0	0.0	0.0	576
0.25	87.56	10.38	1.96	0.06	0.04	0.0	0.0	0.0	0.0	114
0.5 – 2.3	59.17	29.16	10.17	1.16	0.25	0.08	0.01	0.0	0.0	581
2.5 – 6.1	27.34	19.24	37.58	11.82	2.82	1.05	0.15	0.0	0.0	179
6.4 – 12.4	23.50	11.28	23.01	23.14	12.16	5.33	1.58	0.0	0.0	61
12.7 – 25.1	20.45	8.53	14.74	16.28	16.99	13.53	8.65	0.83	0.0	26
25.4 – 50.5	6.67	5.56	8.89	13.33	19.44	20.00	25.56	0.56	0.0	3
50.8 – 76	0.0	0.0	0.0	0.0	0.0	0.0	0.0	0.0	0.0	0
76.2 – 101.3	0.0	0.0	0.0	0.0	0.0	0.0	0.0	0.0	0.0	0
101.6 – 126.7	0.0	0.0	0.0	0.0	0.0	0.0	0.0	0.0	0.0	0
≥127	0.0	0.0	0.0	0.0	0.0	0.0	0.0	0.0	0.0	0

*This work was originally presented in English units. Direct conversion to metric is the reason for small gaps between each range of rates.

exceed the hourly rate. A 1-min rainfall rate is generally referred to as being "instantaneous." Bussey [1950] found that about 20% of the time during an hour the instantaneous rate was zero, or a very low amount called a "trace." About 35% of the time the hourly rate was exceeded, and it was common for the hourly rate to be exceeded by 5 or 6 times for a few minutes.

Davis and McMorrow [1976] developed tables of clock-hour rate versus instantaneous rate for 6 locations, and clock-hour rate versus 4-min rate for 7 locations from original data. They indicate that these can be used to predict the 1- or 4-min rate for any region having a similar precipitation regime as determined from available clock-hour data. A variety of climates, including the wet tropics, is represented. Tables 16-10 and 16-11 from this study give the percent contribution of the instantaneous rate to clock-hour rate for Urbana, Illinois and Miami, Florida.

A more direct method for determining instantaneous rainfall rates was developed by Jones and Sims [1978]. They used instantaneous rainfall rate data for 9 observation sites, plus 4-min rainfall rate data at another 10 sites to evaluate the frequency of rainfall rates based on a world rain climate classification used by Herbstritt [1973]. Figure 16-7 from the Jones and Sims report shows the climatic classifications and the data stations. The data for stations within each of four of the five climatic zones were summarized and are presented in Figure 16-8. Although the curves in this figure are intended to represent instantaneous rainfall rates, mixing of the 1- and 4-min data has the net effect of giving a slightly low estimate for less than 10^{-1} exceedance frequency.

Table 16-11. Percent contribution of instantaneous precipitation rate to clock-hour precipitation rates for Miami, Florida (annual).

Clock-hour Rates mm/h*	Instantaneous Rates (mm/h)*									Tot No Clock-h
	0.00 – 0.76	1.0 – 2.3	2.5 – 6.1	6.4 – 12.4	12.7 – 25.1	25.4 – 50.5	50.8 – 126.7	127 – 254	>254	
Trace	93.55	4.60	1.49	0.33	0.04	0.0	0.0	0.0	0.0	92
0.25	85.31	9.44	4.01	1.17	0.06	0.0	0.0	0.0	0.0	27
0.5 – 2.3	65.67	19.97	11.13	2.30	0.66	0.26	0.01	0.0	0.0	170
2.5 – 6.1	39.21	16.40	29.82	9.84	2.21	2.14	0.38	0.0	0.0	74
6.4 – 12.4	29.81	11.52	18.64	22.42	9.47	5.87	2.23	0.04	0.0	44
12.7 – 25.1	34.04	6.32	16.67	10.61	10.00	11.14	10.18	1.05	0.0	19
25.4 – 50.5	15.50	12.17	7.50	12.33	13.17	13.67	20.83	4.83	0.0	10
50.8 – 76	0.0	0.0	0.0	0.0	0.0	0.0	0.0	0.0	0.0	0
76.2 – 101.3	0.0	0.0	0.0	0.0	0.0	0.0	0.0	0.0	0.0	0
101.6 – 126.7	0.0	0.0	0.0	0.0	0.0	0.0	0.0	0.0	0.0	0
≥127	0.0	0.0	0.0	0.0	0.0	0.0	0.0	0.0	0.0	0

*This work was originally presented in English units. Direct conversion to metric is the reason for small gaps between each range of rates.
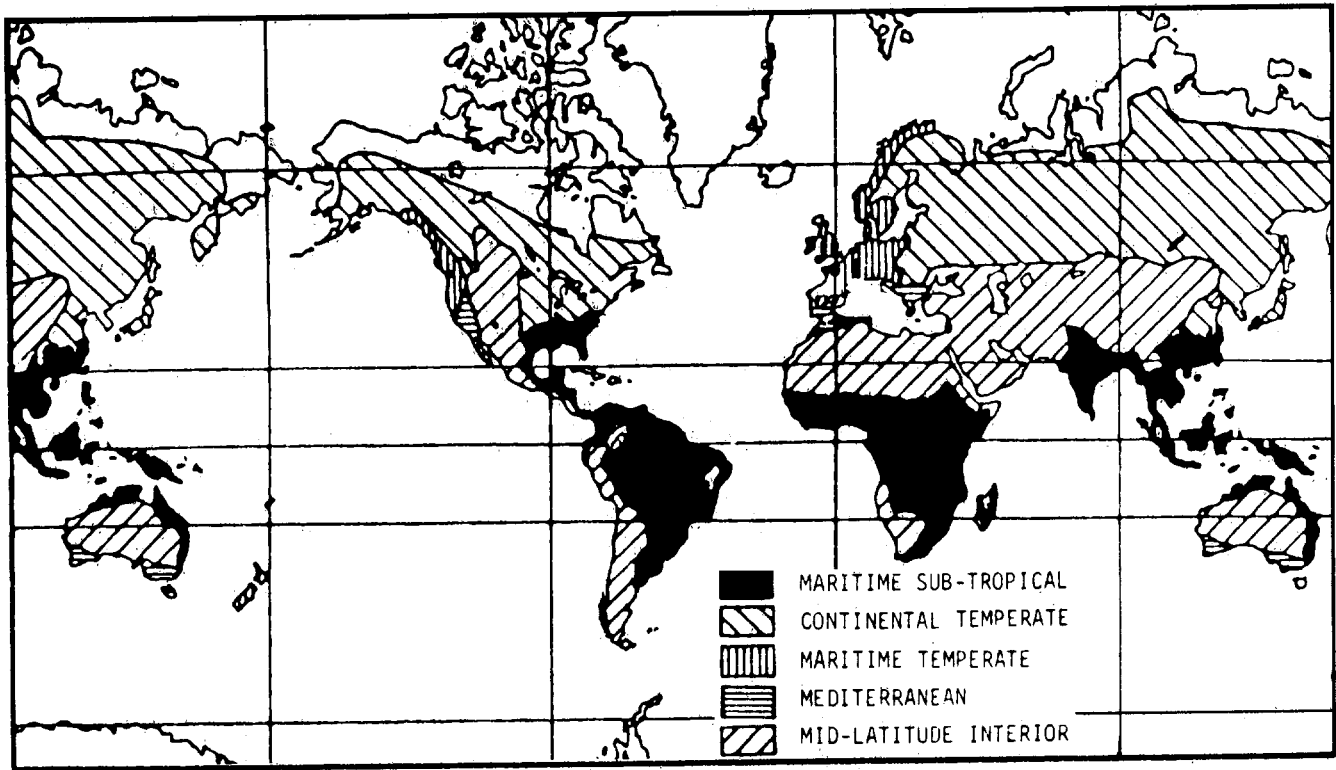
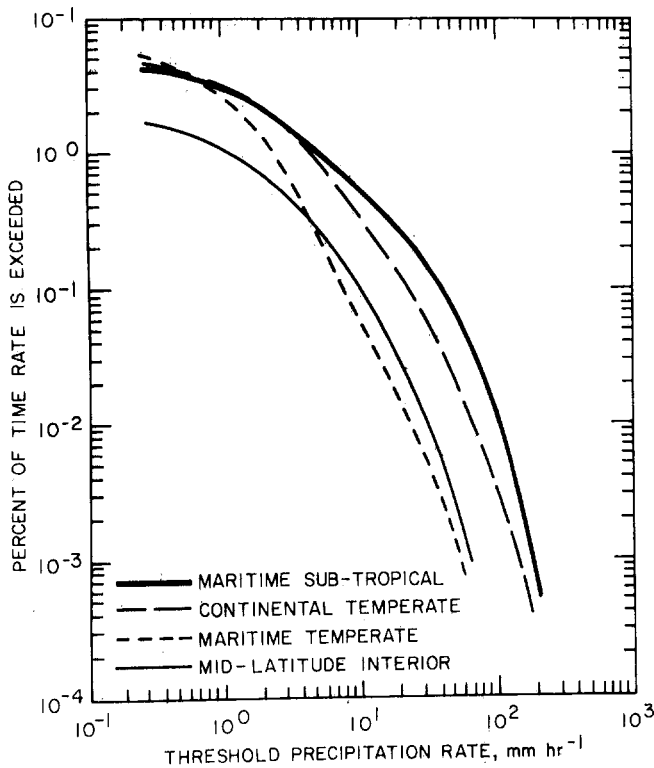Figure 16-7. Rain climates of the world [after Herbstritt, 1973].

Figure 16-8. Average rainfall rate—frequency relationships for four rain climates.

A more comprehensive model for determining instantaneous precipitation rates exceeded for a specified percent of a year was developed by Crane [1980]. The world was divided into 8 regions, as shown in Figure 16-9, on the basis of total rain accumulation, and maps showing the number of thunderstorm-days published by Landsberg [1974]. Additional guidance was taken from the Köppen world climate classification. Boundaries were adjusted to accommodate variations in terrain, predominant storm type and motion, general atmospheric circulation, and latitude. Satellite and precipitation frequency data were used to extend the rain climate regions over the ocean; however Feldman [1979] presents an elaborate expansion of the model for ocean areas. The U.S. is spanned by 5 regions; but one of them is divided into 3 sub-regions as shown in Figure 16-10.

The measured instantaneous rain rate distributions available for each of the 7 regions and 3 sub-regions were pooled to construct median rain rate distributions. These are presented in Table 16-12. No data were available for Region A, and the author does not explain how its distribution was derived.

Tattelman and Grantham [1982] discuss sources of 1-min data and present a survey and comparison of available models for estimating 1-min rates. They found that the best estimates of annual statistics on 1-min rates are made using the Davis and McMorrow model for locations where clock-
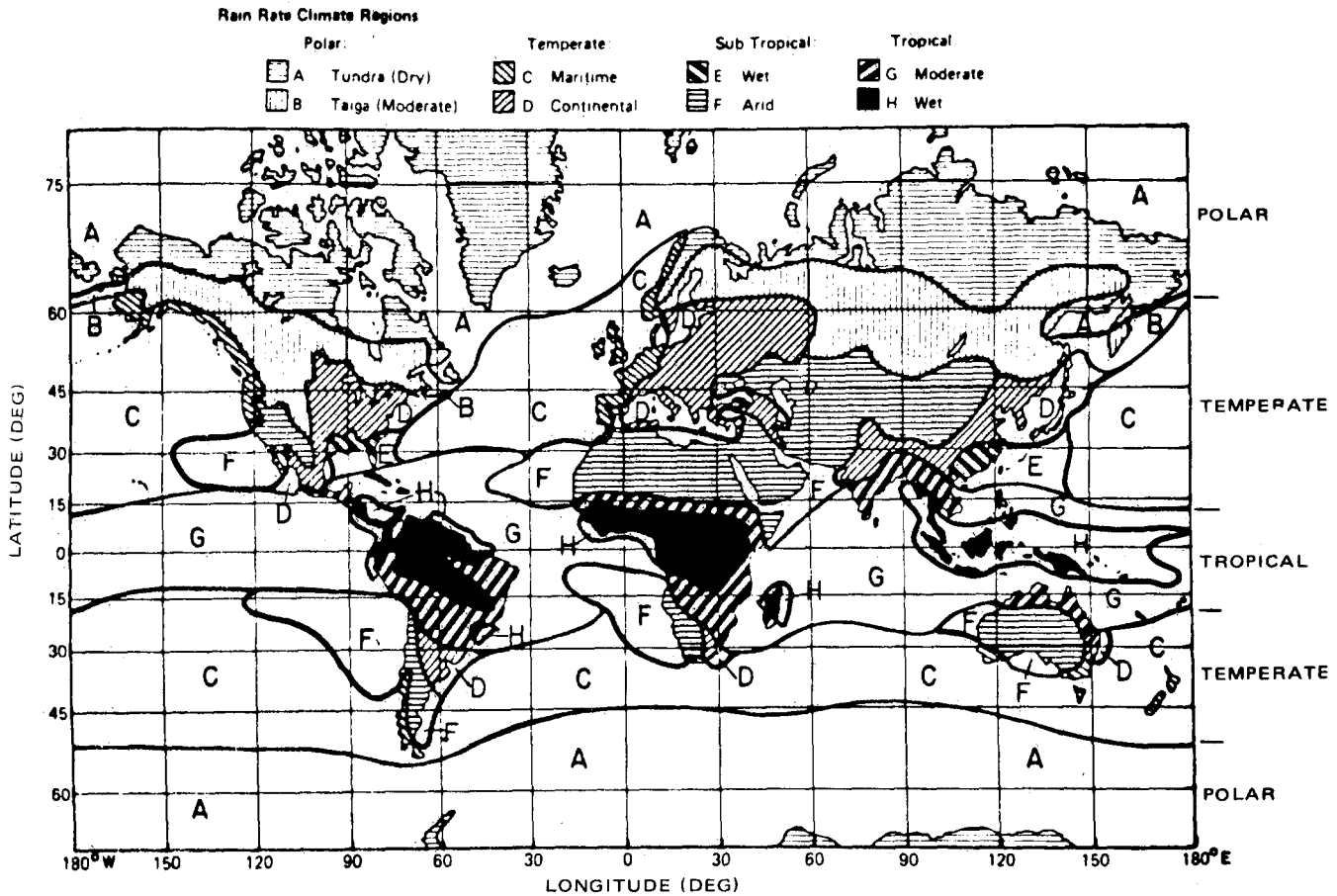
Figure 16-9. Rain rate climate regions [Crane, 1980]. (Reprinted with permission from IEEE © 1980)

hour data are available. Tattelman and Grantham also found that good estimates from clock-hour data could be made using a model developed by Huschke et al. [1982]. Huschke et al. consolidated the tables for the individual locations from Davis and McMorrow into 3 tables for all locations.

Figure 16-10. Rain rate climate regions within the United States [Crane, 1980]. (Reprinted with permission from IEEE © 1980)

Two tables represent "convective" and "stratiform" precipitation. The third table, which was found to be most accurate, simply includes all the data. Where clock-hour data are not available, Tattelman and Grantham found the Crane model produced estimates of annual 1-min rain rate statistics at least as good as any of the other available models.

A model for estimating instantaneous rainfall rates equaled or exceeded 2.0%, 1.0%, 0.5%, 0.1%, 0.05% and 0.01% of the time during a month from readily available climatological data was developed by Lenhard [1974] and improved by Tattelman and Scharr [1983].

The Tattelman-Scharr model was developed using stepwise multiple regression analysis for each of six exceedance levels (p = 2.0%, 1.0%, 0.5%, 0.1%, 0.05% and 0.01% of time during the month). The multiple regression equation is expressed by

$$R_p = A_p + B_pT + C_pI + D_p \ f(L,T) \quad (16.7)$$

where R_p is the estimated precipitation rate (mm/min) for exceedance level p, T is the monthly mean temperature (°F or 1.8 K − 459), I is a precipitation index (monthly mean precipitation divided by the monthly mean number of days

Table 16-12. Point rain rate (R_p) distribution values (mm/hr) versus percent of year rain rate is exceeded.

Percent of Year	Rain Climate Region									
	A	B	C	D_1	D_2	D_3	E	F	G	H
0.001	28	54	80	90	102	127	164	66	129	251
0.002	24	40	62	72	86	107	144	51	109	220
0.005	19	26	41	50	64	81	117	34	85	178
0.01	15	19	28	37	49	63	98	23	67	147
0.02	12	14	18	27	35	48	77	14	51	115
0.05	8.0	9.5	11	16	22	31	52	8.0	33	77
0.1	5.5	6.8	7.2	11	15	22	35	5.5	22	51
0.2	4.0	4.8	4.8	7.5	9.5	14	21	3.2	14	13
0.5	2.5	2.7	2.8	4.0	5.2	7.0	8.5	1.2	7.0	13
1.0	1.7	1.8	1.9	2.2	3.0	4.0	4.0	0.8	3.7	6.4
2.0	1.1	1.2	1.2	1.3	1.8	2.5	2.0	0.4	1.6	2.8
Number of Station Years of Data	0	25	44	15	99	18	12	20	2	11

with precipitation), and f(L,T) is a latitude-temperature term defined as

$$f(L,T) = \begin{cases} 0 & L \leq 23.5° \\ (L - 23.5)T & 23.5° < L \leq 40° \\ (40 - 23.5)T & L > 40° \end{cases}$$

(16.8)

A_p is the constant for exceedance level p, and B_p, C_p, and D_p are multiple regression coefficients for T, I and f(L,T), respectively, for exceedance level p.

The minimum threshold amount of precipitation to define a rainy day varies with country. Three of the most common threshold values used worldwide to define a rainy day are 0.25, 1, and 2.54 mm. The number of days per month with another frequently used threshold called a "trace" differs only slightly with the number of days equal to or greater than 0.25 mm. Results of the stepwise multiple

regression analysis for each of the six exceedance levels, including regression coefficients and constants to be used in Equation (16.7), are provided in Table 16-13, 16-14 and 16-15 for indices based on rainy day threshold values of 2.54 mm, 1 mm, and 0.25 mm, respectively.

The Tattelman-Scharr model was subjectively evaluated by estimating rates at independent locations representing a wide variety of the earth's climates. Results indicted several circumstances when the model is either invalid or should be used with discretion. This occurred for very dry or cold months for which there were little or no data among the dependent stations. The model was found to be generally invalid when any of the following conditions exist for a specific month at a location:
1. $T \leq 273$ K
2. $I < 2$mm/day
3. Number of rainy days < 1.

Inconsistencies such as negative rates, or increasing rates with increasing exceedance level occasionally occur when

Table 16-13. Results of stepwise multiple regression analysis for exceedance levels p = 0.01%, 0.05%, 0.10%, 0.50%, 1.0%, and 2.0% based on a threshold value of 2.54 mm for I. (The regression coefficients are given for each independent variable.)

P	Constant A_p	T B_p	$I_{(2.54)}$ C_p	f(L,T) D_p	R	SEE (mm/min)
0.01	-0.91	2.8×10^{-2}	2.3×10^{-2}	-3.4×10^{-4}	0.83	0.43
0.05	-0.50	1.6×10^{-2}	1.9×10^{-2}	-3.1×10^{-4}	0.86	0.24
0.10	-0.31	1.1×10^{-2}	1.4×10^{-2}	-3.0×10^{-4}	0.85	0.19
0.50	-0.01	2.5×10^{-3}	5.4×10^{-3}	-1.5×10^{-4}	0.76	0.09
1.0	0.03	7.4×10^{-4}	2.9×10^{-3}	-7.6×10^{-5}	0.67	0.06
2.0	0.04	-2.0×10^{-4}	1.5×10^{-3}	-3.2×10^{-5}	0.64	0.02

Table 16-14. Results of stepwise multiple regression analysis for exceedance levels p = 0.01%, 0.05%, 0.10%, 0.50%, 1.0%, and 2.0% based on a threshold value of 1.00 mm for I. (The regression coefficients are given for each independent variable.)

P	Constant A_p	T B_p	$I_{(1.00)}$ C_p	f(L,T) D_p	R	SEE (mm/min)
0.01	-1.00	2.8×10^{-2}	3.6×10^{-2}	-2.2×10^{-4}	0.84	0.41
0.05	-0.56	1.6×10^{-2}	2.5×10^{-2}	-2.4×10^{-4}	0.88	0.23
0.10	-0.36	1.1×10^{-2}	2.0×10^{-2}	-2.4×10^{-4}	0.87	0.18
0.50	-0.03	2.4×10^{-3}	7.8×10^{-3}	-1.2×10^{-4}	0.79	0.09
1.0	0.02	6.9×10^{-4}	4.2×10^{-3}	-6.2×10^{-5}	0.71	0.05
2.0	0.04	-1.8×10^{-4}	2.0×10^{-3}	-2.6×10^{-5}	0.67	0.02

T is between 273 K and 277 K. When T is in this range, estimated rates are acceptable if they are positive and decrease with increasing exceedance level. If the estimated rates are consistent, but a negative rate is estimated for p = 2%, this may indicate that it rains less than 2% of the time during that month.

When there are between 1 and 3 rainy days in the month, the model may estimate rates for each of the exceedance levels which, when integrated, indicate a total rainfall two or more times greater than the monthly mean precipitation. Under these circumstances heavy, but infrequent, convective precipitation accounts for just about all of the precipitation in the month. Therefore, the most accurate estimates are for the two or three lowest exceedance levels, and significant rainfall might not occur more often than 0.5% of the month. These possibilities should be considered before accepting rate estimates in arid locations.

16.2.1.3 Extreme Rates.

As noted in the previous sections, there are many stations in the world where precipitation is measured, but there are few outside of the U.S. and Europe where amounts are tabulated and published for time periods of less than 24 hours. In tropical regions, where the most intense precipitation occurs, data on extremes of short-duration rainfall are even rarer than for the middle latitudes. United States Weather Bureau Technical Paper No. 25 [1955] presents rainfall intensity-duration curves for 200 stations in the contiguous United States plus 1 station each in Alaska, Hawaii, and Puerto Rico. Lenhard and

Sissenwine [1973] found Pensacola, Florida to have the most intense rainfall of the 203 stations; the curves for Pensacola are reproduced in Figure 16-11 for 2- to 100-yr return periods. Smoothed analyses of the data from individual stations were subsequently published by the National Weather Service because the variable nature of rainfall can result in substantial differences in rainfall intensity statistics between stations separated by a relatively short distance [for example, Frederick et al., 1977]. A return period represents the time interval that an event would be expected to occur at least once. Mathematically, a return period of n years is the reciprocal of the probability of the event occurring in one year. If we denote the probability of the event not occurring in one year by P, the P = (2 − 1/n). The probability that it will not happen in n years is P^n. That is, the probability of the event occurring at least once in its return period approaches 63% asymptotically as n increases. Comparision of the these curves with estimates of world-wide extremes using the model presented in the Lenhard and Sissenwine study indicate that, except for tropical mountainous areas with orographically enhanced rainfall, rainfall intensities at Pensacola are comparable to those at some of the more extreme locations in the world. This is not surprising, since thunderstorms occurring in tropical maritime air over the United States are considered as severe as most places in the world.

The most extreme rainfall intensities that have ever been recorded in the world for time periods of 1 minute to 1 year are shown in Figure 16-12, with an envelope of their extremes. Data used were obtained from Riordan [1974].

Table 16-15. Results of stepwise multiple regression analysis for exceedance levels p = 0.01%, 0.05%, 0.10%, 0.50%, 1.0%, and 2.0% based on a threshold value of 0.25 mm for I. (The regression coefficients are given for each independent variable.)

P	Constant A_p	T B_p	$I_{(0.25)}$ C_p	f(L,T) D_p	R	SEE (mm/min)
0.01	-1.00	2.8×10^{-2}	4.2×10^{-2}	-2.2×10^{-4}	0.85	0.41
0.05	-0.56	1.6×10^{-2}	3.0×10^{-2}	-2.3×10^{-4}	0.88	0.22
0.10	-0.36	1.1×10^{-2}	2.4×10^{-2}	-2.3×10^{-4}	0.88	0.17
0.50	-0.03	2.3×10^{-3}	1.0×10^{-2}	-1.2×10^{-4}	0.82	0.08
1.0	0.01	5.6×10^{-4}	6.0×10^{-3}	-5.6×10^{-5}	0.77	0.05
2.0	0.03	-2.3×10^{-4}	2.8×10^{-3}	-2.4×10^{-5}	0.74	0.02
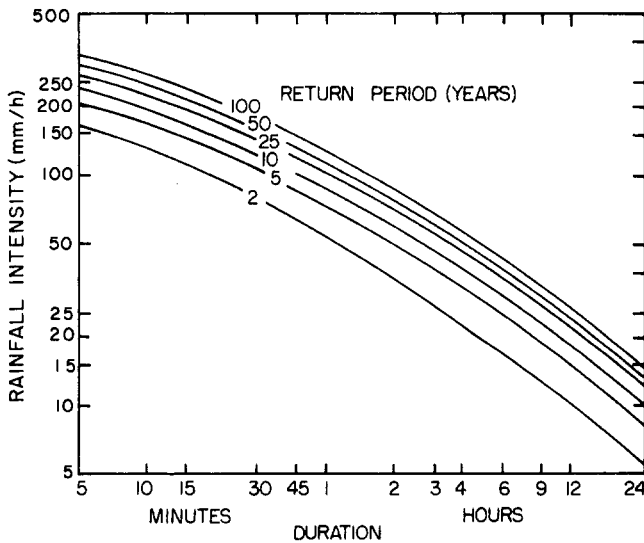
16.2.1.4 Duration of Rainfall Rates. The question of how long a given rate is likely to persist was investigated by Sims and Jones [1973]. They derived duration tables for Miami, Fla.; Majuro Island; Island Beach, N.J.; Franklin, N.C.; and Urbana, Ill. based on an analysis of at least one year of 1-min rainfall rates at each location. The tables present the conditional frequency distribution of occurrences of various durations from 1 to 90 minutes for rainfall rates from 0.2 to 3.0 mm/min. Table 16-16 presents the results for Miami, Fla. based on 1 year of data. The table indicates, for example, that when it was raining the rate exceeded 0.8 mm/min, it continued at that rate or greater for at least 4 min 52.1% of the time. It equaled or exceeded that rate continuously for 25 min only 1.1% of the time. Note that
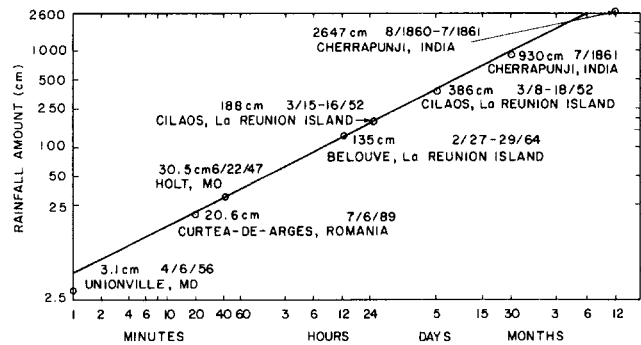
Figure 16-12. World record rainfall values.

the table does not indicate how often various rates occur, but how long various rates continued at that rate or higher without dropping to a lower rate.

16.2.1.5 Rainfall Rates Along Lines. Jones and Sims [1971] present data for 3 rain gage networks, one near Miami and two in England. Data for a larger network in central Illinois are presented by Sims and Jones [1973]. Average intensities along paths of various lengths, based on 2-min rates, were derived for all the networks. The cumulative frequencies of average rates for 2-gage (5-km), 8-gage (33-km), and 14-gage (62-km) north-south lines in the central Illinois network are shown in Figure 16-13. This figure illustrates the effect of line length on the frequency of the line-averaged rates. For rates greater than 0.2 mm/min, the highest rates occur most often on the shortest line. This is because larger paths are likely to extend beyond the high rates at the core of a rain cell into an area of light or no rain. This situation reverses during light rain (<0.2 mm/min in the figure) since a short path is more likely to be associated with the fringe of a rain cell.

Table 16-16. Conditional frequencies of durations of various precipitation rates for about one year of data from Miami, Florida.

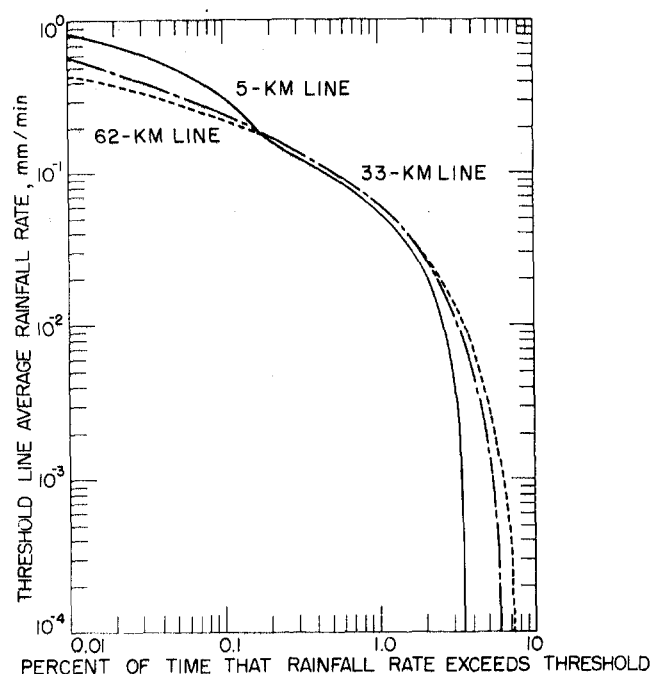| Duration Equaled or Exceeded (min)	Rate Equaled or Exceeded (mm/min)										
	0.2	0.4	0.6	0.8	1.0	1.25	1.50	1.75	2.0	2.5	3.0
1	100.0	100.0	100.0	100.0	100.0	100.0	100.0	100.0	100.0	100.0	100.0
2	85.7	67.1	72.3	77.7	81.9	69.0	62.8	74.1	59.1	45.5	50.0
4	53.3	47.9	43.1	52.1	43.1	29.3	20.9	22.2	22.7	0.0	0.0
6	37.3	27.7	26.2	28.7	19.4	8.6	11.6	11.1	4.5		
8	25.4	20.7	20.0	16.0	8.3	6.9	4.7	3.7	4.5		
10	19.7	14.9	11.5	11.7	6.9	5.2	4.7	0.0	0.0		
15	11.9	8.0	6.9	6.4	5.6	1.7	0.0				
20	7.8	4.8	4.6	4.3	0.0	0.0					
25	5.7	1.6	0.8	1.1							
30	4.1	0.5	0.8	0.0							
45	1.2	0.0	0.0								
60	0.4										
90	0.0										

Figure 16-13. Cumulative frequency distributions of average rainfall rates for 5-, 33-, and 62-km north-south lines in central Illinois.

16.2.2 Hail

Hail consists of ice particles with a diameter of 5 mm or more. Smaller particles are classified as ice pellets. Generally transparent globular ice pellets are called sleet, while generally translucent snow pellets encased in a thin layer of ice are called graupel or soft hail. If the diameter of the ice particles is 2 cm or more, it is called large hail.

The potential for damage of hailstones depends on the size, density, hardness, number density, impact velocity, and duration of the hailstorm. For a vehicle in flight the horizontal extent of the hailstorm also becomes important. However, it is difficult or impossible to take all factors into account. Consequently, for this review the criterion of hailstorm intensity is arbitrarily restricted to maximum stone size.

Hailstone diameters of 1.9 to 2.5 cm are the minimum for damage to aircraft, especially in flight when the impact is greater due to airspeed. The metal surface of a transport aircraft at rest on the ground resists damage from hailstones up to 7.5 cm in diameter. Damage to crops reportedly occurs with hailstones exceeding 3.5 cm in diameter. However, a great number density of smaller 6 mm stones will damage crops of wheat, corn and soybeans [Gringorten, 1971]. Terminal velocity, an important factor in the destructive power, is related directly to the size of the hailstones.

16.2.2.1 Hailstone Characteristics.
Although hailstone diameters are usually less than 1.3 cm, there is a distribution

frequency from 0.25 cm to several centimeters. In September 1970 a hailstone diameter of 14 cm was reported to have fallen in Coffeyville, Kansas. In hailstorms, the conditional probability of occurrence of maximum-size hailstones of 7.5 cm or greater is approximately 0.5%, of 5 cm or greater 2%, of 2.5 cm or greater 7% or 8%. Diameters of less than 3 mm occur roughly 5% of the time [Gringorten, 1971].

The density (weight per unit volume) of hailstones is a variable with little documentation. For some large natural hailstones in several storms in the midwestern U.S., estimates ranged from 0.828 to 0.867 g/cm^3. Hence, a rounded value of 0.9 g/cm^3 is deemed acceptable in calculations of impact energy. Such large hailstones have an onion-like structure, attesting to the up-and-down motion to which they have been subjected during their growth in severe storms.

Terminal velocity (w), according to most authors, can be related directly to the hailstone diameter (d) by

$$w = K\sqrt{d} . \qquad (16.10)$$

For w in cm/s and d in cm, the value of K at the surface has been found to range from 1150 to 1990, with a "best" estimate at 1630.

16.2.2.2 Hailstorm Characteristics.
The ratio of hailstorms to thunderstorms varies greatly with geography, so that thunderstorm frequency is no criterion of hail frequency. The month of greatest hailstorm frequency also varies. In the United States the hail season extends from April to September, with June and July the most severe months. Most hail occurs between 1200 and 1900 LST with a peak for damaging hail at 1600 LST.

The width of a swath of hailstone incidence has been variously estimated from a few yards to 120 km, but rarely more than 8 km. The length of the path is considerably greater than the width, but even more difficult to define. The term "hailstreaks" has been coined for hailstorms in the midwest, which are normally 2 to 25 km long in Illinois. The median width is 1.5 to 3 km, the length is 10 km in Illinois and 25 km in South Dakota. The areal extent of these hailstreaks varies from 2 to 2000 km^2.

Large hail (greater than 2 cm), is found only in well-developed thunderstorms whose cloud tops may reach 15 km. Small hail and soft hail are thought by some meteorologists to be an essential feature of all thunderstorms. However, ice particles less than 1 cm in diameter, which may be present aloft in the cores of the thunderstorms, are likely to melt completely before reaching the ground. Although thunderstorms are most frequent in the tropics and subtropics, occurring up to 180 days per year in several places, hail is rarely found on the ground in the tropics. Hail on the ground is most likely found in midlatitude mountainous and adjacent areas.

16.2.2.3 Frequency and Duration at the Ground. The most severe hail activity in the world occurs in the United States, and the most significant center within the United States is in western Nebraska and southeastern Wyoming. Although the greatest number of hailstorm days is at Cheyenne, Wyoming, averaging 9.4 days per season, it is so localized that an average of 7 days per year may be considered an acceptable extreme. By comparison, in some areas thunderstorms average 40 to 50 days per year. In the most severe month and in the most severe location, the average number of hailstorms is 2.9 per month. However, a more acceptable number for our use, especially for application to flight paths, is 2 hailstorms per month.

Using the average of 7 hailstorms per year in the Poisson distribution for the frequencies of zero, one, and two hailstorms per year, together with the conditional frequency distribution of the maximum hailstone size in a storm (Section 16.2.2.1), we obtain the cumulative probability of the annual largest hailstone diameter in the most severe location shown in Figure 16-14. Application of the Gumbel distribution further leads to estimates of the greatest diameters in periods of 1 to 25 years (Table 16-17).

The duration of hailstorms has been reported variously from a few minutes to a few hours. The best estimate for the average time, at the point of most severe occurrence and in the most severe month, is 10 min [Changnon, 1970]. When this is coupled with the average of 2 hailstorms per

Table 16-17. Diameter of the maximum-size hailstone in period of 1 to 25 years in the most severe location.

Period of Years	Hailstone Diameter (mm)	
	Average	10% Extreme
1	25	55
2	35	66
5	53	76
10	63	89
25	76	102

month, the single-point probability of encountering a hailstorm becomes 0.000448. The probability of encounter in terms of hailstone size is shown in Table 16-18.

16.2.2.4 Hail Aloft. Nearly every thunderstorm has some hail, snow, or ice pellets at one stage or another of its development, particularly at levels between 6 and 8 km. At any given time, however, hail is considered to occur in a shallow layer. Above 9 km hail has been encountered infrequently, but cannot be discounted.

In the absence of sufficient and objective data, a certain amount of inference must be used in considering the frequency of hail as a function of altitude. Hailstones must form and grow in size above the freezing level in the atmosphere. Over northeastern Colorado, western Nebraska, or southeastern Wyoming, the average height of the 273 K isotherm is 4.1 km during the hail season (summer). Once formed, the hailstones will fall, be buffeted vertically up and down, or become suspended at a "balance" level. This should become a level of high concentration and, therefore, a level with a relatively high probability of hail occurrence. Balance levels may be either at or below the level of updraft maximum, but above the freezing level.

With our present knowledge, it is expedient to assume

Figure 16-14. Cumulative probability of the annual largest hailstone diameter in the most severe location, plotted on extreme probability paper.

Table 16-18. Estimates of the probability of encountering hailstones of given diameter at a single-point location from ground to 1500 km in the most severe location in the worst month.

Hail Diameter (cm)	Single-station Probability
Any size	0.448×10^{-3}
≥ 0.6	0.354×10^{-3}
≥ 1.3	0.161×10^{-3}
≥ 1.9	0.605×10^{-4}
≥ 2.5	0.314×10^{-4}
≥ 5.1	0.851×10^{-5}
≥ 7.6	0.170×10^{-5}
≥ 10.2	0.25×10^{-6}

that the probability of encountering hail is uniformly the same at any level from 3 to 6 km, and that any level in this interval can become a level of hail concentration. Concomitantly, it is assumed that the probability of hail encounter decreases from 3 downward to 1.5 km and also from 6 upward to 14 km. Since hailstones do not form or grow at the 1.5 km level, and since hailstones do not melt appreciably when falling from that level to the surface, the probability of hail encounter at levels at and below 1.5 km is approximately the same as that found at the surface (0.000448).

For the significantly large hailstones (>2 cm diameter), it has been found that their diameters remain virtually unchanged when falling from aloft to the ground. As a result, the conditional probability distribution of hailstone diameters aloft can be adequately estimated by the conditional probability distribution at the surface.

Estimates of the ratio of probabilities of hail aloft to hail at a lower level are available for thunderstorms in Ohio and Florida. In these storms hail was encountered about 7 times more often between 3 and 6 km than at 1.5 km. These data also indicated that at 7.6 km the probability of encountering hail is about 3 times as great as at 1.5 km. Above 7.6 km the probability of encountering hailstones diminishes steadily to nearly zero at 13.7 km (Table 16-19).

The probability of hail occurring at the ground increases with increasing height of the radar-echo tops of the associated thunderstorm. For example, hail has been reported on the ground for about half of the New England thunderstorms when radar-echo tops have exceeded 15 km. In addition, hailstorms in the southern and midwestern U.S. sometimes have echo tops up to 18 and 21 km [Kantor and Grantham, 1968]. These extremely high echo tops extend well above the cirrus anvil and penetrate several kilometers into the stratosphere. Because these giant storms must be accompanied by exceedingly high vertical velocities, hail above the tropopause is possible.

Table 16-19. Estimates of the probability of encountering hail of any size at a single-point location by altitude.

Altitude (km)	Probability
Ground level	0.000448
1.5	0.000448
3.0	0.00314
4.6	0.00314
6.1	0.00314
7.6	0.00134
9.1	0.00100
10.7	0.00067
12.2	0.00034
13.7	0.000

Table 16-20. Estimates of the probability of occurrence of a hailstorm in an area (A), in the worst area during the worst period, when 2 hailstorms per month are expected at any single point.

Area A (km^2)	Probability (in %)
0	0.045
26	0.06
260	0.17
2600	0.58
26 000	3.1
260 000	29

16.2.2.5 Area and Line Coverage. Ten years of observations at a network of some 50 stations in a 400 km^2 area around Denver [Beckwith, 1960] gave the average ratio of occurrence of hailstorm days in that area to the occurrence at a single station as 4.4 to 1. Thus, if the probability of occurrence at a single station is 0.000448, then the probability of one or more occurrences in a 400 km^2 area would be 0.00197. A subsequent investigation in Illinois and South Dakota [Changnon, 1971] has led to the conclusion that the area-to-point ratio of hail-day frequencies is related to the area size, but is reasonably independent of geography.

With the above information a recent model of areal coverage [Gringorten, 1979] has yielded an estimate of the correlation coefficient of 0.99 for hail events at points 1.3 km apart. With this estimate the probability of a hailstorm occurrence somewhere in an area (A) as a function of the size of that area becomes as shown in Table 16-20. The model also has yielded the probability of encountering hail along a flight path (at an altitude where the single-point probability is 0.00314), as 0.025 in a path length of 160 km, and 0.042 in a path of 320 km. The probability of encountering hailstones of at least 2.5 cm in diameter is smaller by 7/100, becoming 0.0018 for 160 km and 0.0029 for 320 km.

16.2.2.6 Hail in Design and Operation of Equipment. Since the probability of hail of even the smallest size is very slight between the ground and 1500 m and since the effect of hail on most surface equipment will not result in endangering human life, there is no need to specify a hail-size extreme as an operational design criterion. If hail interferes with a surface operation, postponement until the storm ends is advisable.

Aloft (between 3 and 6 km), probabilities of hail are as high as 0.00314, which is still sufficiently low so that there is no need to specify a hail-size extreme for equipment whose failure would not endanger human life. If such danger exists, however, the estimates provided in this section should be considered.

16.2.3 Snowfall

Snow is important to the design of equipment and structures that must bear an increased structural load imposed by snow accumulations. It can also impede movement over uncleared ground. In areas where the mean winter temperatures are near or below freezing, the maximum depth of snow during the season is usually the accumulation from many individual snows. In warmer climates extremely heavy snowstorms can occur, but these are usually followed by melting and amounts on the ground at any one time are not as great as in colder areas farther north. The most favored locations for heavy snowstorms and excessive snow depths are mountain locations, especially those in proximity to large bodies of water.

A survey on North American snowfall extremes through the 1969-70 season by Ludlum [1970] indicates that each state in the U.S., except Florida and Hawaii, has recorded 24-h snowfalls of at least 45 cm. North America's heaviest 24-h accumulation of 193 cm occurred at Silver Lake, Colorado, a mountain location (elevation 3115 m). A study of intense snowfalls by Riordan [1973] indicates that at least

75 cm of snow has been recorded in a 24-h period in 23 states in the U.S. including locations as far south as Arizona, New Mexico, North Carolina, and Virginia. The greatest Canadian 24-hour snowfall was 112 cm at Livingston, Alberta. North America's greatest single storm accumulation of 480 cm occurred at Mt. Shasta Ski Bowl in the California mountains [Riordan, 1974]. The greatest measured snow depth in the U.S. was 1145 cm at Tamarack, California.

Snow loads on structures are not routinely measured and must be estimated. This requires information not only on the depth of snow, but also its density. Even then, the shape and type of structure, and its wind exposure must be taken into account. The density of freshly fallen snow is most commonly between 0.05 and 0.15 g/cm^3. Consequently an accumulation of 76 cm with a "normal" density of 0.1 g/cm^3 would result in a snow load on the ground of about 76 kg/m^2. Depths in much of North America can greatly exceed 76 cm, and rain on top of the snow significantly increases its density. Boyd [1961] analyzed snowfall statistics for more than 200 Canadian stations. His analysis of the maximum depth of snow is shown in Figure 16-15 for a 30-year return period, the time interval in which the indicated
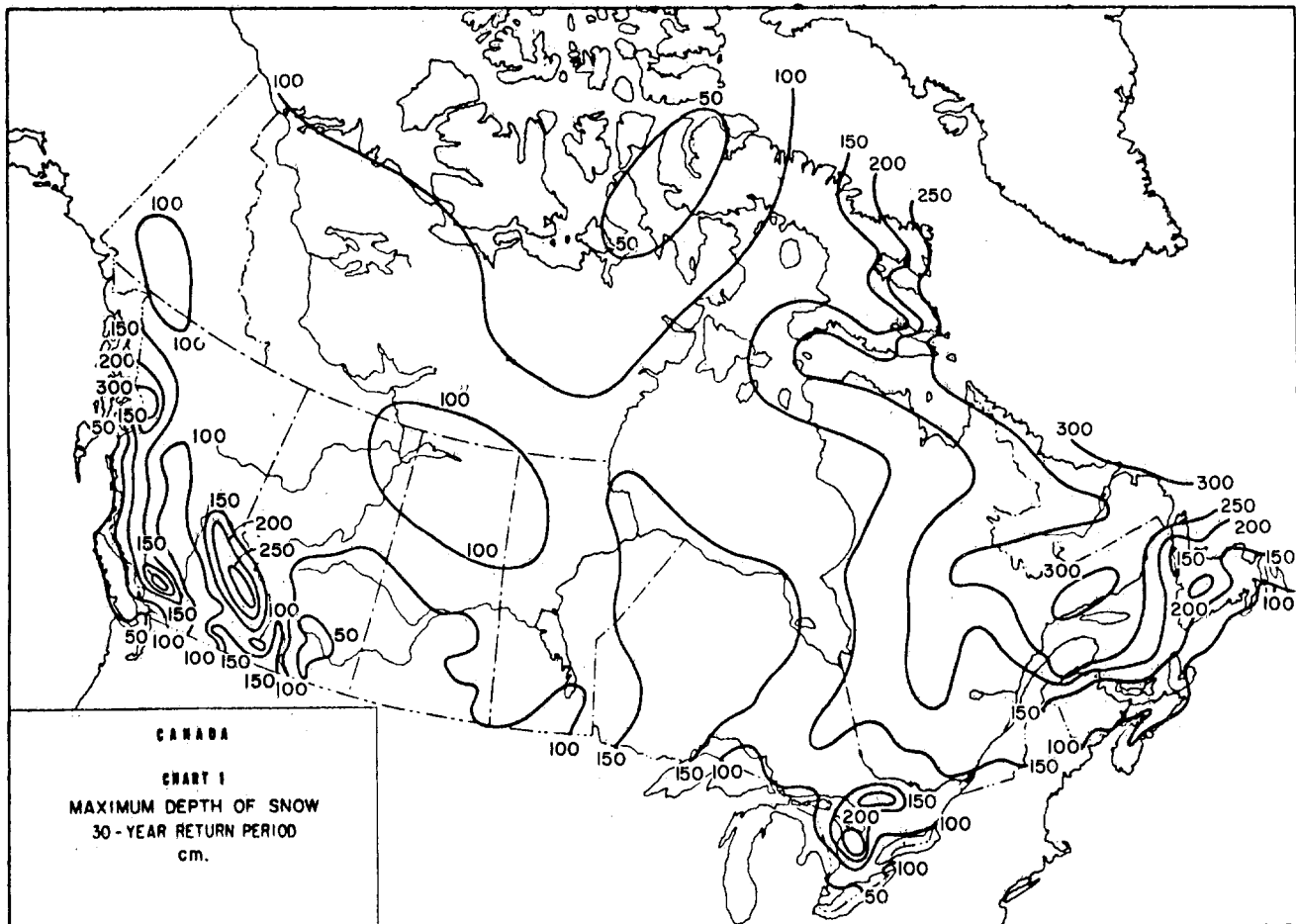
Figure 16-15. Maximum depth of snow for a 30-year return period for Canada expressed in metric units [Boyd, 1961].
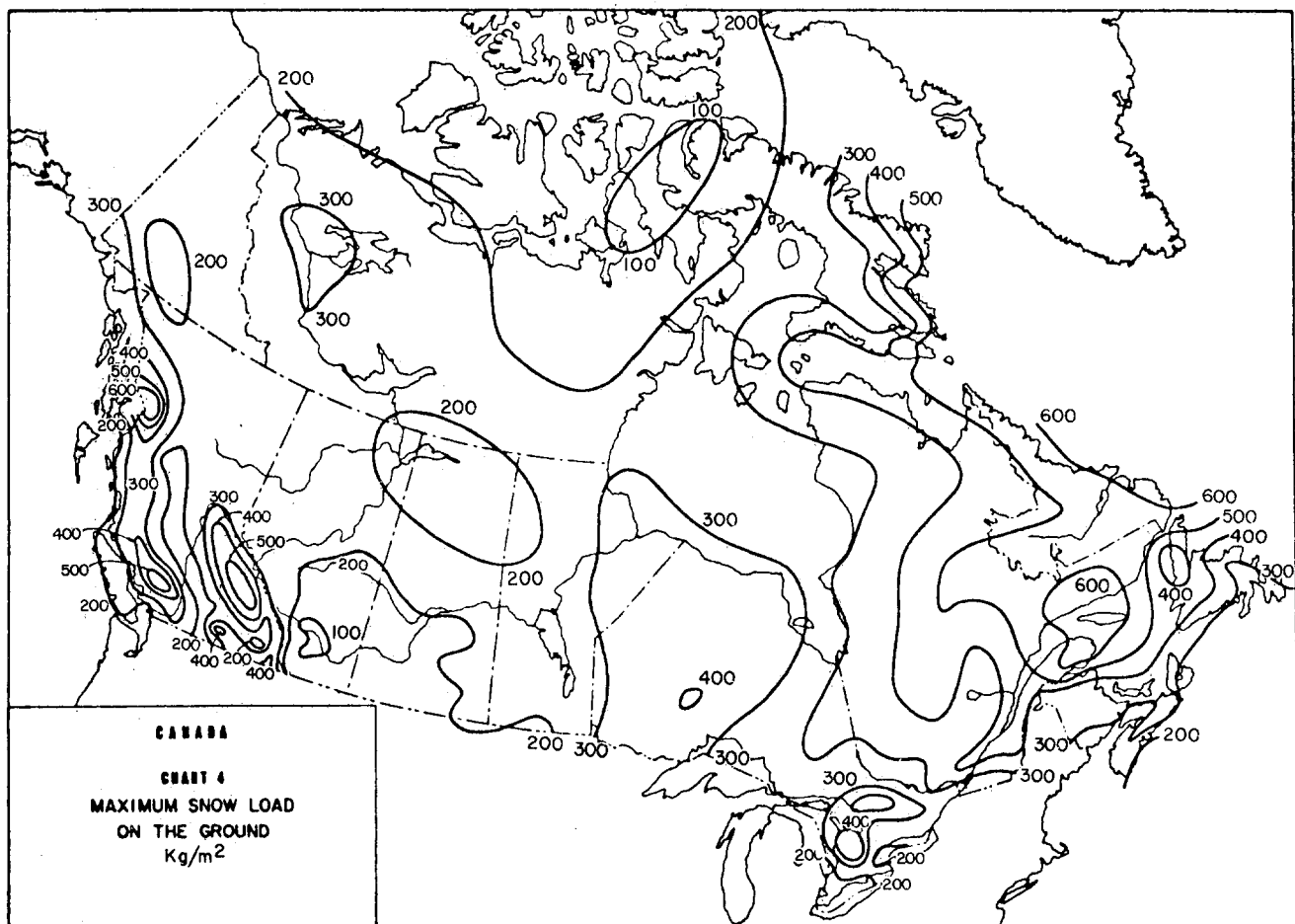
Figure 16-16. Estimated maximum snowload in Canada in a 30-year return period expressed in metric units [Boyd, 1961].

maximum depth would be expected to occur (a 63% chance) at least once. He also estimated the amount of rain that could occur and be retained by the snow. These findings are incorporated into Figure 16-16, which indicates that a maximum snow load on the ground of 600 kg/m^2 can occur in non-mountainous areas in eastern Canada. He tentatively indicates that snow loads on flat or low-slope roofs would be about 80% of the ground load based on limited observations. In a 1951 U.S. Weather Bureau study, the maximum non-mountainous ground snow load in the U.S. is estimated at 300 kg/m^2, and the 1 year in 10 maximum at 200 kg/m^2. Snowfall extremes in North America are considered to be as severe as anywhere in the world, so that these values are considered representative of non-mountainous worldwide extremes.

16.2.4 Ice Accretion on Surface Structures

Ice accretion, or icing, refers to ice accumulating on stationary objects located near the earth's surface. Such ice can disrupt transportation, cause power and communication outages, and result in severe damage to structures bearing

the burden of accumulated ice. Nevertheless, it remains one of the few meteorological conditions not quantitatively observed on a routine basis by any national weather service.

There are three basic types of ice formed by accretion in the atmosphere: glaze, hard rime, and soft rime. Glaze occurs most commonly when rain or drizzle freezes on objects. It is clear and nearly as dense as pure ice (which has a density of 0.917 g/cm^3). Hard rime is less transparent than glaze, and at times is opaque, depending on the quantity of air trapped in the ice. Its density varies from about 0.6–0.9 g/cm^3. Soft rime, which is white and opaque, is feathery or granular in appearance, with a density less than 0.6 g/cm^3. Rime ice, both hard and soft, is most often formed by the freezing of supercooled cloud or fog droplets. For this reason it is a localized phenomenon, occurring most frequently in mountainous areas or hilltops exposed to low, stratus type clouds, or on land areas adjacent to bodies of water.

Most of the information available on surface icing is for glaze; it is usually recorded because of extensive human distress or a large amount of damage. Even then, measurements have been subjective, non-standardized, and difficult to interpret. The most comprehensive study on the geographical distribution and frequency of glaze, worldwide,
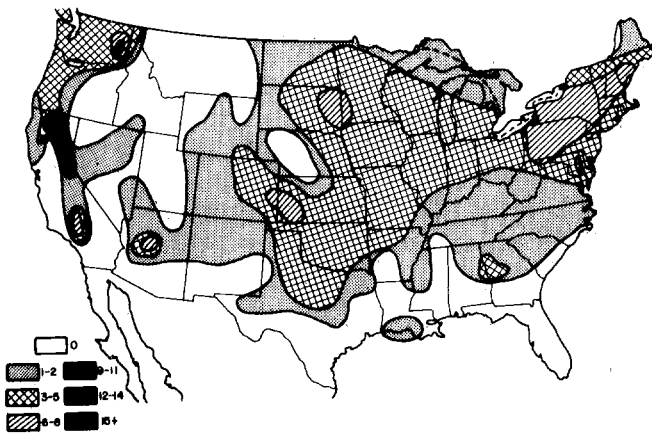
Figure 16-17. Number of times ice at least 1.25 cm thick was observed during the 9-year period of the Association of American Railroads Study [Bennett, 1959].
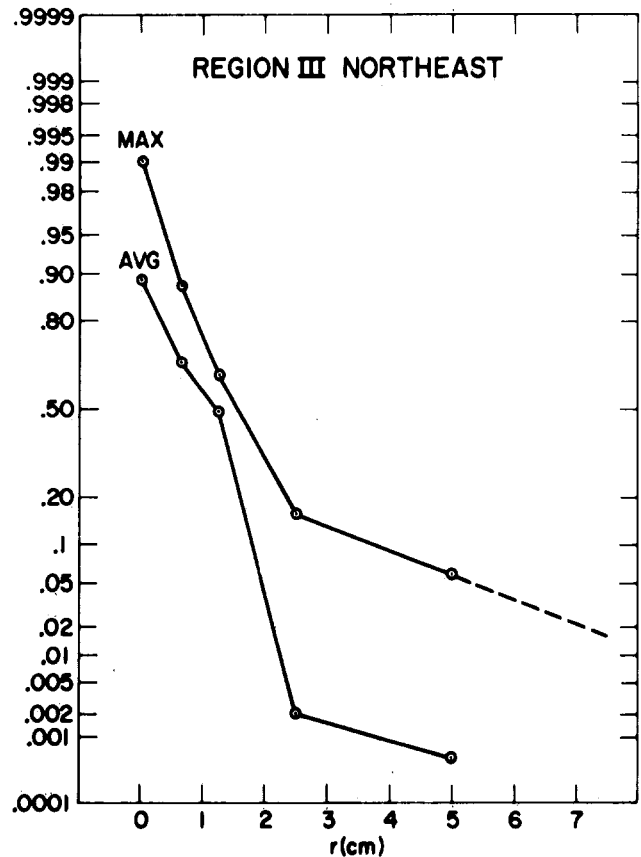

Figure 16-19. Estimated probability of ice thickness, r, occurring at least once in any year at a representative point in region III (AVG), and in the most severe part of region III (MAX) [Tattelman and Gringorten, 1973].

was done by Bennett [1959]. The information presented indicates that glaze is as frequent and as severe an occurrence in parts of North America as it is anywhere in the world. Figure 16-17 from that report shows the number of times that ice at least 1.25 cm in thickness was observed in the U.S. during a 9-yr period in a study by the Association of American Railroads. Although the length of record is short for climatological purposes, the relatively high frequency of heavy ice storms in the central and northeastern U.S. is supported by other data.

Tattelman and Gringorten [1973] reviewed many sources for information on ice storms in the contiguous U.S. for the 50 winter seasons from 1919-20 through 1968-69. The data were analyzed to determine the probability of occurrence of ice thicknesses in each of eight regions in the U.S. The regions shown in Figure 16-18 are areas with similar glaze characteristics subjectively determined on the basis of latitude, geography, climatology and the distribution of ice storms. Figure 16-19 shows ice thickness versus probability

of occurrence in a year for the northeast (region III in Figure 16-18), which had the greatest frequency of ice storms. The curve labelled AVG represents an average for all states in the region, whereas the curve labelled MAX represents the estimate for the state in the region with the highest frequency of ice storms. The authors stress the subjectivity involved in arriving at their estimates.

Eastern Canada, from Nova Scotia and Newfoundland northward to southern Baffin Island, has the highest frequency of freezing rain and drizzle in North America [McKay and Thompson, 1969]. Extreme ice storms in this area have produced accumulations of ice 20 to 40 cm in thickness. This is not surprising because the area is frequently subject to the passage of slow moving "mature" cyclones, and associated winds can exceed hurricane force (33 m/s). Strong winds increase the number of precipitation drops impinging on a vertical surface, so that the accumulation of ice can exceed the depth of precipitation by a factor of 3 or more.

Ice accretion is difficult to measure because the shape and size of the collecting surface, and its orientation to the wind can result in large differences. Furthermore, the configuration and density of ice on a surface are dependent upon a number of atmospheric variables. Tattelman [1982]

Figure 16-18. Regions of similar glaze characteristics [Tattelman and Gringorten, 1973].

16-21

Table 16-21. Mean and standard deviation of the ratios of the mass of ice on the 3-, 13-, and 50-mm diameter cyclinders to that on the 25 mm diameter cylinder.

Category	Cylinder Diameter (mm)	Mean	Standard Deviation
In-cloud icing	3.2	0.21	0.059
In-cloud icing	12.7	0.59	0.062
In-cloud icing	50.8	1.47	0.116
Freezing rain	3.2	0.18	0.041
Freezing rain	12.7	0.54	0.056
Freezing rain	50.8	1.65	0.091
Both combined	3.2	0.20	0.054
Both combined	12.7	0.57	0.063
Both combined	50.8	1.56	0.139

gives an overview on the dynamics of ice accretion and research in the field. He also presents an analysis of icing measurements on cylinders, for differing synoptic conditions, made during climatic chamber tests of an ice measurement system. Results include a comparision of the mass of ice that accumulates on cylinders which are 3, 13, 25, and 50 mm in diameter (Table 16-21).

16.2.5 Distributions of Precipitation Elements

Precipitation parameters vary appreciably with type of storm, geographic location, and even from storm to storm of the same type and in the same geographic region; for this reason, no model storms are presented in this section. However, individual profiles or averages that are derived from observations at several locations are given, and, wherever possible, the applicability and representativeness of the data are indicated. Great care must be taken in extrapolating the results to geographical regions that are characterized by a climatology which differs from that of the region from which the data were obtained.

16.2.5.1 Raindrop Size Distributions. Numerous equations have been proposed to express the size distribution of raindrops measured at the ground as a function of rainfall rate. They can all be expressed in the form

$$N_D \, \Delta D = N_o D^{-\alpha} \exp(-\Lambda D^{\,\beta}), \qquad (16.11)$$

where $N_D \, \Delta D$ is the number of drops per unit volume with diameters between D and D + ΔD, N_o is the value of N_D where the curve crosses the D = 0 axis, Λ is a parameter that depends on the type and intensity of the precipitation, and α and β are parameters which determine the shape of the distribution.
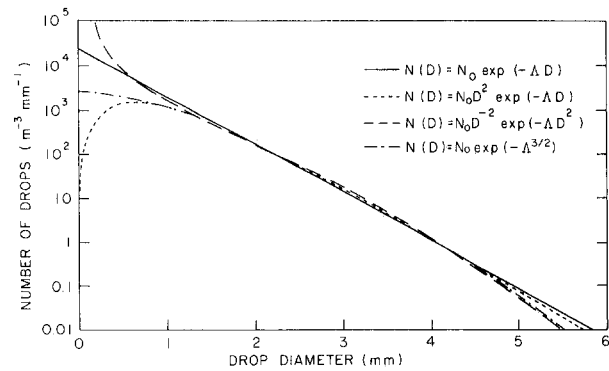
Figure 16-20. Four typical shapes of raindrop size distributions measured at the ground.

Examples of some drop size distributions are shown in Figure 16-20. When α = 0 and β = 1, Equation (16.11) reduces to the simple exponential distribution first proposed by Marshall and Palmer [1948]. This is shown in the solid line of Figure 16-20. This distribution was derived from data obtained in stratiform rain, and tends to overestimate the number of small drops. When α = 2 and β = 1, the resulting expression is an approximation to the log-normal distribution proposed by Levin [1954]. In this case, there is a realistic decline in the number of drops at the lower end of the spectrum. Setting α = −2 and β = 2 results in a gamma distribution first derived by Best [1950]. This distribution holds if, as some measurements indicate, the liquid water content per drop size interval follows an exponential distribution. The fourth distribution is one proposed by Litvinov [1956] for drizzle-type rains, setting α = 0 and β = 3/2. Although all the distributions in Figure 16-20 have been extended to 5-mm diameter drops (the usual maximum drop size observed), the distribution for drizzle-type rains should be truncated at approximately 2-mm diameter.

The total liquid water content M, the Rayleigh radar reflectivity factor Z, and the median volume diameter D_o can be expressed as weighted integrals of the size distribution. The weighting factor in deriving Z is D^6, while that for deriving M is $\pi/6 \, \rho D^3$, where ρ is the density of water in g/cm^3. Assuming an exponential distribution (α = 0, β = 1), and integrating between D = 0 and D = ∞ (an approximation sufficiently accurate for most purposes), we obtain

$$D_o = 3.67/\Lambda \qquad (mm) \qquad (16.12)$$

$$M = 10^{-3} \, \pi(\rho N_o/\Lambda^4) \; (g/m^3) \qquad (16.13)$$

$$Z = 720 \, N_o/\Lambda^7 \qquad (mm^6/m^3). \qquad (16.14)$$

Other parameters (for example, the median power diameter) can also be found using the appropriate weighting factor. Such integrations, however, become cumbersome for distributions in which $\alpha \neq 0$ and $\beta \neq 1$. For this reason,
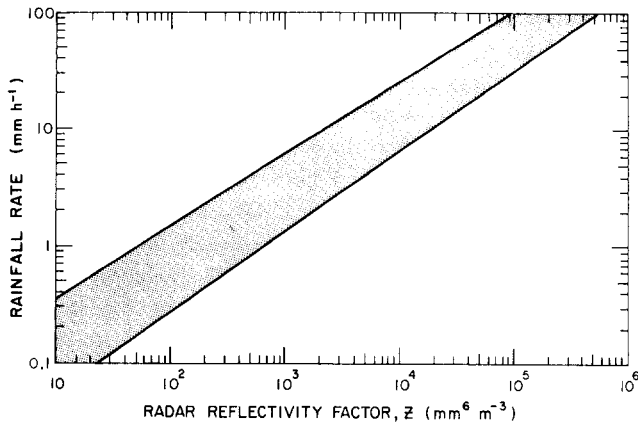
Figure 16-21. Radar reflectivity factor vs rainfall rate (shaded area is the range of the measured relations).

the simple exponential distribution is often used, even when it is known to deviate from measured size distributions.

Numerous empirical relations have been proposed expressing radar reflectivity as a function of rainfall rate or liquid water content, or rainfall rate as a function of liquid water content. The relations differ significantly, according to the location and type of precipitation. Figures 16-21, 16-22, and 16-23 summarize the results of measurements from several observers. The shaded area of Figure 16-21 encompasses the range of measured relations between radar reflectivity and rainfall rates, and illustrates the variability that can be encountered. Figure 16-22 expresses the same data in terms of radar reflectivity versus liquid water content. If rainfall rate is the measured quantity, Figure 16-23 can be used to find the expected range of liquid water content.

16.2.5.2 Snowflakes. Gunn and Marshall [1958] found that an exponential law similar to that shown by the solid line of Figure 16-20 was applicable to the size distribution of aggregate snowflakes. The spectral parameters in snow are related to the precipitation rate by
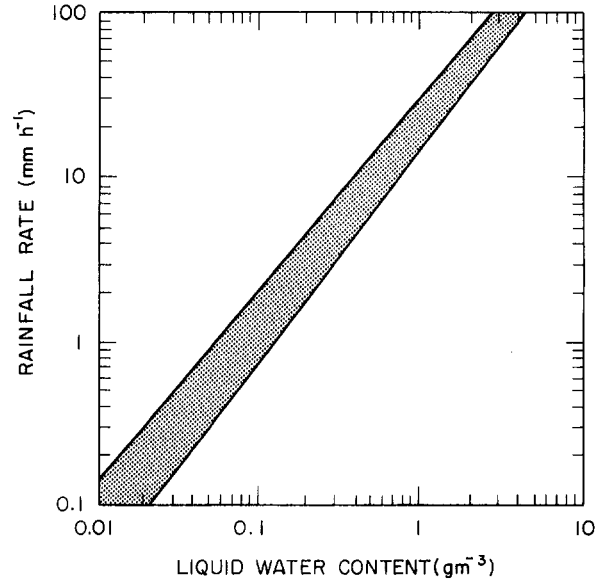
Figure 16-23. Liquid water content of precipitation vs rainfall rate.

$$N_D \, \Delta D = N_o \exp(-\Lambda D) \qquad (16.15)$$

$$\text{where} \quad N_o = 3.8 \times 10^3 \, R^{-0.87} (\text{m}^{-3}\text{mm}^{-1}) \qquad (16.16)$$

$$\Lambda = 2.55 R^{-0.48} \qquad (\text{mm}^{-1}), \qquad (16.17)$$

where R is precipitation rate in millimeters of water per hour. For snowflakes, the diameter D refers to the melted spherical diameter of the snowflake.

Recent measurements [Lo and Passarelli, 1982] of the evolution of snow size spectra with decreasing altitude demonstrate the existence of three growth regimes. At the top of the snow region, growth is by deposition only. The size distribution is typified by curve 1 in Figure 16-24. Progressing down through the atmosphere, N_o increases while Λ remains constant. Then aggregation begins, and there is a rapid decrease in both N_O and Λ. Curve 2 of Figure
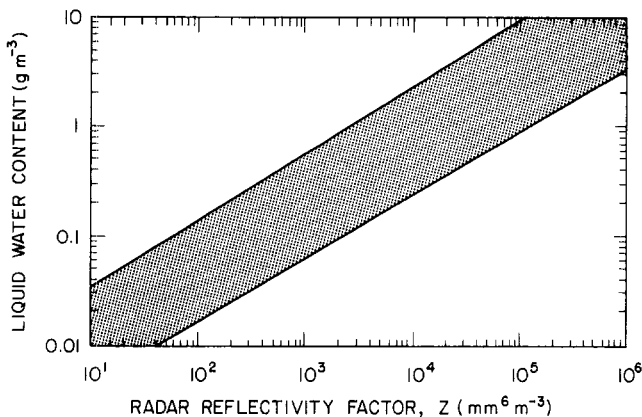

Figure 16-22. Radar reflectivity factor vs liquid water content of rain (shaded area is the range of observed relations).
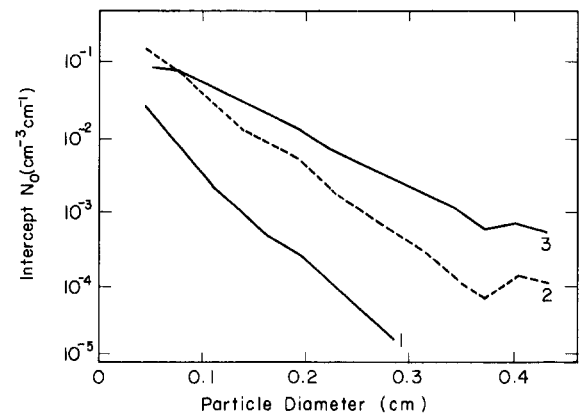

Figure 16-24. Snow size spectra as a function of growth regime and altitude.

16-23

16-24 illustrates a typical spectrum during this phase. Finally, breakup counteracts the effects of both deposition and aggregation, and the distribution remains constant, with a slope and intercept typical of curve 3 in Figure 16-24. The minimum value of Λ observed in the atmosphere is approximately 10 cm^{-1}.

16.2.5.3 Distribution of Precipitation Elements with Height.
The vertical distribution of precipitation parameters can be inferred from the vertical distribution of radar reflectivity, using the appropriate conversions. When the precipitation particles are ice crystals or snowflakes, it is necessary to determine the type of particle and general size regime before choosing the equation to convert the particle size or mass to the equivalent diameter or mass of a liquid drop. Table 16-22 shows factors for converting from a physical length, L, of the solid particle to an equivalent spherical diameter, D. A power relation of the form $D = a L^b$ has been assumed, and a and b are listed for general particle types.

The maximum size of hydrometeors is related to the slope of the distribution by the empirical relation

$$D_m \Lambda \approx C , \qquad (16.18)$$

where D_m is the maximum equivalent diameter, Λ is the slope of the exponential distribution, and C is a constant dependent on the type of hydrometeor. Using data collected over several years, AFGL scientists have found that average values of C range from 12 for ice crystals to 10.5 and 9 for small and large snow, respectively, and 7.5 in rain.

If an exponential distribution is assumed, the particle size distribution of hydrometeors can be completely described from the slope of the distribution (Λ), the intercept (N_o), and the total number of drops (N_t), which depends upon the minimum and maximum particle size assumed. The size is dependent upon the slope of the distribution as shown in Equation (16.18).

Table 16-23 gives the characteristics of average distributions for various hydrometeor types. In each case, N_t, N_o and Λ are expressed as power functions of M, the total water content in g/m^3. The units of Λ are 1mm^{-1}; of N_o, m^{-3}mm^{-1}; and of N_t, m^{-3}. Expressions connecting other sets of parameters may be obtained from this table and manipulation of Equations (16.12) through (16.14), or integration of Equation (16.11) with the appropriate weighting factor.

Table 16-22. Factors for converting from physical length, L, to equivalent diameter, D.

Particle type	Size range	a	b
Ice crystals	<0.2mm	0.438	1.000
	≥0.2mm	0.256	0.667
Small snow	<0.5mm	0.370	0.670
Large snow	≥0.5mm	0.400	0.782

Height variations of gross parameters such as water content or radar reflectivity factor are functions of type of storm and geographic location. However, when there is a sufficient body of data for a particular region, it is possible to define a climatological model. Two such models are shown in Figures 16-25 and 16-26. Figure 16-25 shows the results for stratiform storms at Wallops Island, Virginia. The dotted line may be considered an average vertical profile of liqiud water content for stratiform storms at this location, and the solid lines indicate the variability of the data. Figure 16-26 shows the same analysis for convective storms at Wallops Island. The major difference between these two figures is the high water content between 2 and 4 km in convective storms. This storage zone aloft is characteristic of most convective storm situations, regardless of location. Stratiform storms, on the other hand, are characterized by relatively smooth vertical profiles of liquid water content, with only a slight bulge at the melting zone.

16.2.5.4 Extreme Values of Liquid Water Content.
Measurements of the maximum concentration of liquid water in severe convective storms have not been made on a systematic basis. Isolated reports of concentrations as high as 30 g/m^3 [Sulakvelidze et al., 1967] and even 44 g/m^3 [Roys and Kessler, 1966] are found in the literature. There have been occasions when investigators have suspected the occurrence of abnormally high concentrations but lacked the
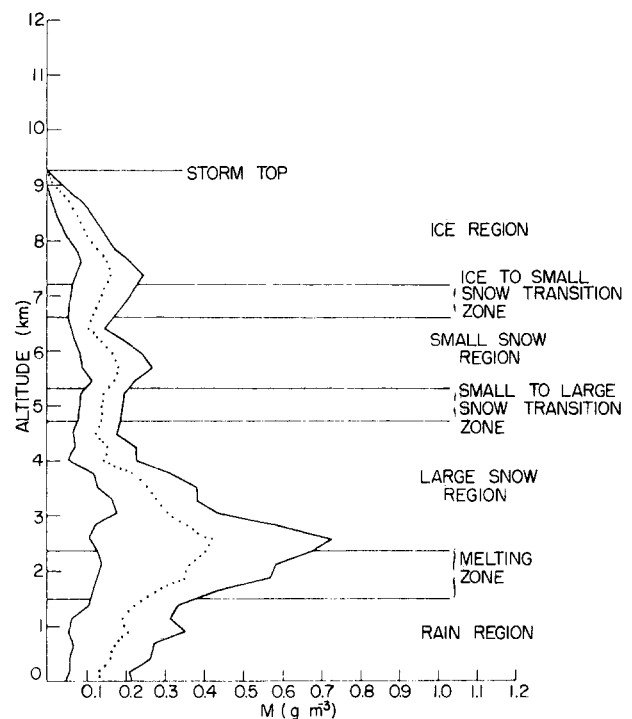

Figure 16-25. Liquid water content in grams per cubic meter vs altitudes in kilometers for stratified-storm situations (dotted line is the mean and the solid lines represent plus and minus 1 standard deviation).

Table 16-23. Distribution parameters as a function of hydrometeor type and of total mass, M (N_t is the total number of particles per cubic meter; N_o and Λ are the zero intercept and slope for an exponential size distribution).

Hydrometeor Temp. Range Min. Diameter Sub Types	$N_t = e\ M^f$		$N_O = i\ M^j$		$\Lambda = k\ M^q$	
	e	f	i	j	k	q
Ice Crystal <248 K d = 0.055 mm						
Tropical	61522	0.073	514541	−0.583	6.343	−0.394
Temperate	98719	0.303	1104536	−0.201	7.675	−0.299
Small Snow 258 to 243 K d = 0.065 mm						
Tropical	50723	0.032	403471	−0.739	5.968	−0.431
Temperate	19727	0.266	109002	−0.148	4.295	−0.287
Large Snow 273 to 253 K d = 0.065 mm						
Tropical	4122	−0.373	10839	−1.089	2.403	−0.522
Temperate						
Agg. of Plates	6833	0.384	23966	0.096	2.930	−0.226
Agg. of Stellars & Dendrites	1649	0.155	3251	−0.202	1.778	−0.301
Agg. of Columns & Bullets	14005	0.455	67147	0.164	3.791	−0.209
Rain > 273 K d = 0.1 mm						
Tropical	4033	0.443	12619	0.161	2.471	−0.210
Temperate						
Widespread	1934	0.133	4382	0.018	1.897	−0.245
Drizzle	5850	0.366	21509	0.017	2.824	−0.246
Thunderstorm	649.9	0.310	945.6	0.017	1.293	−0.245

equipment for measuring them. In considering many aspects of the storm, Roys and Kessler could not find evidence which indicated that the measured concentration 44 g/m³ should be either rejected or accepted. Omitting the value of 44 g/m³, their 26 other measurements of the maximum liquid water content in Oklahoma thunderstorms fit very well the distribution illustrated in Figure 16-27. According to this distribution, the probability that the maximum water content, M, in an Oklahoma thunderstorm will exceed a given value, x, is

$$P(M > x) = \exp(-x^2/64), \qquad (16.19),$$

where M and x are in g/cm³.

It is dangerous to extrapolate from such a small sample. Nevertheless, the actual occurrence of extreme values of liquid water concentrations probably follows the general shape of Figure 16-27 with possible modification of the constants in the distribution function. Figure 16-27 indicates that 75% of Oklahoma thunderstorms have maximum liquid water contents exceeding 4.3 g/m³, and that liquid water contents in excess of 9.4 g/m³ occur in only 25% of the storms. Substitution into Equation (16.19) shows the values of 30 g/m³ or higher are literally "one in a million" occurrences in Oklahoma thunderstorms, and the occurrence of a value of 44 g/m³ has a probability of 10^{-12}.

It is of interest to compare these extreme values of water content to the water content corresponding to a record rain-
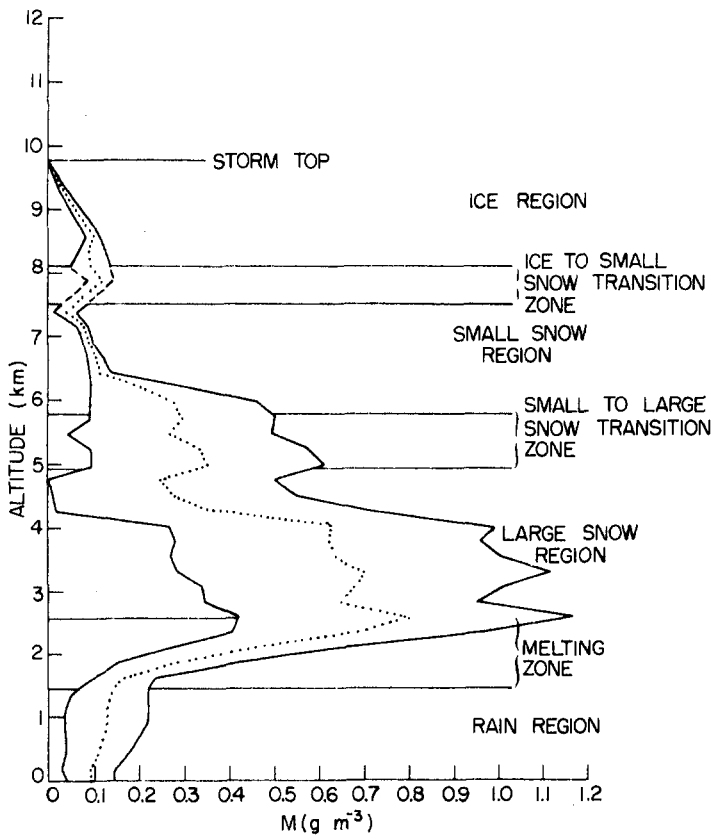
Figure 16-26. Liquid water content in grams per cubic meter vs altitudes in kilometers for convective-storm situations (dotted line is the mean and the solid lines represent plus and minus 1 standard deviations).

Figure 16-27. Probability of maximum liquid water content within Oklahoma thunderstorms.

fall rate. Over a 1-min interval, the world record rainfall amount is 3.1 cm; this fell at Unionville, Maryland, in 1956 [Riordan, 1974]. Assuming a Marshall-Palmer distribution, this rainfall rate corresponds to a liquid water content of approximately 55 g/m^3. Consequently, extremely large values of water content (for example, greater than 30 g/m^3) may occur on rare occasions either at the surface or aloft in severe thunderstorms.

16.3 CLOUDS

16.3.1 Surface Observations

Cloud observations taken regularly by ground observers at weather stations throughout the world primarily contain the following information:

(1) Visual estimate of total amount of sky covered by clouds,

(2) Cloud ceiling, which is the estimated or measured height above ground of the lowest layer of clouds that cover more than half of the sky.

Secondarily, visual estimates of amount and height of bases of individual cloud types and layers are reported. But because low clouds obscure higher clouds, it is often impossible to obtain accurate information on the distribution of clouds at the higher levels. Studies of the accuracy of visual cloud observations show that the greatest errors occur in estimating cloud amounts when the sky is 3/10 to 7/10 covered. These errors however, tend to average out over long periods. The average error in visual estimations of cloud heights ranges from 300 m for clouds at 750 m, to 1500 m for clouds with bases near 7 km. At many points, however, particularly at airport stations, ceiling heights can be measured with a higher degree of accuracy with ceilometers, clinometers, or balloons.

Observed values for a particular time give amount of sky covered but not the cloud distribution. For example, if 5/10 cloud cover is reported, one large cloud formation may cover half of the sky or small individual cloud cells may be equally distributed over the sky. There is no direct way to obtain the geometry of clouds in the sky from the reported standard observations.

There can be considerable variation in the frequency of occurrence of given cloud amounts and ceiling heights between stations located within several kilometers of each

other. Because local topographical effects are the primary cause of such variations, caution must be used in applying climatological data on clouds of one or more stations to an entire region, particularly in mountainous and coastal regions.

16.3.1.1 Summaries of Surface Observations. Tabulations of surface cloud observations are available for stations in most areas of the world. A *Guide to Standard Weather Summaries and Climatic Services* [NOC, 1980] has been prepared by the Naval Oceanography Command in Asheville, North Carolina, which lists some 23 types of cloud summaries. The station list includes locations in various countries, continents, islands, and oceans. There are close to 10 000 weather stations around the world, although not all of them provide routine observations of clouds. Among the better summaries of cloud information are those prepared by the United States Air Force Environmental and Technical Applications Center (USAF/ETAC) as *Revised Uniform Summaries of Surface Weather Observations* (RUSSWO). Similar summaries are issued by the Naval Weather Service as *Summary of Meteorological Observations, Surface* (SMOS), and *Summary of Synoptic Meteorological Observations* (SSMO).

Table 16-24 is a sample of the frequencies (in tenths) of *sky cover*, from clear (0/10) to overcast (10/10) at a single station (Bedford, Mass.) in a single month (January) for eight 3-h periods of the day. It also shows the average sky cover, but does not subdivide the cloud cover by height of clouds. Table 16-24 also shows the frequencies for the midseason months for all hours combined.

Table 16-24. Sample percent frequencies of sky cover, by tenths. (example is for Bedford, Mass).

Hours	January Sky Cover (tenths)											Avg. Sky Cover (tenths)
	0	1	2	3	4	5	6	7	8	9	10	
00–02	34	2	3	3	2	1	2	3	2	2	46	5.5
03–05	32	2	3	3	2	2	3	3	3	2	45	5.7
06–08	21	5	4	4	3	2	2	3	5	4	47	6.3
09–11	17	5	5	4	4	2	2	3	6	4	48	6.5
12–14	16	4	5	4	4	3	3	4	6	5	46	6.6
15–17	16	6	5	5	3	3	3	4	5	5	45	6.4
18–20	28	3	5	4	3	2	3	3	4	2	43	5.7
21–23	32	3	4	4	2	1	3	3	4	2	42	5.5
Mid-season Month	Seasonal Sky Cover											
Jan	24	4	4	4	3	2	3	4	4	3	45	6.0
Apr	18	4	4	5	4	3	3	4	7	4	44	6.4
Jul	15	5	6	7	6	5	5	6	9	5	31	5.9
Oct	30	5	5	5	4	3	3	4	5	4	32	5.0

In the RUSSWO, as in many summaries, the frequencies are given for ceiling heights jointly with the visibility in matrix form. Table 16-25 is a sample of ceiling height information as gleaned from eight such matrices for Bedford, Mass., one for each 3-hour period. Table 16-25 also shows the cumulative percent frequencies of ceilings for the mid-season months for all hours combined.

Table 16-25. Sample percent frequencies of ceiling heights equal to or higher than, including ceiling unlimited (example is for Bedford, Mass).

|	January Ceiling (m)											
Hour	6100	4900	3700	3000	2400	1800	1200	900	600	300	150	30
00–02	55	55	58	60	62	66	72	76	80	86	92	98.4
03–05	51	52	55	57	60	63	70	74	80	86	93	98.3
06–08	48	48	53	56	60	63	70	74	79	86	94	98.9
09–11	50	51	56	59	63	66	71	75	80	86	94	99.8
12–14	50	51	56	60	64	66	70	75	80	86	94	99.4
15–17	52	53	58	61	64	67	72	77	81	86	93	99.2
18–20	56	57	60	62	65	67	71	76	81	87	94	99.2
21–23	57	57	60	62	64	67	72	77	81	87	94	99.1
Mid-season month	Seasonal Ceiling (m)											
	6100	4900	3700	3000	2400	1800	1200	900	600	300	150	30
Jan	52	53	57	60	63	66	69	76	78	86	94	99.0
Apr	49	50	53	56	60	64	73	77	81	88	95	99.5
Jul	61	62	68	72	75	77	82	85	88	92	97	99.5
Oct	62	62	65	68	70	72	77	81	84	89	95	98.6
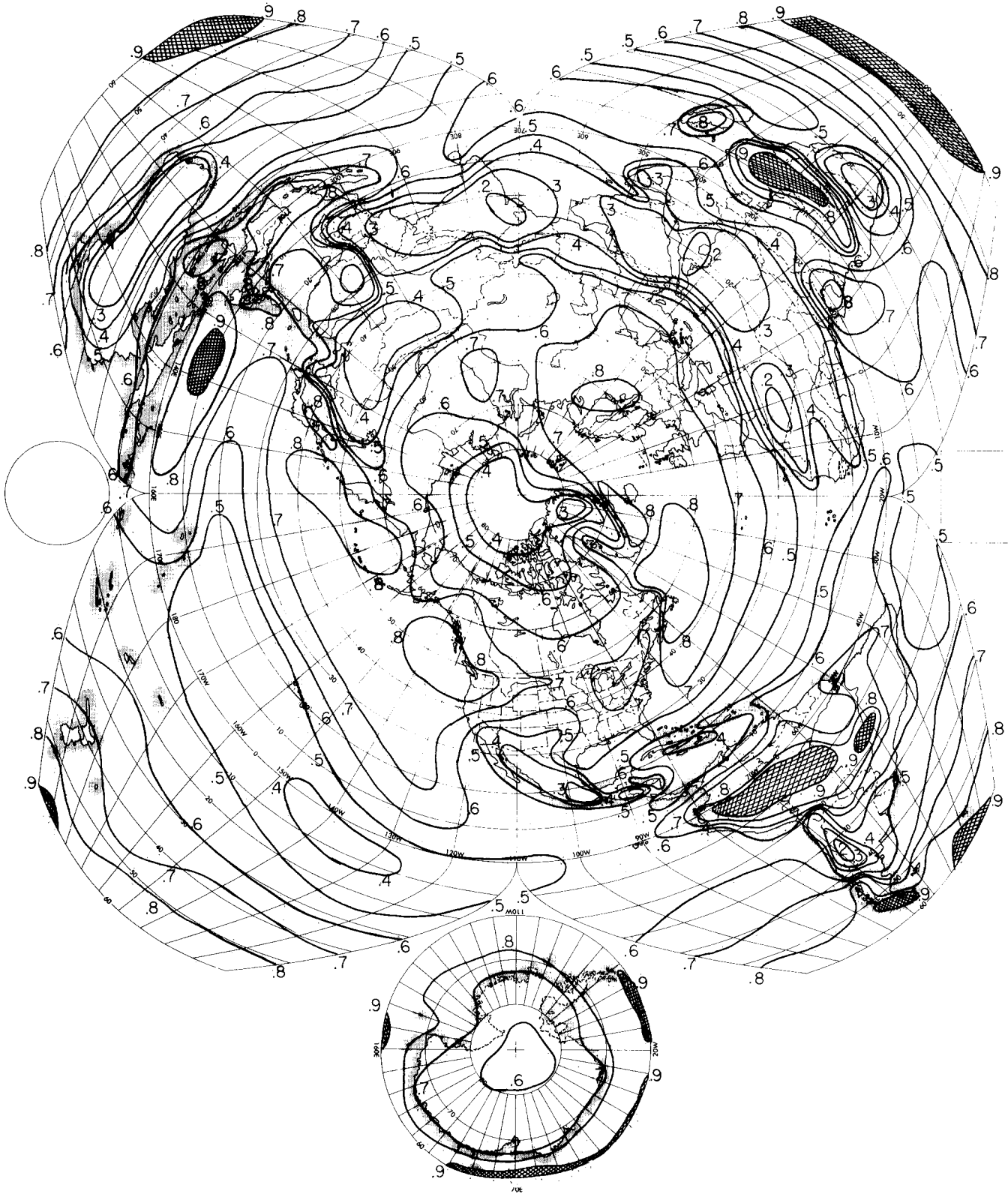
Figure 16-28. Mean sky cover, January, 1200–1400 LST.
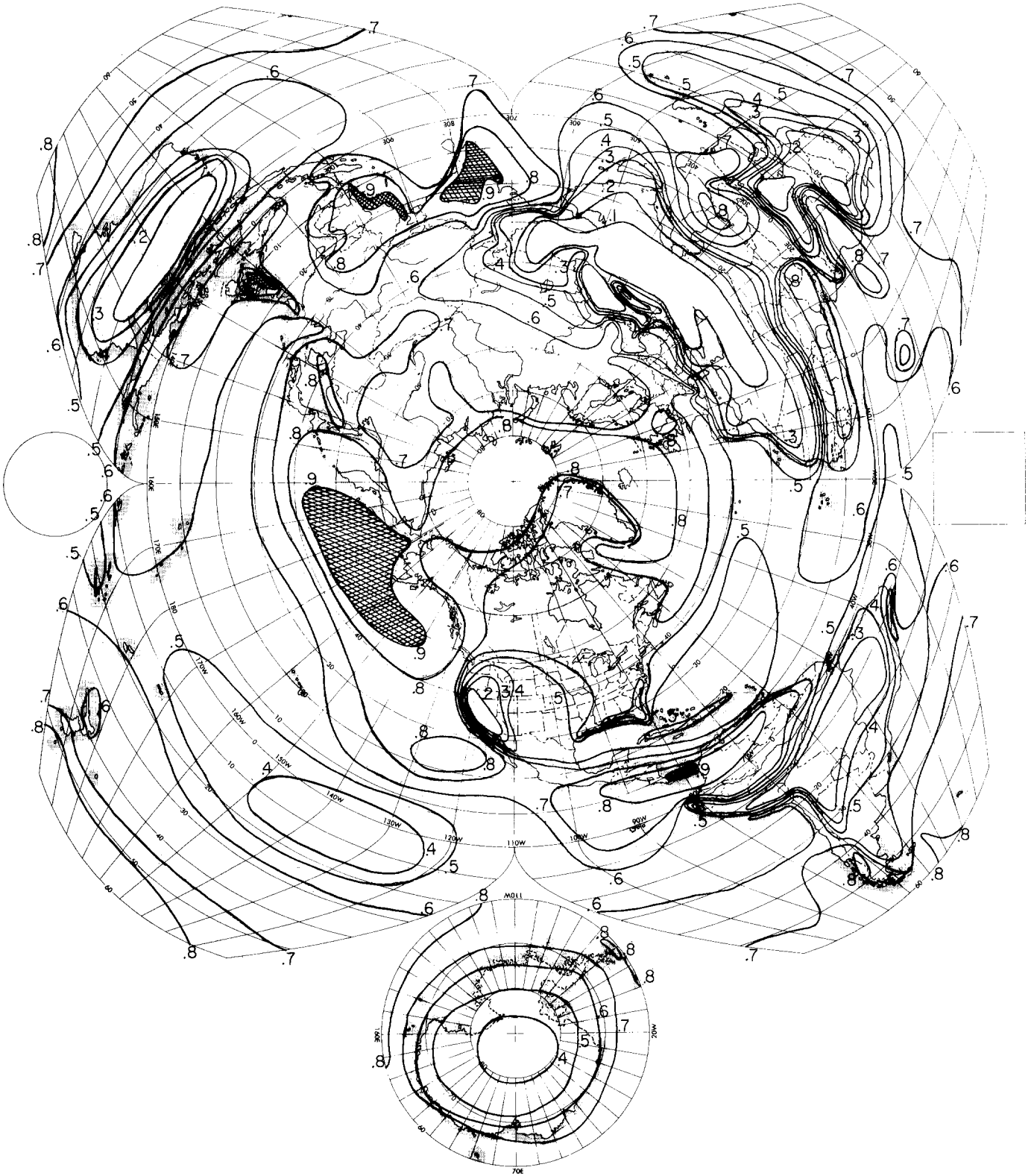
Figure 16-29. Mean sky cover, July, 1200–1400 LST.

16.3.1.2 Global Sky Cover. While there are numerous tabulations of sky cover compiled from surface observations, there are relatively few maps. One of the sources for these maps is the chapter "Climatology" by Landsberg [1945] in the *Handbook of Meteorology*. The chapter has six world maps of sky cover, one for every other month beginning with January. Figures 16-28 and 16-29 show average cloudiness for 1200–1400 LST in January and July, respectively, based on Landsberg's charts; subsequently published tables of the National Intelligence Survey, RUSSWO, SMOS and SSMO; and data collected at the Woods Hole Oceanographic Institute for the Atlantic and Indian oceans.

Mean sky cover is significantly correlated with the frequency of clear and of overcast conditions. Table 16-26 presents a sample of RUSSWO information for some U.S. stations; it contains the percent frequencies of sky cover, from clear to overcast, in January at noontime. Among these stations the mean sky cover ranges from 4.7 to 8.4 tenths. For low mean sky cover the frequency of clear skies is high and the frequency of overcast low. The opposite is true for a high mean sky cover. In extra-tropical regions the incidence of 1/10 to 7/10 sky cover remains generally low. However, the U-shaped distribution is less marked in the summer months (Table 16-24). In tropical and sub-tropical regions partial sky cover also is more frequent at the expense of clear and overcast. This is evident from the frequencies for Key West, Florida, and is particularly well illustrated by the data from Diego Garcia in the Indian Ocean at latitude 7° south (Table 16-26).

16.3.1.3 Modeling of Cloud Distributions. In the following presentations a distinction is made between the terms *cloud cover* and *sky cover*. Sky cover is an observer's view of cover of the sky dome, whereas cloud cover can be used to describe areas that are smaller than the floor space of the sky dome, or larger.

Cloud Cover Models. There have been several alternative mathematical formulas proposed for the probability distribution of sky cover. Each uses the variable (x) ranging from zero, for clear, to 1.0 for overcast. Each model is claimed to have versatile statistical characteristics to simulate U-shaped curves of sky cover. That is, large frequencies of clear and/or overcast skies, with small likelihoods of partial cover, can be fitted; yet the models also will fit the bell-shaped distributions in which the sky cover is mostly scattered to broken.

Alternative 1: The Beta distribution is an early cloud model [Falls, 1973] whose density function is given by

$$f(x) = \frac{\Gamma(a + b)}{\Gamma(a) \Gamma(b)} x^{a-1}(1 - x)^{b-1};$$
$$0 \le x \le 1, a,b > 0 . \tag{16.20}$$

Falls gives pairs of values of the two parameters in some 29 regional types that cover the world, for the four mid-season months, for two times of the day.

Alternative 2: More recently, Somerville and Bean [1979] have used a model called the S-distribution in which the cumulative probability F(x) of sky cover (x) is estimated by

Table 16-26. Percent frequencies of sky cover, by tenths, at a representative sample of stations. (For uniformity, the cases are all for January 1200 LST.)

| Station | \multicolumn{11}{c|}{Sky Cover (tenths)} | Mean Sky Cover (tenths) |
	0	1	2	3	4	5	6	7	8	9	10	
Extra-tropical												
Phoenix, Ariz.	33	6	4	4	3	3	4	5	7	5	26	4.7
Washington, D.C. (Dulles Airport)	22	8	6	3	3	3	2	3	6	4	40	5.7
Bridgeport, Conn.	21	3	4	5	4	2	3	5	6	6	41	6.2
Austin, Texas	18	5	4	3	3	3	3	5	6	6	44	6.4
Chicago, Ill.	14	4	4	3	3	3	2	5	6	6	50	6.9
Great Falls, Mont.	11	4	3	3	3	2	3	5	8	8	50	7.3
Boise, Idaho	11	4	3	3	2	2	2	4	5	6	58	7.5
Niagara Falls, N.Y.	3	3	3	3	3	3	2	4	9	8	59	8.2
Seattle, Wash.	5	2	2	2	1	2	2	4	9	7	64	8.4
Sub-tropical and tropical												
Key West, Florida	14	9	10	12	8	8	4	7	9	7	12	4.7
Diego Garcia 7°18′S, 72°24′E	0	0	0	4	5	7	6	16	18	14	30	7.8

$$\hat{F}(x) = 1 - (1 - x^\alpha)^\beta; \qquad (16.21)$$
$$0 \leq x \leq 1 , \alpha,\beta > 0 .$$

Pairs of values of the two parameters (α, β) have been determined to make the distribution $F(x)$ fit the data in the sky-cover summaries; they have been published for some 23 stations around the world, for each of eight periods of the day in each month of the year. The procedure has been to use 10 climatic cumulative frequencies $F(x_i)$ of sky cover for $x_i = 0.05(0.1)0.95$. A first guess is made for α, and β is then estimated by method of least squares:

$$\beta = \frac{\Sigma\{\ell n \ [1 - F(x_i)] \cdot \ell n[1 - x_i^\alpha]\}}{\Sigma\{\ell n[1 - x_i^\alpha]\}^2}. \qquad (16.22)$$

After the pair of values (α, β) are entered into the basic equation to obtain the estimates $\hat{F}(x_i)$, the sum of squares of the differences between $\hat{F}(x_i)$ and $F(x_i)$ is obtained. The best values for the parameters (α, β) are those that minimize the sum of squares of errors. These were determined by trial and error, such that the best pair of values for the sky cover at Bedford, Mass., in January at noontime, were found to be $\alpha = 0.1468$, $\beta = 0.1721$. These estimates are different from those in Table 16-24 by rmse $= 0.01$.

In the above-mentioned models, strictly speaking, the probabilities of absolutely clear and of complete overcast are each computed to be zero; hence they are not truly realistic. The difficulty is overcome, in practice, by stipulating that the integration for clear be taken from zero cover to 0.5 tenths, for overcast from 9.5 tenths to 10 tenths. There is another difficulty, however, in that each solution is given for the sky dome as seen by a ground observer, considered to have a radius of 28 km. The above alternatives have not been developed to give cloud-cover distribution for varying areal coverage. However, simplicity is in their favor, especially with the S-distribution, which is readily programmed on a desk-top computer.

Alternative 3: A *"Model B"* for linear and areal coverage of a weather element has been described recently [Grin-

gorten, 1979] which, like the above models, requires two parameters for a description of the probability distribution of cloud cover. The parameters in Model B have physical meaning. One parameter (P_o) is the mean cloud cover as given in RUSSWO and other climatic summaries; it is taken to be the single-point probability of a cloud intercept when looking up from the ground. The second parameter (r), known as the *scale distance*, is the distance between two stations whose correlation coefficient of cloud covers is 0.99. At Bedford, Mass., it varies from 0.5 km in summer noontime to as much as 10 km in winter midnight. Regrettably, as developed so far, estimations of the probability of cloud cover by this model must be made by use of 11 charts as published [Gringorten, 1979]. It does not yield estimates succinctly by formula. On the other hand, Model B avoids the difficulties of the previous two alternatives by providing finite estimates of all-clear and full overcast for varying areal extent. As an example, Table 16-27 shows the percent probability of cloud cover at Bedford, Mass., January noontime; the parameter values are $P_o = 0.66$, and $r = 2.6$ km. In Table 16-27 the cloud cover is given, not only as a ground observer sees it, but also for a small area of 100 km^2 and for a large area of 100 000 km^2. A small area is likely to be either all-clear (0/10) or overcast (10/10), but a large area is nearly always partially covered. For the ground observer's sky cover, the estimates differ from those in Table 16-24 by rmse $= 0.02$.

Ceiling Model. The *Burr curve* provides one of the best models for ceiling height cumulative distributions:

$$\hat{F}(h) = 1 - \{1 + (h/c)^a\}^{-b} ; a,b,c > 0, \qquad (16.23)$$

where h is the ceiling height and a,b,c are parameters.

At the University of Florida [Bean et al., 1979] sets of values for a, b, and c have been determined (for each of eight periods of the day in each month of the year at some 23 stations around the world) to make the estimated distributions, $\hat{F}(h)$, fit the data for some 30 ceiling heights as

Table 16-27. An example of model estimates of percent probabilities of cloud cover, by tenths, depending upon size of the area (example is for Bedford, Mass., January 1200 LST).

Areal Size (km^2)	Cloud Cover (tenths)											Mean Cloud Cover (tenths)
	0	1	2	3	4	5	6	7	8	9	10	
100	29	1	1	1	2	1	1	2	2	1	59	6.6
2424 (Observer's sky dome)	16	4	5		3	3	5	4	6	9	41	6.6
100 000	0.5	3	4	7	9	9	12	13	16	19	8	6.6

given in the climatic summaries. In this procedure, a rounded figure is chosen for c, such as 300, 600, or 3 000 m. Trial estimates for a and b are then made to minimize the sum of squares of the differences between the model estimates $\hat{F}(h)$ and the cumulative frequencies F(h) of the climatic summaries. An initial trial estimate of a can be made by a linearization of the Burr curve through Taylor expansion, resulting in

$$a = \frac{\left[N \sum x_i y_i - \sum x_i \sum y_i \right]}{\left[N \sum x_i^2 - (\sum x_i)^2 \right]}, \quad (16.24)$$

where $x_i = \ell n(h_i/c)$, $y_i = \ell n\, F(h_i)$, and N is the number of ceiling heights for which the climatic tables give the frequencies $F(h_i)$. Corresponding to each trial estimate of a,

$$b = \frac{[- \sum \ell n\, \{1 - F(h_i)\}\, \ell n\, \{1 + (h_i/c)^a\}]}{\sum \{\ell n(1 + (h_i/c)^a\}^2}. \quad (16.25)$$

For Bedford, Mass., January noontime, values found were a = 1.1678, b = 0.1927 when c = 0.305 km, giving the estimates of probability that differed from those in Table 16-25 for 1200–1400 hours by rmse = 0.01.

16.3.2 Cloud Cover in Layers Aloft

Nephanalysis, concerning the type, amount, and scatter of clouds both in the horizontal and vertical directions, is important, particularly in connection with line-of-sight requirements. For example, knowledge of the probability of cloud-free lines-of-sight (CFLOS) from one level of the atmosphere to another at selected angles of elevation, can be vital to electro-optical communication systems. Although there is now a sizable body of literature on this subject, the statistics are none too satisfactory. Clouds are not only volatile but are often hidden by other clouds, so that an analysis of cloud presence, or a climatology of cloud frequencies as a function of level or layer above the ground is crude and speculative, especially if information is limited to the observations from the ground. An observer sees the "sky dome" with an uncertain radius, assumed to be 27 km in the following discussion and analysis.

A valuable study on the frequency of occurrence of clouds in the vertical was based on observations from aircraft over Germany [deBary and Moller, 1963]. It resulted in estimates of the average cloud cover as a function of altitude and the thickness of the atmospheric layer. Recently a model has been developed that yields similar estimates of cloud cover, without using aircraft observations. The model uses only RUSSWO statistics on the total sky cover and ceiling heights [Gringorten, 1982]. Figure 16-30 illustrates the out-
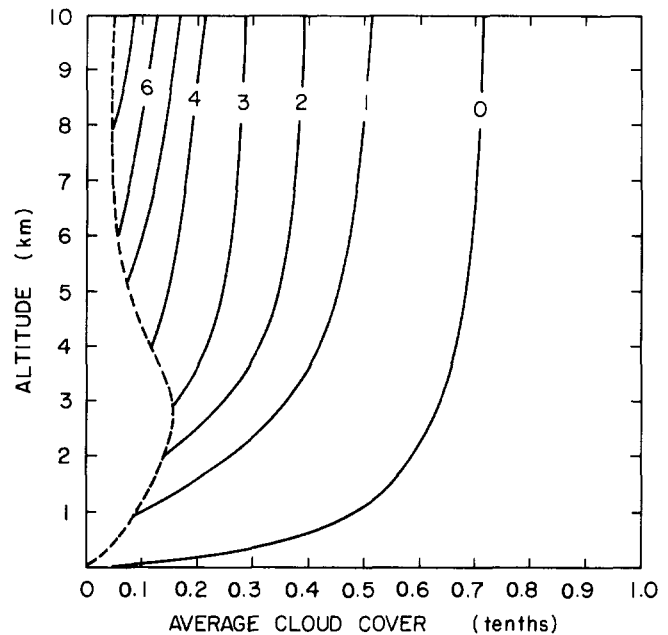
Figure 16-30. Average cloud cover by layers, December, 1200–1400 LST, Grissom AFB, Indiana.

put of the model in December, noontime for Grissom AFB, Indiana. The abscissa is for the cloud cover from 0 (clear) to 1.0 (overcast). The ordinate is for elevation above the ground, from 0 (surface) to 10 km aloft. The broken curve is drawn for the mean cloud cover at levels, and the solid curves are drawn for the mean cloud cover in layers. The broken curve shows, for example, mean cloud cover of 0.1 at 1 km, 0.14 at 2 km, 0.07 at 5 km. From each level the solid curve, when followed to a higher level, gives the average cloud cover in the layer between the two levels. For example, in the layer from 2 km to 4 km, the cloud cover averages 0.32, from 2 km to 8 km it averages 0.38, and so on.

In similar manner, the distribution of cloud cover in layers aloft can be reconstructed for any station that has RUSSWO or similar records. Grissom AFB, Indiana, was chosen for illustration because of its relatively high average sky cover. With a lower average, a station should have lower frequencies in most or all of its layers aloft.

16.3.3 Satellite and Radar Observations

16.3.3.1 Satellites. Weather satellite images are providing detailed information on the structure and distribution of clouds over large areas of the earth. Figure 16-31 illustrates a variety of cloud and fog formations over Europe and Northern Africa; the image was obtained from one of the satellites of the Defense Meteorological Satellite Program (DMSP). In addition to images in the visible portion of the spectrum as shown in Figure 16-31, corresponding images
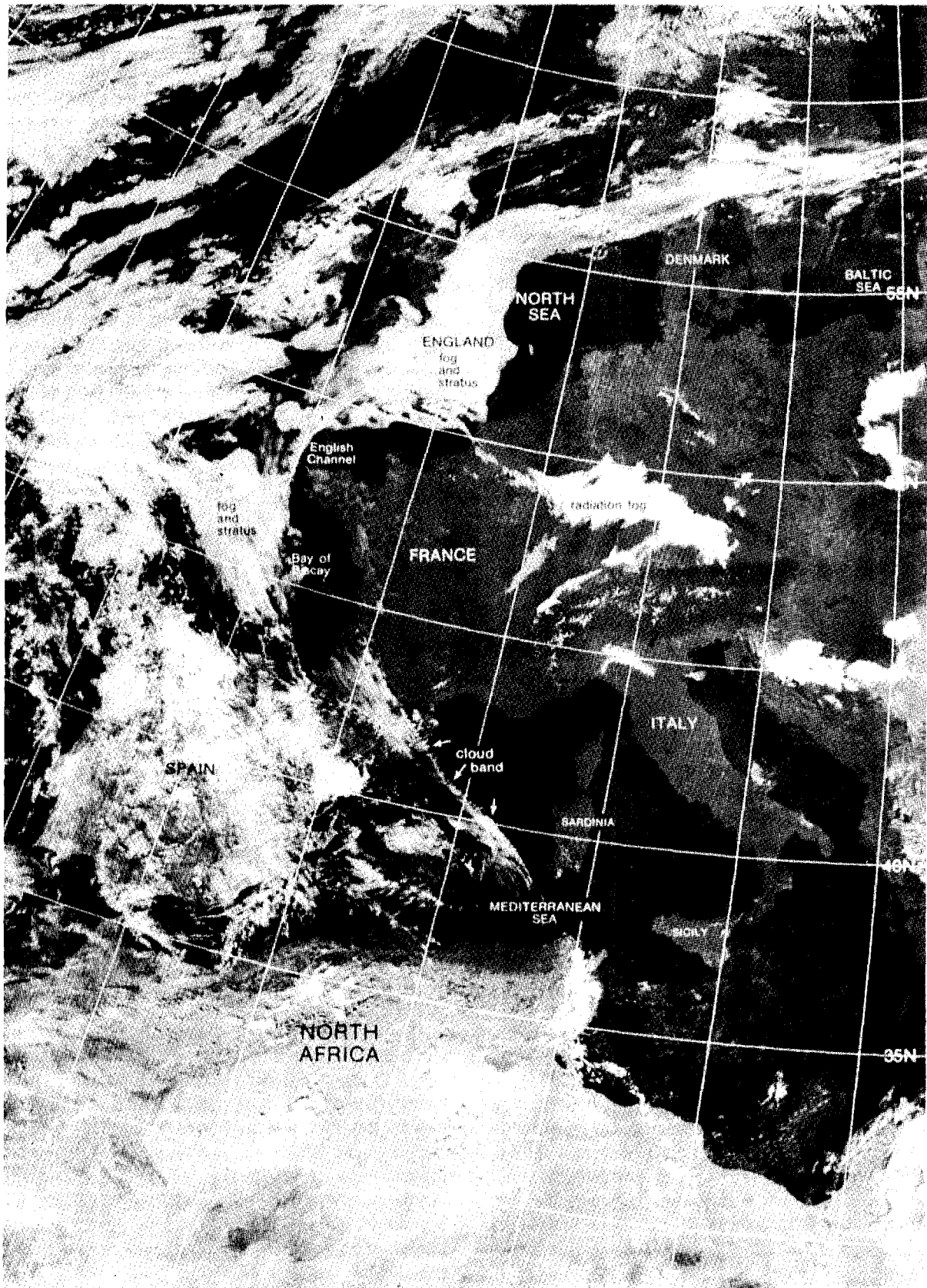
Figure 16-31.   DMSP LF low enchancement, 1015 GMT, 13 October 1978 [Fett et al., 1981].

in the thermal infrared are available. These simultaneous images or brightness fields can be used to deduce the height of the cloud tops. From the accumulation of such data, a regional and, eventually, a global cloud climatology will be developed.

16.3.3.2 Radar.

Because of the electromagnetic scattering characteristics of water drops and ice particles, detection of non-precipitating (less than 200 μm diameter), hydrometeors in clouds is effectively limited to the shorter radar wavelengths (less than a few cm). For example, radars operating at 0.86-cm wavelength have been used for operational cloud detection and continue to be used in research for deducing physical and dynamical characteristics of clouds prior to the development of precipitation. Precipitation-sized particles are readily detected by longer wavelength (3–10 cm) radars, as discussed in Section 16.2.5. Optical and infrared wavelength (0.5 to 15 μm) radars, or lidars, have also been used to observe clouds; theoretical comparisons of optical and microwave cloud detection capabilities have been made by Derr [1978].

Observations by the vertically pointing TPQ-11 radar were recorded by the Air Weather Service between 1964 and about 1975 at 43 locations around the world. The multiple-layer ceiling observations are archived at the National Climatic Center, Asheville, N.C. Two of these radars, acquired by the NOAA Wave Propagation Laboratory and the University of Washington, respectively, have been modified for improved reliability and sensitivity and are used in multi-sensor field programs. Early results were presented by Weiss et al. [1979], and by Pasqualucci and Miller [1981]. The Wave Propagation Laboratory subsequently built a transportable fully-scanning coherent 0.86-cm radar with a dual-polarization receiver which was first used in the spring of 1981. The dual polarization capability permits derivation of hydrometeor microphysical characteristics, while the coherent reception permits measurement of Doppler winds in clouds. There is increasing interest in the detection of clouds and aerosols by 0.3 cm radar [Lhermitte, 1981].

16.3.4 Clear and Cloud-Free Lines-of-Sight

To determine the utility of various communications, surveillance, and weapons systems, the probability of clear/cloud-free lines-of-sight (CLOS/CFLOS) must be known for the geographical areas and climatic regimes in which these systems must operate. (CLOS is defined as LOS not obscured by either haze or clouds). Since CLOS and CFLOS are neither directly observed nor measured on a routine basis, various methods have been developed to estimate their frequency of occurrence. Some of these methods are described in this section and examples of data, analyses, and results are provided on the frequency of occurrence of CLOS and CFLOS.

16.3.4.1 Aircraft Observations.

In a test program, Bertoni [1967] determined that realistic estimates of the probability of clear and cloud-free lines-of-sight could be derived from a large sampling of aircraft in-flight observations. This resulted in a major effort in which observations were made from aircraft, at various angles to the sky ($+30°$ and $+60°$), the horizon ($0°$), and the earth's surface ($-30°$ and $-60°$). Observations were acquired over most of the northern hemisphere during all months, but were limited to the daylight hours. (Nighttime observations tended to overestimate clear conditions).

Figure 16-32 is an example of the analyses shown in the resulting report [Bertoni, 1977a,b]. The large numbers in the figure are percent probabilities of CFLOS; the smaller numbers, in parentheses, indicate the total number of observations taken within each of the $10°$ latitude-longitude sectors. Figure 16-33 is similar to Figure 16-32 in that it shows probabilities of CLOS which are generally smaller than probabilities of CFLOS. This is illustrated more dramatically in Figure 16-34 in which frequencies of CLOS and CFLOS are compared for an area around Columbia, Mo, about 1000 km^2. Values for CLOS are reduced by some 20% to 30%, due mostly to haze. Figure 16-34 also confirms that the probabilities of CLOS and CFLOS depend on the angle of the line-of-sight as well as the percent of sky cover. CLOS and CFLOS probabilities increase as the lines-of-sight approach the vertical.

16.3.4.2 Surface Observations.

Whole-sky photographs at Columbia, Missouri and conventional National Weather Service observations of sky cover were used by Lund and Shanklin [1973] to develop a universal model for estimating probabilities of CFLOS through the entire atmosphere. Earlier CFLOS studies based on these same observations are described by Pochop and Shanklin [1966], Bundy [1969], Shanklin and Landwehr [1971], and Lund and Shanklin [1972].

Probabilities of CFLOS based on the Lund and Shanklin model can be estimated through the use of the following formula:

$$_\alpha\hat{P}_l = {}_\alpha C_s K_l, \qquad (16.26)$$

where $_\alpha\hat{P}_l$ is a column vector of α rows for each angle considered; $_\alpha C_s$ is a matrix for α rows and s columns, one row for each elevation angle, one column for each sky cover category; and $_s K_l$ is a column vector of s rows. The $\hat{P}$ values are estimates of probabilities of CFLOS through the atmosphere, the C values are probabilities of CFLOS at angles α given k tenths of sky cover and the K values are probabilities of each k tenths of sky cover. The $_\alpha C_s$ matrix is contained in Table 16-28.

Using the historical records for Columbia, Missouri as an example, the following probabilities of 0/10, 1/10, . . ., 9/10, 10/10 sky cover at Columbia are 0.187, 0.047, 0.047, 0.049, 0.037, 0.031, 0.045, 0.045, 0.055, 0.065, 0.392.

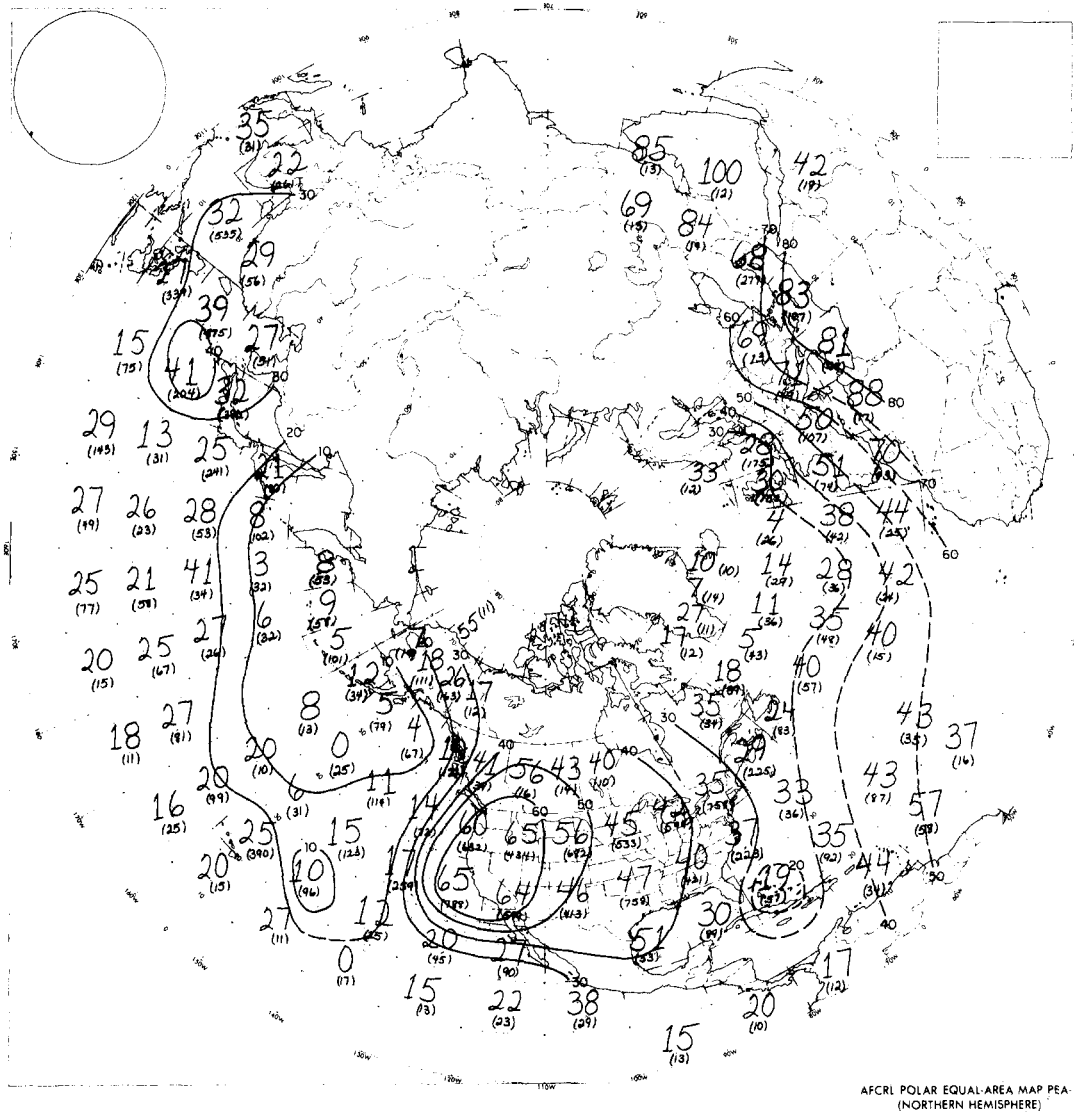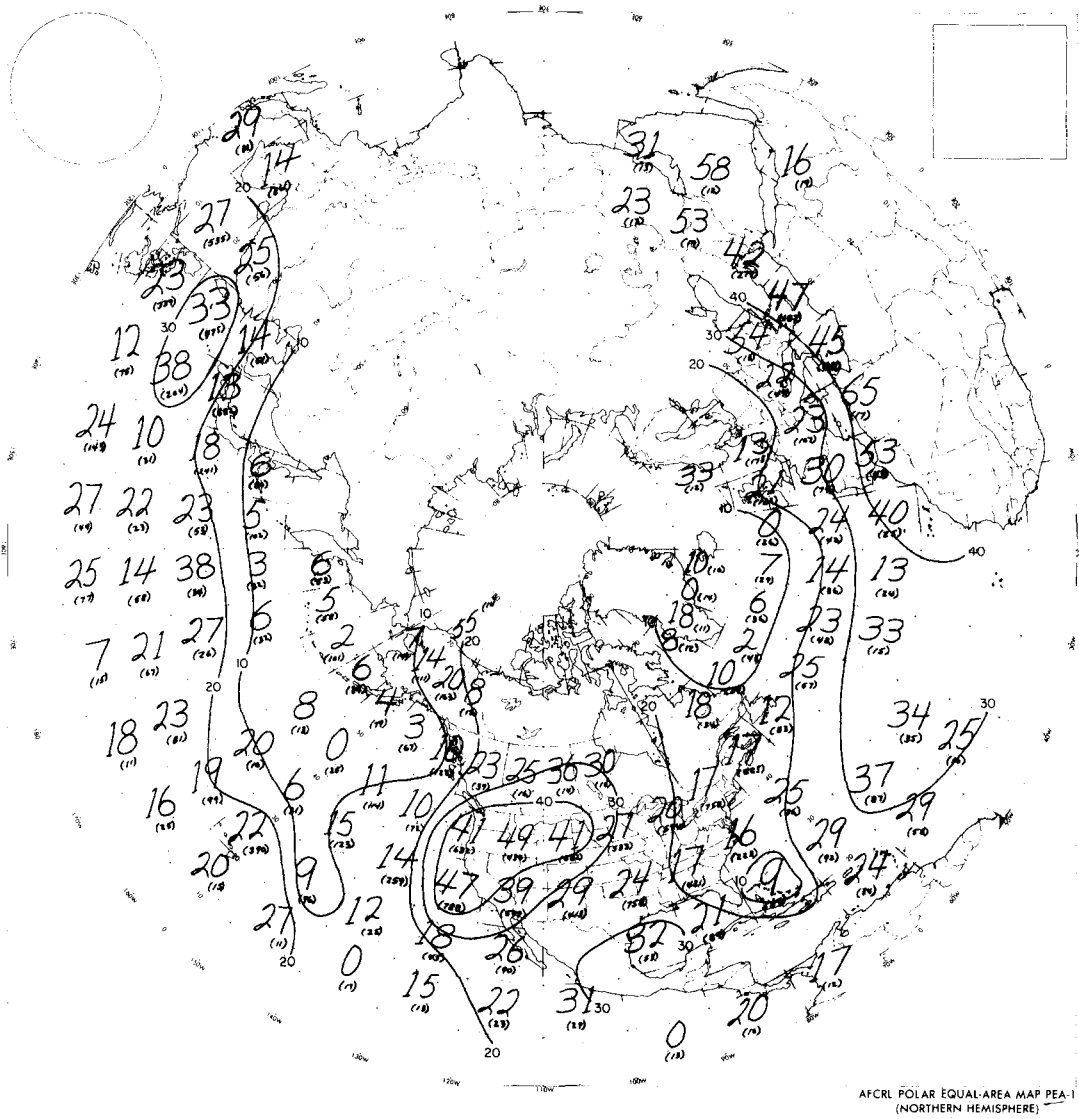AFCRL POLAR EQUAL-AREA MAP PEA-1
(NORTHERN HEMISPHERE)

Figure 16-32. Estimates of the probability of a cloud-free line-of-sight to the ground at 30° below the horizon (−30°) from altitudes between 7.6 and 10.6 km in summer.

Then the matrix multiplication indicated in Equation (16.26) yields

Elevation Angle (deg)	Probability
90	0.509
80	0.506
70	0.504
60	0.500
50	0.496
40	0.483
30	0.463
20	0.437
10	0.392

Consequently, there is an estimated 50.9% probability of a CFLOS at Columbia looking toward the zenith (90°), and a 50% and 46.3% probability of a CFLOS at 60° and 30° elevation angles, respectively. (See Section 16.3.4.3 for discussion of a correction to a suspected bias toward higher CFLOS probabilities produced by the Lund-Shanklin model.)

Using this model, atlases of CFLOS probabilities have been compiled for many parts of Europe, Asia and Africa, as well as for the U.S. and the USSR. (Lund et al., 1975, 1976, 1977, 1978, and 1979). A sample page from the atlas for the United States of America (Lund et al., 1977) is shown in Figure 16-35. This shows the probability of having a CFLOS in July at 1200 to 1400 LST at a 30° elevation angle. This atlas is based on at least a 15-yr period of record for the majority of U.S. stations shown by the dots in Figure 16-35.

Figure 16-33. Estimates of the probability of a clear line-of-sight to the ground at 30° below the horizon (− 30°) from altitudes between 7.6 and 10.6 km in summer.

Table 16-28. Probabilities of CFLOS as a function of elevation angle and observed Total Sky Cover [Lund and Shanklin, 1973].

Elevation Angle (deg)	Sky Cover (Tenths)										
	0	1	2	3	4	5	6	7	8	9	10
90	1.00	0.97	0.92	0.87	0.81	0.77	0.70	0.62	0.48	0.31	0.08
80	0.99	0.97	0.92	0.87	0.81	0.77	0.69	0.61	0.47	0.31	0.08
70	0.99	0.97	0.91	0.86	0.80	0.76	0.68	0.61	0.47	0.30	0.08
60	0.99	0.96	0.90	0.85	0.80	0.75	0.66	0.60	0.46	0.29	0.08
50	0.99	0.96	0.90	0.85	0.78	0.73	0.64	0.58	0.45	0.29	0.08
40	0.99	0.95	0.88	0.83	0.76	0.71	0.62	0.55	0.42	0.27	0.07
30	0.98	0.93	0.86	0.80	0.73	0.66	0.57	0.50	0.38	0.24	0.06
20	0.98	0.90	0.83	0.75	0.67	0.59	0.50	0.42	0.33	0.21	0.05
10	0.97	0.86	0.76	0.65	0.55	0.47	0.39	0.32	0.24	0.16	0.03
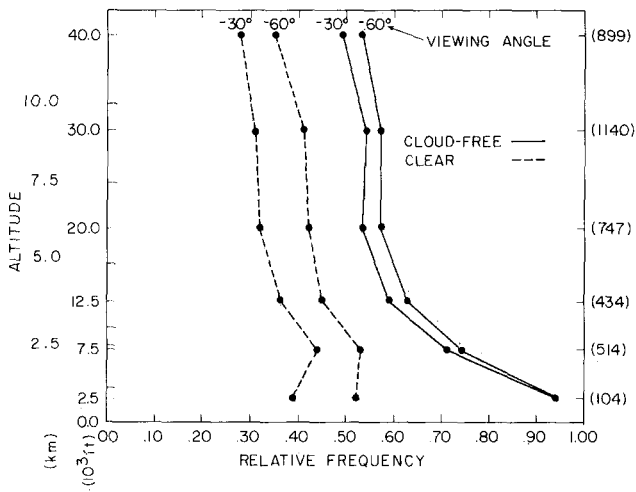
Figure 16-34. Relative frequencies of clear or cloud-free lines-of-sight observed in the area between 34° to 43°N and 88° to 97°W as a function of altitude. (The number of observations is shown in parentheses on the right hand margin.)

Rapp, Schutz, and Rodriques [1973] extended the Lund-Shanklin CFLOS model to include finding the probability of a CFLOS between the earth and any given altitude in the atmosphere. They accomplished this by using 3-h synoptic reports of clouds in addition to total sky cover.

16.3.4.3 Comparison of Estimates Between Aircraft and the CFLOS Model Based on Surface Observations.

CFLOS probabilities computed from sky-cover observations taken at 6 stations (Columbia, Mo., Atlanta, Ga., Fort Worth, Tx., North Platte, Neb., Alburquerque, N.M., and Ely, Nev.) have been compared with CFLOS probabilities based on observations taken from aircraft by Lund and Bertoni [1980].

CFLOS probabilities were computed at selected altitudes for each of the 6 stations, each midseason month, and each depression angle. The probabilities for the four midseason months were averaged and plotted, and were usually higher than those based on inflight observations. Figures 16-36 and 16-37 show the model and inflight CFLOS probabilities for
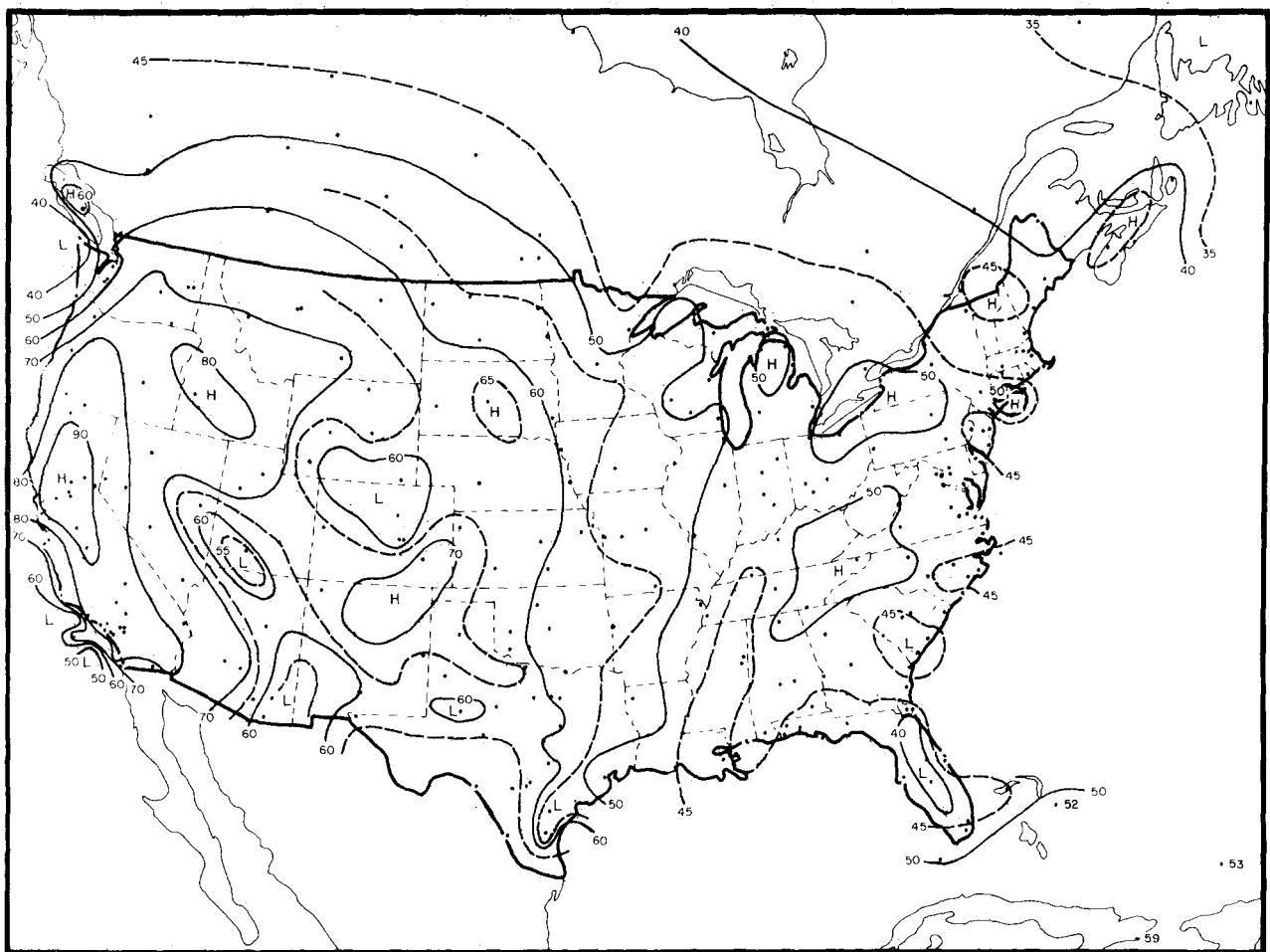
Figure 16-35. CFLOS probabilities for July, 1200–1400 LST, 30° elevation.
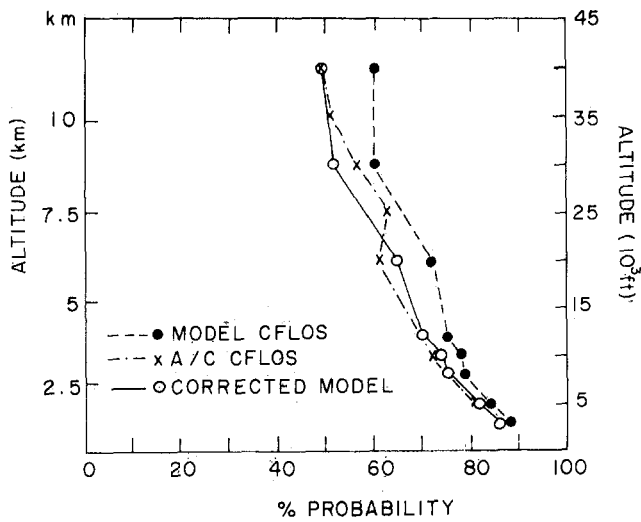
Figure 16-36. Six-station average probabilities of a cloud-free line-of-sight determined from aircraft observations (X's), from the CFLOS model (●'s), and from the model corrected for bias (○'s) at a depression angle of 30°.

depression angles 30° and 60°, respectively. The differences suggest that the Lund-Shanklin model CFLOS probabilities are biased toward higher values. This apparent bias can be essentially eliminated by a linear reduction of the model estimates as follows:

$$\hat{P}^1 = (0.99 - 0.0045a)\hat{P} \; ; \; 0 \leq a \leq 45, \quad (16.27)$$

where "a" is the altitude in kilometers and $\hat{P}$ is the model estimate. Figures 16-36 and 16-37 show the corrected CFLOS
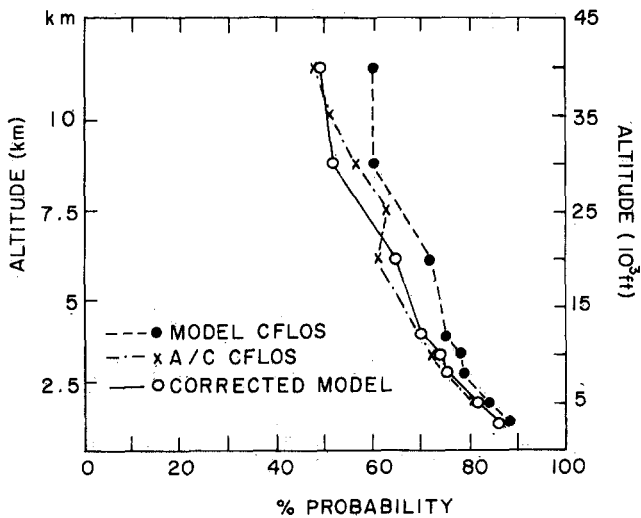
Figure 16-37. Six-station average probabilities of a cloud-free line-of-sight determined from aircraft observations (X's), from the CFLOS model (●'s), and from the model corrected for bias (○'s) at a depression angle of 60°.

estimates as well as the model and inflight CFLOS probabilities.

16.3.4.4 Cloud-Free Fields-of-View.

An instantaneous CFLOS is often not sufficient for acquiring and tracking a target, or for estimating the probability of detecting a target when there is an opportunity to search for favorable cloud conditions. Therefore, probability distributions of cloud-free areas of fields-of-view (FOV) are needed. Grantham et al. [1979] and Lund et al. [1980] completed studies for estimating the probability of cloud-free fields-of-view (CFFOV) between earth and an airborne or space platform. Using whole-sky photographs taken at Columbia, Mo., the average cloud-free fraction of each of 185 annular sectors [see Figure 16-38] was computed, plotted, and analyzed to determine how it varied with position on the photograph. Figure 16-38 depicts the average cloud-free fraction of each sector when 2/10 total cloudiness was observed. Clearly, the average cloud-free fraction decreases from the center of the picture, which corresponds to directly overhead, to low elevation angles of the edges of the picture. The maxima (highs) are not exactly centered at the zenith (the center of the picture) as one would expect. The failure of the isolines to be symmetric about the center of this figure is due in part to sampling variability. However, other studies of the photographs have suggested that sun angle or local effects, perhaps from the city of Columbia, may also contribute to the lack of symmetry.

Circular fields-of-view centered at a ground observers zenith were investigated. Figure 16-39 shows circles with
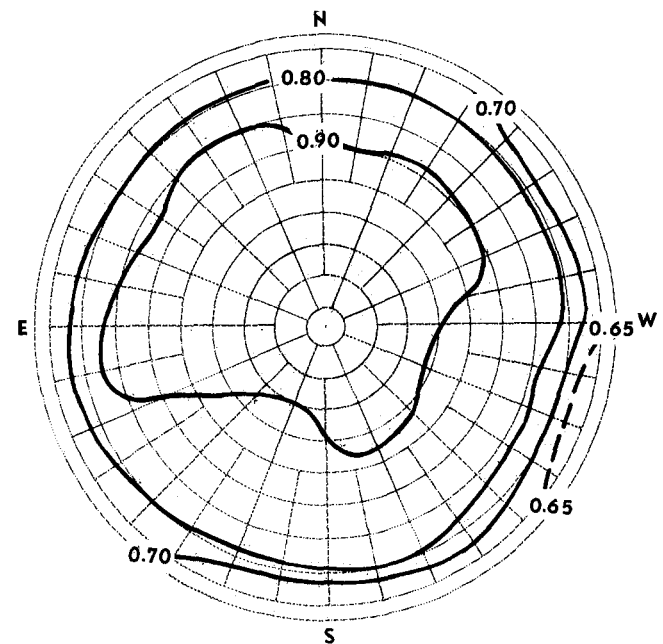

Figure 16-38. Average fraction of each annular sector that was cloud-free on the 131 photographs when 2/10 sky cloud cover was observed.
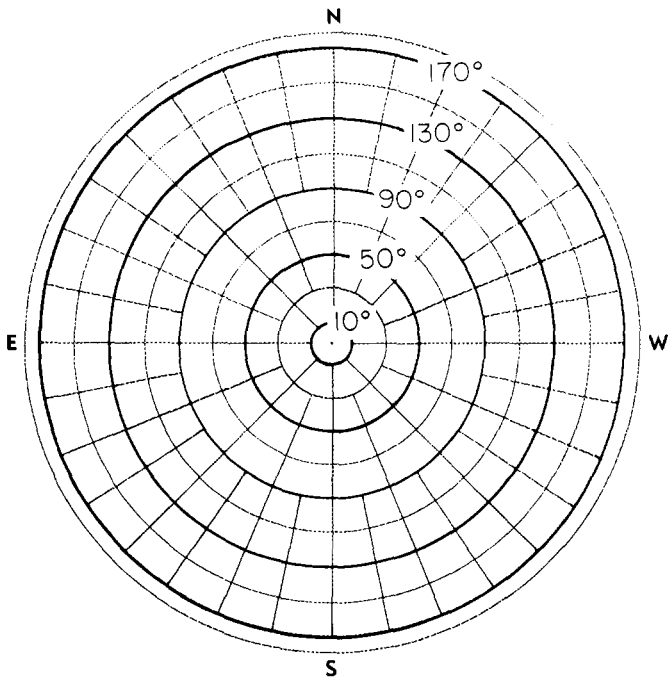
Figure 16-39. Circular fields-of-view with angular diameters of 10°, 50°, 90°, 130°, and 170° centered at the ground observer's zenith.

angular diameters, centered at the observer's zenith, of 10°, 50°, 90°, 130°, and 170°. Because the probability distributions are functions of the sky cover, they were stratified on that basis.

Figure 16-40 depicts cumulative frequency distributions of the fraction of the area that is cloud free in the 10° circle as a function of the observed sky cover. The points on the figure were obtained from the data and the curves were subjectively drawn through the points. This figure shows, for example, that if one wants to be 80% sure that at least 0.5 of the 10° FOV is cloud free, operation can be allowed only when 0/10, 1/10, 2/10, 3/10, or 4/10 sky cover is observed. If he relaxes his requirements to a 50% probability that at least 0.2 of the 10° FOV is cloud free, he can additionally operate when 5/10 or 6/10 sky cover is observed.

Figure 16-41 shows how the cloud-free fraction varies for five fields-of-view (10°, 50°, 90°, 130° and 170°) when the weather observer reports 5/10 sky cover. Let us assume that at least 0.2 of a FOV must be cloud free. The curve labeled 10° shows there is a 73% chance that at least 0.2 of the FOV is cloud free. The curve labeled 90° shows a 94% chance, and the curve labeled 170° shows a 100% chance that at least 0.2 of the 170° FOV will be clear when the observer reports 5/10 sky cover. If, however, the requirement is that at least 0.8 of the area must be cloud free, the probability will be near zero for the large 170° FOV and will increase to 44% for the small 10° FOV.

Lund et al. [1980] modified the Lund-Shanklin CFLOS model described in Section 16.3.4.2 to estimate climatic
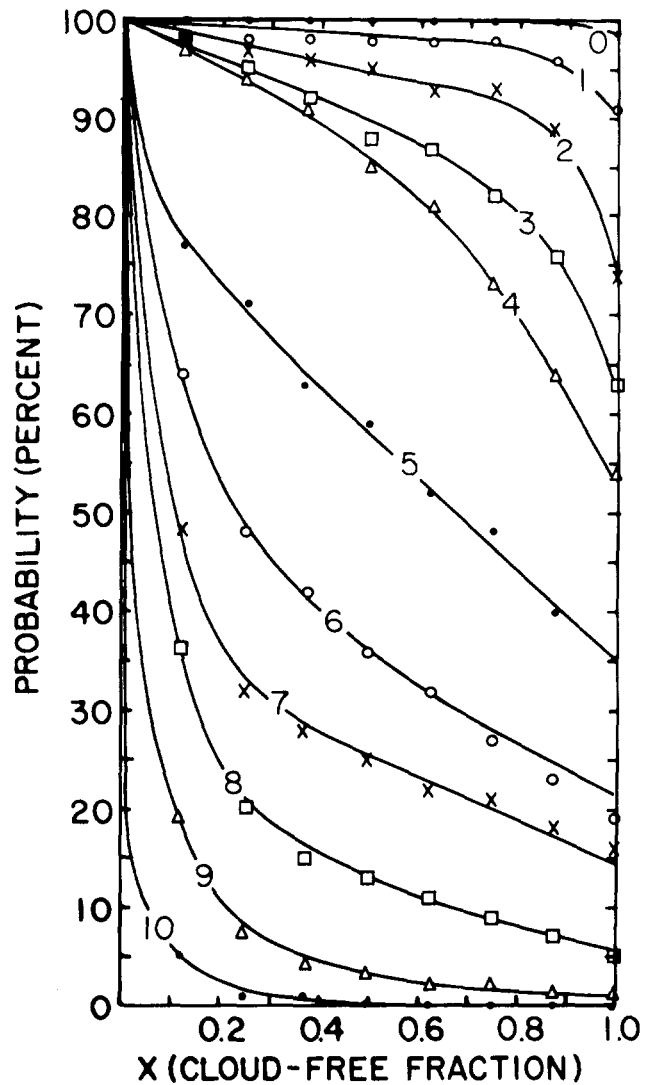
Figure 16-40. Probability that a 10° FOV at zenith will have a cloud-free fraction $\geq x$ (curves for each tenth of sky cover were subjectively drawn to the data points).

probabilities of CFFOV from climatic probabilities of the tenths of cloudiness. Figure 16-42 shows a comparison of the probability of a CFLOS as a function of elevation angle when two-tenths sky cover is reported, with corresponding CFFOV probabilities when the FOV is 10° and 20°. The figure shows good agreement between CFLOS probabilities and FOV probabilities for cloud-free fractions ≥ 0.5 and ≥ 0.75. However, there is only a 61% chance that a 10° FOV centered at a 30° elevation angle will be totally cloud free, and only a 48% chance for a 20° FOV to be totally cloud free. These differences between the CFLOS and CFFOV model probabilities are larger than expected. Therefore, users of the CFFOV model and the CFLOS model should understand that the models yield probability estimates which are believed to be good first approximations. Better approximations await higher quality whole-sky photographs or more precise observing techniques.
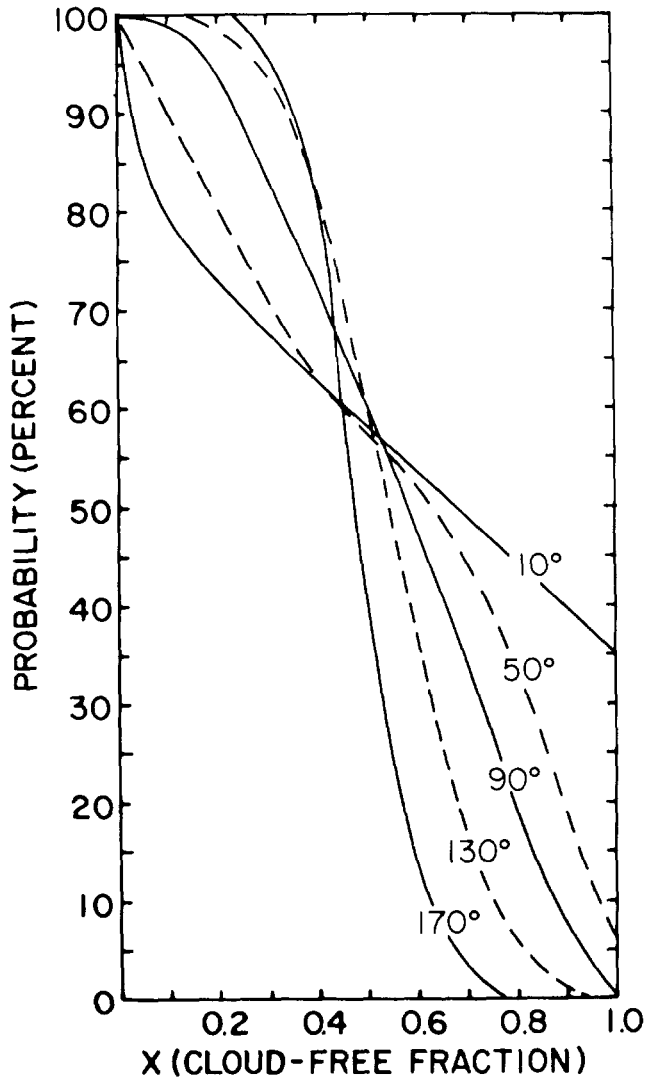
Figure 16-41. The probability that a 10°, 50°, 90°, 130°, and 170° FOV at zenith will have a cloud-free fraction ≥x when the weather observer reports 5/10 sky cover.

16.3.4.5 Joint Probabilities of CFLOS. Lund [1973] extended the Lund-Shanklin [1973] CFLOS model described in Section 16.3.4.2 to address the problem of estimating joint probabilities of cloud-free lines-of-sight from more than one observing sight. This model requires a climatic record of sky cover observations taken simultaneously from all sites.

Table 16-29 gives estimated CFLOS probabilities for Minot, N.D., $P(C_M)$; three-way joint probabilities of CFLOS for Grand Forks, Minot, and Fargo, $P(C_G \ C_M \ C_F)$; and, three-way joint probability for none of the three sites, $P(\overline{C}_G \ \overline{C}_M \ \overline{C}_F)$. The probabilities apply to August, the month when the highest CFLOS probabilities occur, and the elevation angle is 40°. Table 16-30 is the same as Table 16-29 except that probabilities apply to November, the month when the lowest CFLOS probabilities occur.
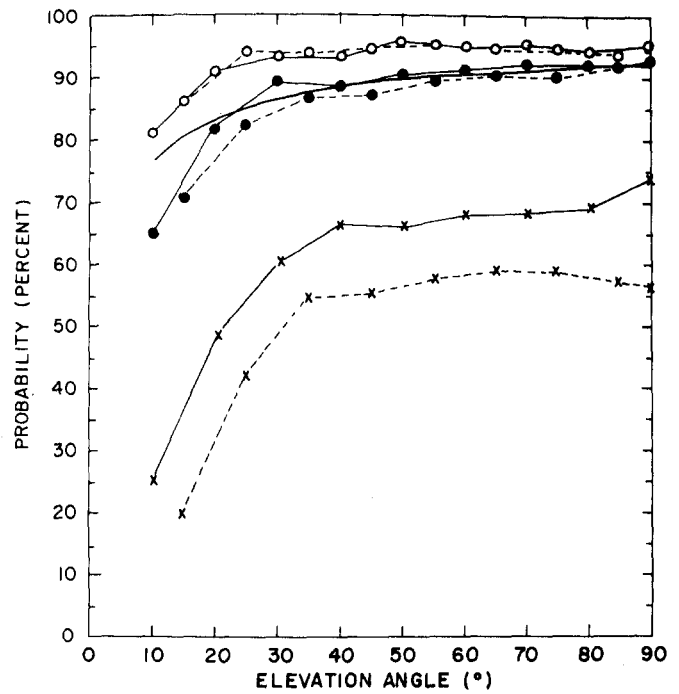
Figure 16-42. The probability of a CFLOS as a function of elevation angle when 2/10 sky cover is reported (heavy curve), and corresponding CFFOV probabilities when the FOV is 10° (solid lines) and 20° (dashed lines.).

16.3.5 Water Content of Clouds

Moisture in clouds can exist as a vapor, liquid, or solid. Some water vapor is always present in the atmosphere. The amount of water vapor a parcel of air can hold is a function of the temperature [Haurwitz, 1941]. Under conditions where the atmosphere becomes saturated the water vapor condenses and forms clouds.

Knowledge of the amounts of liquid water and ice contained within clouds is important to aviation due to its direct and indirect effects. The quantity "liquid water content" is the concentration, expressed in mass per unit volume, precipitation. Although many methods of determining liquid water content have been used, none are completely satisfactory.

Table 16-29. Estimated 3-way joint probabilities of CFLOS at 40° elevation angle for August at Minot $P(C_M)$; Grand Forks, Minot, and Fargo, $P(C_G \ C_M \ C_F)$; none of the three sites, $P(\overline{C}_G \ \overline{C}_M \ \overline{C}_F)$.

	Hour							
	0	3	6	9	12	15	18	21
$P(C_M)$	0.73	0.74	0.65	0.62	0.59	0.58	0.60	0.67
$P(C_G \ C_M \ C_F)$	0.48	0.48	0.37	0.35	0.34	0.31	0.35	0.41
$P(\overline{C}_G \ \overline{C}_M \ \overline{C}_F)$	0.07	0.08	0.12	0.13	0.15	0.14	0.13	0.10

Table 16-30. Same as Table 16-29 except the probabilities apply to November, the month when the lowest CFLOS probabilities occur.

	Hour							
	0	3	6	9	12	15	18	21
$P(C_M)$	0.50	0.49	0.50	0.36	0.38	0.39	0.40	0.49
$P(C_G\ C_M\ C_F)$	0.23	0.22	0.20	0.14	0.13	0.14	0.17	0.23
$P(\overline{C}_M\ \overline{C}_M\ \overline{C}_F)$	0.27	0.28	0.28	0.40	0.38	0.37	0.34	0.29

16.3.5.1 Liquid Water Content in Clouds.

The actual amount of liquid water from droplets or ice crystals in a cloud will vary, depending on the type, altitude, and temperature of the cloud. Clouds formed by strong vertical motion will generally contain large amounts of liquid water. Lamb et al. [1976] measured as many as 1.5 g/m³ in synoptic-scale winter clouds that contained convective elements. Generally, clouds of this type range in amounts that are illustrated in Figure 16-25. Aufm Kampe and Weickmann [1957] suggest 10.0 g/m³ as the maximum value of liquid water content in cumulonimbus clouds. Higher values have been reported. The range of values and probability of occurrence are discussed in detail in Section 16.2.5.4.

In large-scale storm systems, liquid water content in most of the clouds is in the range 0.1 g/m³. The highest values of liquid water content (see Figure 16-25) occur near the freezing level (or melting layer).

The values quoted in the preceeding paragraphs have been computed from particle-size distributions and assumptions relating crystal size and equivalent melted diameter. They should be considered as best estimates. Increased accuracy will be possible only when a reliable method of directly measuring water content is developed.

16.3.5.2 Measuring Liquid Water Content.

Three methods of measuring liquid water content have been tried: direct measurement, computation from particle distributions, and attenuation of radar or lidar signals.

Although several possible instruments for direct measurement have been devised, only one, the Johnson-Williams (JW) indicator has been used on an operational basis. This instrument operates on the principle that the change in resistance of a heated wire as it evaporates impacting particles is proportional to the liquid water content. The probe is sensitive only to liquid droplets having diameters of ≤30 μm.

The most frequently used method of determining liquid water content is by integration of the particle-size spectra obtained by use of an optical array spectrometer. This procedure is straightforward when particles are liquid. However, when particles are ice crystals, assumptions concerning the relation of crystal size and their equivalent melted diameter are necessary. The AFGL Cirrus study [Cohen,

1981a] and Large Scale Cloud Systems study [Cohen, 1981b] used this method. Knollenberg [1972] notes that this method compared favorably to results given by direct measurement.

During recent years, attempts to relate liquid water content to the intensity of radar returns have been made. Stickel and Seliga [1981] describe one such attempt. At this time, however, radar is not able to give the definition that either direct measurements or computation from particle distributions can provide.

16.3.5.3 Supercooled Clouds and Aircraft Icing.

The principal meteorological parameters associated with aircraft icing are the ambient temperature, the cloud liquid water content, and the drop size distribution. The extent to which ice forms on an aircraft (that is, icing intensity) and whether or not rime or glaze ice is formed depend additionally on the aerodynamic shape of the airplane structures, its true air speed, and the length of time the aircraft is in the icing environment.

The source of most meteorological information collected on icing parameters, including the data presented here, are from stratiform clouds (stratus, stratocumulus, and altostratus). Ninety percent of these clouds are 1 km thick [Figure 16-43]. Stratiform clouds are of principal concern with respect to icing since convective clouds (cumulus, cumulocongestus, and cumulonimbus) are generally avoided by aircraft for other reasons. Cumulus clouds are also relatively limited in horizontal dimension and duration. However, conditions in cumuliform clouds can result in severe icing
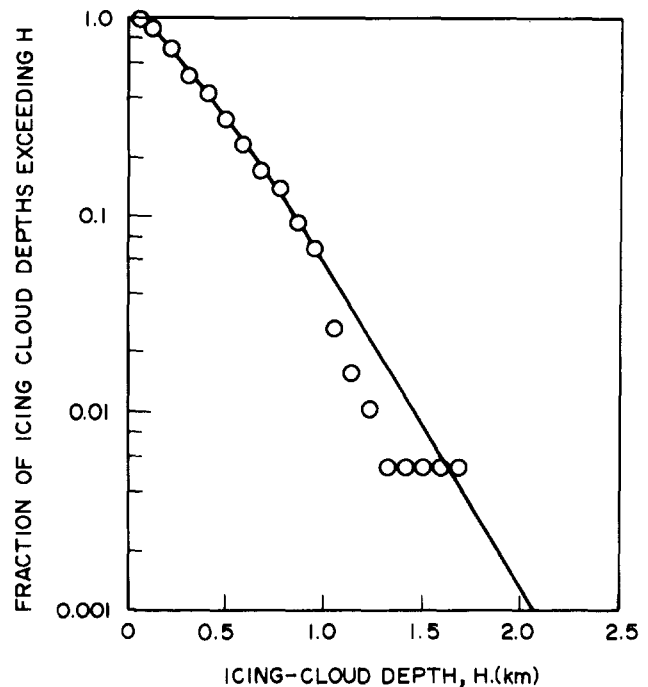

Figure 16-43. Cumulative frequency distribution of depth of icing-cloud layer [after Perkins, 1978].

of aircraft since supercooled water in excess of 2.0 g/m³ [Mason, 1971] have been observed as well as drop sizes occurring over the complete range of the size spectrum. Additional information concerning specific cloud types, associated synoptic conditions, and their relation to icing is given by Lewis [1951] and the Air Weather Service [AWS, 1980].

Clouds containing supercooled droplets (that is, water in the liquid state at temperatures below freezing) can exist in the atmosphere to temperatures as low as 233 K. However, the probability that supercooled droplets will remain unfrozen below the temperature range of 258 K to 253 K decreases rapidly since the number concentration of active freezing nuclei becomes significant at these temperatures. Perkins [1978] observed that approximately 90% of the clouds sampled that contained supercooled water were at temperatures warmer than 253 K. The likelihood of encountering clouds containing supercooled droplets as a function of temperature is shown in Figure 16-44.

The liquid water content (LWC) in wintertime stratiform clouds is a highly variable parameter. This is due principally to the horizontal variations in cloud structure. LWC averaged over long path lengths (>25km) usually do not exceed 0.3 g/m³. Altostratus and altocumulus clouds forming at higher altitudes have proportionately lower LWC amounts due to the temperature dependency of saturation vapor pressure of water. In individual stratocumulus cloud elements,
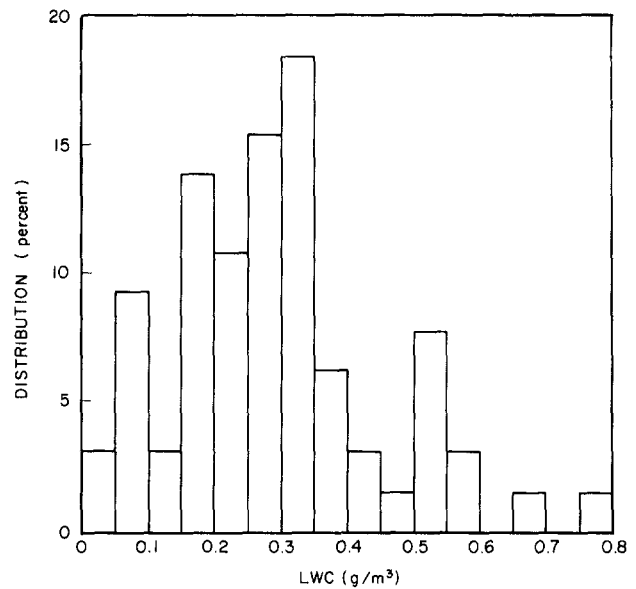

Figure 16-45. Distribution of LWC from 65 sample cases [Glass and Grantham, 1981].

with horizontal dimensions of 0.5 km to 1.0 km, peak LWC values of 1.3 g/m³ have been observed, although values not exceeding 0.8 g/m³ are more typical. The distribution (in percent) of supercooled water content amounts is shown in Figure 16-45. These data are based on sample measurements [Glass and Grantham, 1981] from a day considered representative of clouds during winter icing conditions. The distribution of median volume diameters for these data is shown in Figure 16-46.
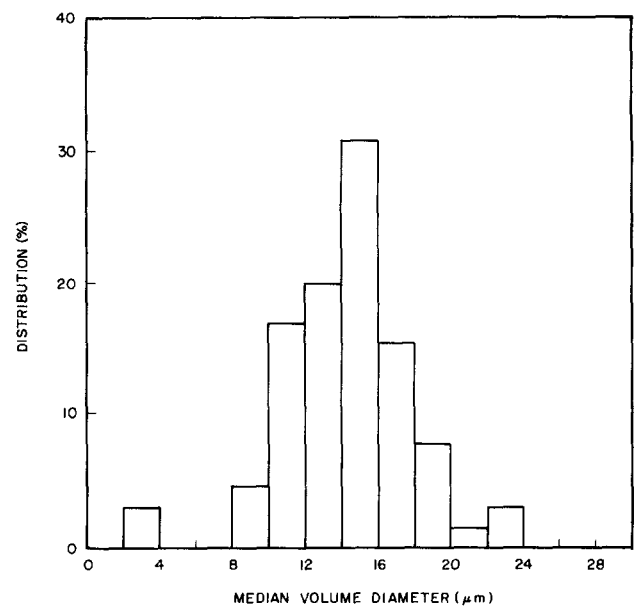

Figure 16-44. Cumulative frequency distribution of temperature of icing-clouds [after Perkins, 1978].

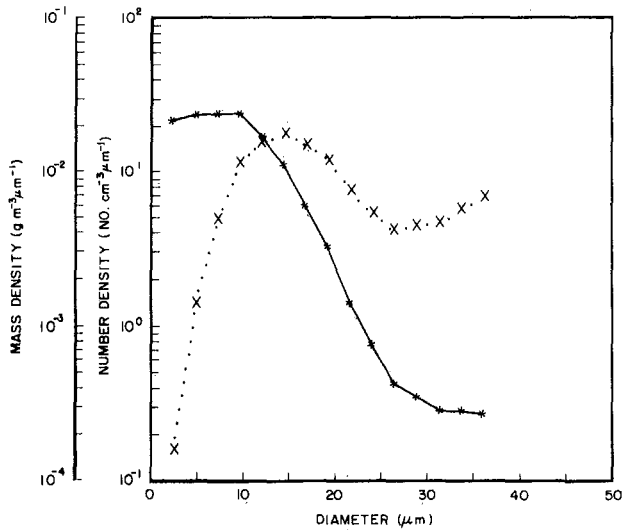Figure 16-46. Distribution of average median volume diameter during each of 65 sample cases [Glass and Grantham, 1981].

Figure 16-47. Number (*) and Mass (..x..) distribution with size for data sets with ≥0.2 g/m³ liquid water.

Distributions of the number and mass density of droplets with respect to size obtained from the same data set are shown in Figures 16-47 and 16-48. Both figures are based on long-duration data sets. Figure 16-47 is drawn from data sets where the average LWC was equal to or greater than 0.2 g/m³, whereas Figure 16-48 is based on data sets from which LWC values did not exceed 0.1 g/m³. Some parameters obtained from these distributions are shown in Table 16-31. Past observations [Perkins, 1978] of droplet-size distribution in supercooled stratiform clouds indicated that values can range up to 50 μm. More recent observations have suggested that large supercooled drops (approaching 300
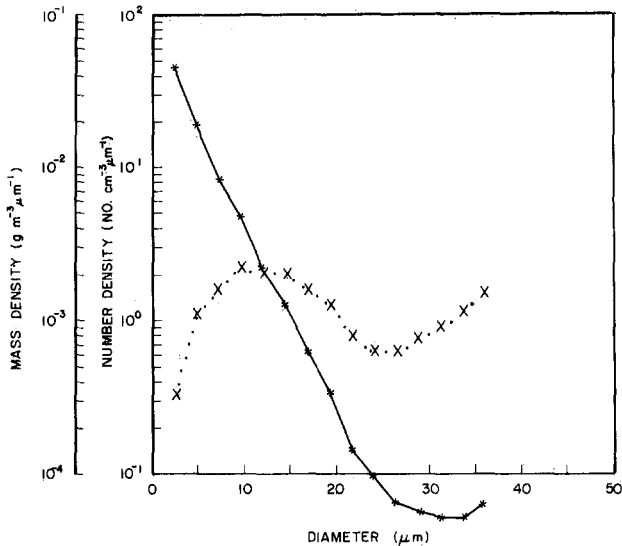
Table 16-31. Characteristiccs of size and mass spectra for the indicated figures.

	Figure 16-47	Figure 16-48
LWC(g/m³)	0.27	0.04
Number density (cm⁻³)	321	192
Mean Vol Diameter (μm)	12	8
Median Vol Diameter (μm)	16	14

μm in diameter) can be found in these clouds. Their number density, however, is much less than 1.0/cm³.

Techniques developed by the Air Weather Service [AWS,1980] for forecasting icing conditions are based on radiosonde observations of temperature and the dew-point spread (difference between temperature and dew point). These parameters are used since formation and maintenance of clouds containing supercooled droplet spectra require a saturated or near-saturated environment. This report quotes studies indicating that when only dew-point spread is considered, there is an 80% probability of icing when the spread is ≤3 K, and 84% probability of no icing when the spread exceeds 3 K. A northern hemisphere climatology of icing probabilities, utilizing the Air Weather Service analysis method [AWS,1980] and applied to 380 northern hemisphere radiosonde stations, has been published by the Air Weather Service [Heath and Cantrell, 1972].

16.3.6 Clouds above 6 Km

Almost all clouds found above 6 km are cirriform clouds composed of ice crystals. Cirriform clouds have been observed at altitudes in excess of 15 km.

16.3.6.1 Observations of Cirrus Clouds. In 1896–97, various observatories made double-theodolite measurements of cirriform clouds. Table 16-32a lists the average heights of the cloud bases in different seasons and at different latitudes. Table 16-32b shows the maximum base heights of cirrus and cirrostratus clouds at these locations [Suring, 1941; Appleman, 1961]. This table indicates that the bases of cirriform clouds are higher at lower latitudes and during the summer, and that the bases of cirrus clouds tend to be higher than those of cirrostratus layers. These observations were confirmed by aircraft flights in the 1950s. The flights made at that time also provided data on the heights of tops, thickness, and frequency of occurrence of cirriform clouds.

Cirriform clouds in the temperate zone are more common in cold weather and at high latitudes. Both bases and tops vary in height, being higher in summer and lower in winter. Tops of cirriform clouds are closely associated with the tropopause. Generally, the tops occur 1.2 to 1.5 km below the tropopause. The thickness of high clouds averages 2.1 to 2.2 km and shows little or no variation with season.

Figure 16-48. Number (*) and mass (..x..) distribution with size for data sets with <0.1 g/m³ liquid water.

Table 16-32a. Mean heights of cirrus bases for international cloud year 1896–1897.

Latitude	Place	Northern summer (km)	Northern winter (km)
78°N	Cape Thordsen	7.3	—
70°N	Bossekop (Sweden)	7.5	—
60°N	Pavlovsk plus Uppsala	7.9	7.1
51°N	Potsdam plus Trappes (average)	8.7	7.7
40°N	Blue Hill plus Washington (average)	10.2	9.1
35°N	Mera (Japan)	11.0	9.1
14°N	Manila	12.0	11.1
7°S	Batavia	11.0	—
35°S	Melbourne	8.5	9.6

Table 16-32b. Maximum heights of cirrus bases for international cloud year 1896–1897.

Latitude	Place	Cirrus (km)	Cirrostratus (km)
78°N	Cape Thordsen	8.6	—
70°N	Bossekop (Sweden)	11.8	10.4
60°N	Pavlovsk plus Uppsala	11.7	10.1
51°N	Potsdam plus Trappes (average)	12.7	11.9
40°N	Blue Hill plus Washington (average)	15.0	13.6
35°N	Mera (Japan)	16.8	15.5
14°N	Manila	20.4	17.1
7°S	Batavia	18.6	14.2
35°S	Melbourne	—	—

In the 1970s, both particle density and liquid water content of high-altitude clouds were investigated in airborne studies of the microphysics of clouds. Aircraft studies of cirriform clouds have been reported by Heymsfield [1975], Ryan et al. [1972], and McTaggert-Cowan et al. [1970]. In more recent years, AFGL has published a series of reports on this subject [Cohen, 1981a,b].

AFGL research flights have shown that cirrus cloud particles are almost always smaller than 1200 μm in diameter.

Heymsfield did find occasional particles as large as 1900 μm, but these were very rare, and generally their number density was less than 1/cm³. Most cirrus particles are smaller than 600 μm. Varley et al. [1980] found some larger particles in the vicinity of a surface storm, but this was an exceptional case.

Although comparison of the work of different investigators is risky due to differences in instrumentation and presentation, an analysis of the results of three studies are

Table 16-33. Water content (melted ice) and particle density observations in cirriform clouds.

Observer	Date	Cloud Type	Altitude (km)	Water Content (Melted Ice) (gm/m³)	Maximum Particle Density (Number/cm³)
Heymsfield	9 Jul 70	Cirrus	7	0.30	Not reported
Heymsfield	4 Apr 72	Cirrostratus	8	0.03	0.20
Ryan	12 Jun 70	Cirrus	9	Not Reported	3.60
McTaggart-Cowan	18 Jun 69	Cirrus	12	Not Reported	0.53
AFGL	28 Jan 79	Heavy Cirrostratus	8	0.23	0.13
AFGL	2 Feb 79	Cirrostratus	9	0.03	0.11
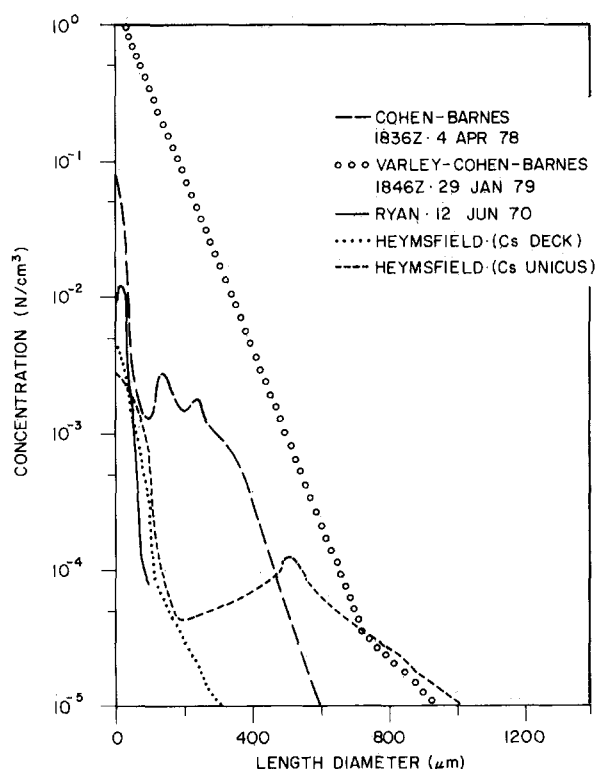
Figure 16-49. Cirrus particle concentrations seen by different observers.

Figure 16-50. Particle size distribution of small-particle subvisible cirrus.

shown in Figure 16-49. This figure gives an idea of different size distributions and is not intended to compare the results of the different studies.

Typical water content (melted ice) and particle densities reported by different observers are shown in Table 16-33.

16.3.6.2 Subvisible Cirrus. Cirrus-like ice particles occurring in apparently cloudless air are called subvisible cirrus. Thin cirrus clouds that are only visible from certain directions or at certain times may also be called subvisible cirrus. Most subvisible cirrus is found in the 3 or 4 km immediately below the tropopause. The maximum occurrence of cirrus, both visible and subvisible, is usually 1 to 2 km below the tropopause. Recent observations suggest that subvisible cirrus is present more than 75% of the time; one rarely finds cloudless areas in the cirrus region in which there are fewer than one particle greater than 2 μm in diameter per cm³.

There are two kinds of subvisible cirrus. The most common consists of small particles with diameters of less than 50 μm, with most particles being less than 20 μm in diameter (see Figure 16-50). Barnes [1980] describes the second type of subvisible cirrus as consisting of isolated ice crystals with diameters of 100 μm to 3000 μm. These particles may occur with the first type (see Figure 16-51), or they may be found in layers devoid of the smaller particles, having fallen from higher-level clouds (often cirrus unicus), where they were generated. In Arctic regions, these crystals
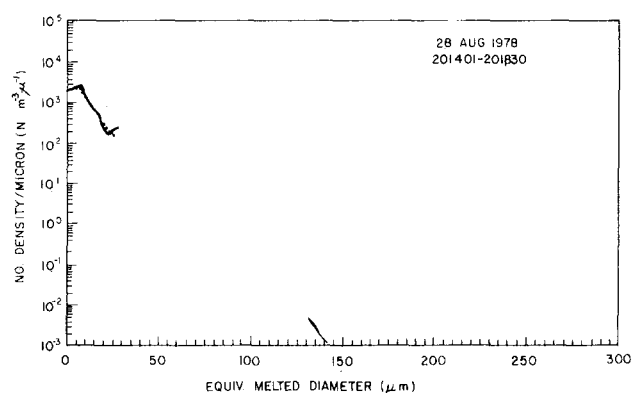
can fall to the ground [Kikuchi and Hogan, 1979] as "diamond dust" snowfalls. Cirrus particles can survive falls in excess of 2 km in subsaturated air [Hall and Prupacher, 1976].

Hall [1964] implies that subvisible cirrus can reduce the lift on laminar flow wings. Barnes [1978] notes that cirrus particles cause erosion of hypersonic vehicles, such as reentry vehicles, and that the presence of unreported thin and subvisible cirrus reduces the efficiency of solar collectors and attenuates energy in laser beams [Barnes, 1982].

16.3.6.3 Clouds Above the Tropopause. While almost all of the water and ice clouds in the atmosphere are in the troposhere, there are some occasions in which clouds penetrate into the stratosphere. This is generally the result of strong convective activity in which severe thunderstorms, caused by unstable conditions and high moisture content, have enough energy to break through the tropopause (Figure 16-52). In this vein, the frequency and percent occurrence of radar precipitation echoes have above 15 km have been estimated [Kantor and Grantham, 1968]. This climatology of radar precipitation echoes also provides information on the month of occurrence and estimated vertical extent of
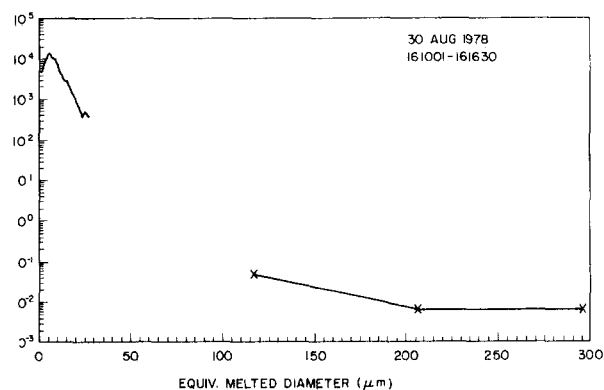

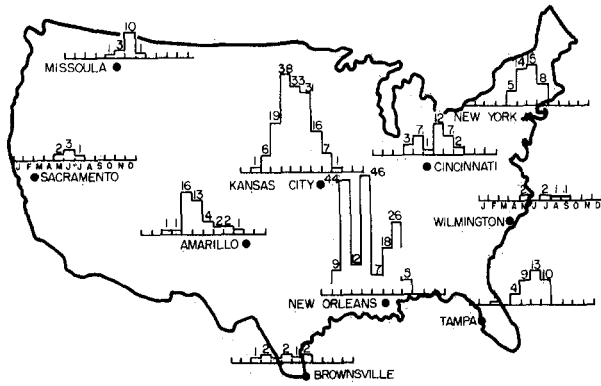Figure 16-51. Particle size distribution showing both types of subvisible cirrus.

Figure 16-52. Average monthly tropopause penetrations by thunderstorms, 1961–1964 [Long et al., 1965].

cumulonimbus clouds over the United States. As a further example, Table 16-34 indicates that cirrus tops can build well beyond the tropopause. The cirrus produced by thunderstorms can often extend about 185 km downwind of the cell that produced it. Thus, stratospheric clouds, while not common, do exist and can be expected in and near regions of strong convective activity.

The size and shape of high altitude convective clouds have been estimated [Long et al., 1965; Roach, 1967]. For thunderstorms that have penetrated the tropopause in the midwestern United States, the shape of the cloud is a cone with a diameter-to-height ratio of roughly five to one for the portion of the cloud above the tropopause. However, much of the cirrus blowoff (shield) that is observed from the ground remains below the tropopause. Mean diameter of high altitude convective cells, including the associated anvil, has been estimated at 32 to 50 km.

16.3.6.4 Tropopause Height. Because there are seasonal, latitudinal, and daily variations in the height of the tropopause, both the latitude and season of the year must be considered in studying the height of the tropopause. Table 16-35 gives mean seasonal heights of the tropopause in the Northern Hemisphere; however, mean seasonal heights may be several kilometers higher than indicated in Table 16-35 on the east side of semistationary lows such as the Icelandic and Aleutian lows during the winter and spring months.

In middle latitudes the day-to-day variations in the height of the tropopause exceeds the seasonal variations; large variations in height occur as a result of horizontal oscillations in the tropopause. The arctic tropopause from the north is brought southward in the rear, and the tropical tropopause from the south is projected northward in advance of well-developed migratory cyclones. Although data are not sufficient to establish exact limits, available data indicate that in middle latitudes (40° to 60°N) the tropopause can fluctuate between about 6 and 15 km. North of 60° and south of 30° latitude, the range is much smaller, the order of 900 to 1800 m around the seasonal mean heights.

Table 16-34. Distribution of cirrus tops relative to the tropopause.

Distance From Tropopause (m)	Frequency of Occurrence (%)
British Isles	
>1200 above	10
1200 to 0 above	10
0 to 1200 below	50
1200 to 2400 below	16
>2400 below	14
Canada	
>1500 above	1
1500 to 0 above	12
0 to 1500 below	52
1500 to 3000 below	23
<3000 below	12

16.4. FOG

Fog, as well as clouds, affect the propagation of electromagnetic radiation through the atmosphere, especially in the frequency spectrum >30 GHz (<1 cm wavelength). The absorption and scattering of electromagnetic radiation by water spheres and fogs have been extensively studied. Deirmendjian [1964], Herman [1962], and Platt [1970] have discussed extinction and scattering by water droplets in the visible, infrared and submillimeter regions of the spectrum, respectively. Gunn and East [1954] have discussed absorption and scattering of microwaves by clouds and rain. The amounts of absorption and scattering are functions of the microphysical structure of the fog.

16.4.1 Microphysical Structure

16.4.1.1 Condensation Nuclei. The atmosphere contains a large concentration of dry aerosol particles ranging in size from about $10^{-3}\mu m$ to $10\mu m$ radius. Mason [1971] divides the spectrum of particles into three parts: (1) Aitken

Table 16-35. Mean seasonal heights of the tropopause.

Latitude	Altitude			
	Dec–Feb (m)	Mar–May (m)	Jun–Aug (m)	Sep–Nov (m)
60° to 80°N	8 400	8 800	9 400	9 200
50° to 60°N	9 200	10 000	11 300	10 000
40° to 50°N	10 000	11 000	12 700	11 800
30° to 40°N	14 000	13 800	14 000	14 200
10° to 30°N	17 000	16 800	15 700	16 300

nuclei (r < 0.1μm), (2) large nuclei (0.1 < r< 1.0μm), and (3) giant nuclei (r > 1.0μm). All of these particles can act as condensation nuclei provided the supersaturation is large enough (300%). However, in the real atmosphere there is a sufficient number of hygroscopic particles so that condensation occurs at supersaturations of less than 0.1%. These hygroscopic particles are either large or giant nuclei. In other words, the Aitken nuclei are not an important factor in the formation of fog even though concentrations of Aitken nuclei up to $10^6/cm^3$ are possible in urban industrial areas. Concentrations of large and giant nuclei are considerably less, averaging about $10^2/cm^3$, with a maximum concentration of about $10^3/cm^3$.

Several workers have derived analytical expressions describing the nuclei size spectrum. The most popular expression is that derived by Junge [1963] for particles greater than r = 0.1 μm

$$\frac{dN}{d(\log r)} = Cr^{-B}, \tag{16.30}$$

where N is the number of nuclei per cm^3 in the radius interval d (log r), and B and C are functions of the drop-size distribution. Measurements from several different parts of the world show, on average, an r^{-3} law, especially in the size range 0.05 μm through 1.0 μm. Below a radius of 0.05 μm, the number of Aitken nuclei begins to decrease with decreasing size.

There are 3 primary sources of origin of nuclei: (1) soil and vegetation, (2) sea spray, and (3) combustion. Depending on their origin, the nuclei normally contain various quantities of SO_x, NH_x NO_x Cl, and Na. The SO_x and NO_x are primarily from industrial or combustion sources, Cl is from industrial sources as well as the sea, NH_x is from decaying organic matter, and Na is from the sea and exists primarily as sodium chloride.

Depending on the size and hygroscopicity of the particles, condensation may begin when the relative humidity is as low as 70%. As the humidity rises due either to additional moisture or a lowering of the temperature, the particles continue to grow and form a haze. When a slight supersaturation occurs, the particles quickly grow into fog droplets. The type and concentration of hygroscopic particles and the amount of superasaturation are the primary factors that affect the fog drop size distribution and resulting visibility.

16.4.1.2 Drop Size Distributions. There are two primary techniques for measuring fog drop-size distributions: impaction and light scattering. In the impaction technique, droplets are impacted on a glass slide which is usually coated with gelatin or some oily substance, the droplets leaving impressions on the slide. The impressions are then later counted and sized to determine the drop size distribution. The 3 primary disadvantages of this technique are (1) the tedious and time consuming process of counting and sizing

the droplets, (2) the low collection efficiencies of the smaller droplets resulting in unreliable counts below about 4 μm radius, and (3) fog-laden air must be drawn through a small opening, thus creating problems with obtaining representation samples. In recent years the light-scattering technique has become much more reliable and popular. The advantages of this technique are the near real time readout of the drop size distribution and the ability to measure the smaller droplets. The main disadvantage of most light scattering instrumentation is that, like the impaction technique, droplets must be drawn into the sample volume through a narrow opening.

Most impaction techniques show droplet radii ranging from 2 to 40 μm with a peak or mode in the number concentration occurring around 5 to 10 μm. Recent light-scattering techniques, however, reveal that the droplet count frequently continues to increase at radii below 5 to 10 μm. An example of this is described in Figure 16-53 which shows four comparisons of fog droplet spectra at Otis AFB, Mass., each measured simultaneously with a Calspan droplet sampler (which uses gelatin coated slides), and a Particle Measuring System forward scatter spectrometer probe (FSSP-100) [Kunkel, 1981].

Using the FSSP-100, Kunkel [1982] shows three basic types of distributions in advection fogs at Otis AFB (Figure 16-54). The common feature of the three distributions is that the maximum concentration per micron diameter interval occurs below 2 μm, apparently the result of inactive or haze nuclei. The middle spectrum (Type B) was the most typical of the distributions observed at Otis AFB, showing a primary mode between 0.5 and 2 μm, a secondary mode or plateau between 5 and 10 μm and a plateau between 15 and 30 μm. Type A has a mode in the 15 to 30 μm plateau. This type of distribution was quite common in radiation fogs observed at Hanscom AFB, Mass. Type C spectra show no plateau or peak but a steady decrease in concentration which can be represented by a power law curve [Junge, 1963].

16.4.1.3 Liquid Water Content. The liquid water content (LWC) of fog can be measured through a variety of techniques. One technique is to collect the liquid water on some type of absorbent filter paper over a specific time period. The paper is weighed before and after collection, and the increase in weight can then be converted to LWC. There are various types of hot-wire devices in which the droplets impact on electrically heated wire and subsequently evaporate and cool the surface of the wire. The magnitude of the cooling is a measure of the LWC. The LWC also can be determined by integrating the drop-size distribution curves, assuming the volume of air sampled is known. A small wind tunnel or blower is necessary with all of these techniques, in order to draw the sample into the sampling surface or through the sampling area.

Measurements of LWC in fog have been very sparse. Therefore, it is difficult to obtain any type of statistics on
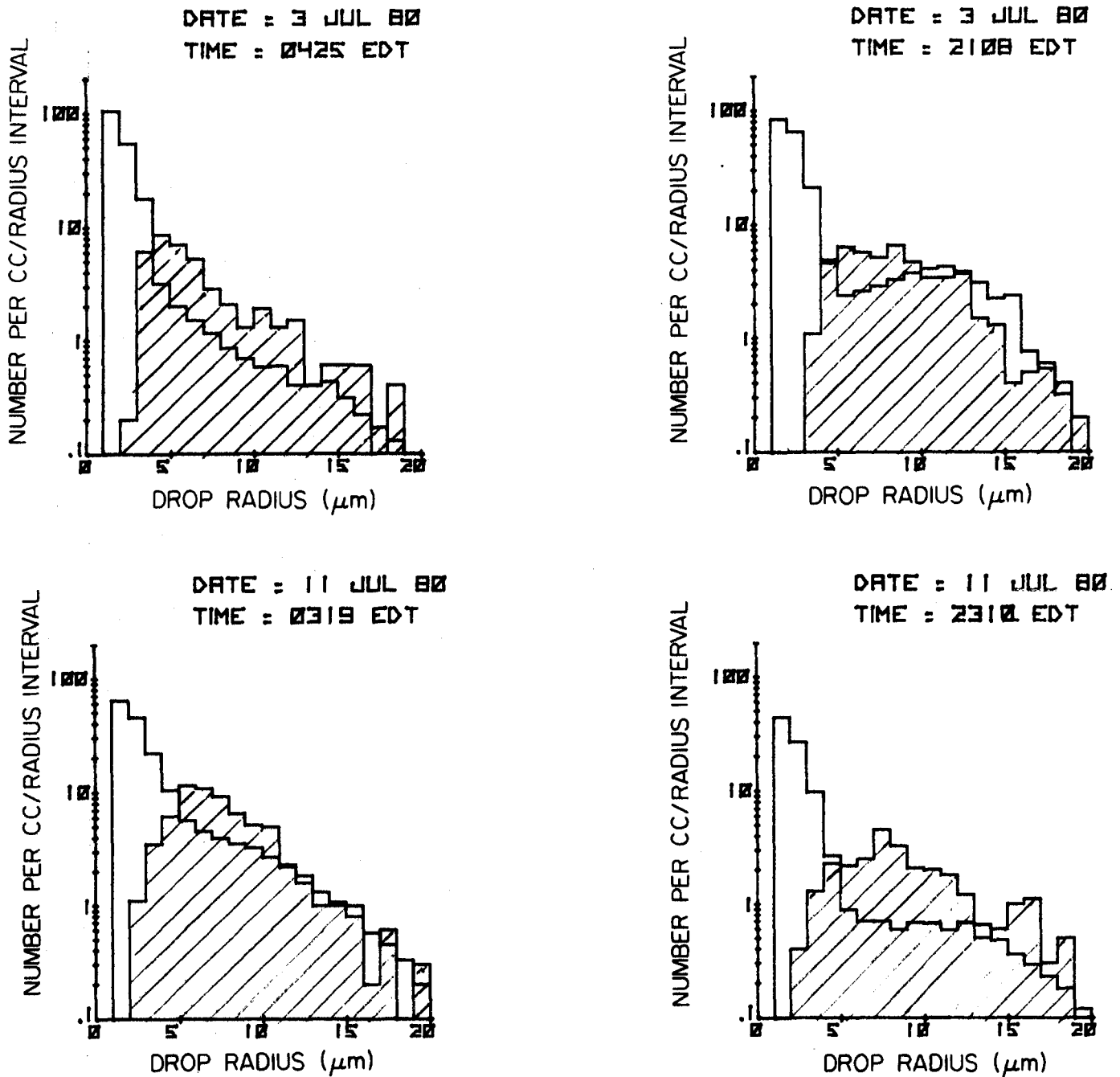
Figure 16-53. Four examples of droplet concentration spectra from the Calspan sampler (hatched area) and the FSSP-100.

the frequency of LWC amounts. Recently however, Kunkel [1982] determined the LWC from 400 samples during 7 advection fogs at Otis AFB by integrating the drop-size distributions which were averaged over 5-min periods. Figure 16-55 shows the percentage of time that the LWC at 5 m and 30 m above the ground is below a given value. The data include all samples with a liquid water content of at least 0.01 g/m³ at the 5 m level. The average LWCs were 0.03 and 0.17 g/m³ and the maximum LWCs were 0.33 and 0.48 g/m³ at the 5- and 30-m levels, respectively.

16.4.2 Visibility

16.4.2.1 Definitions. There are several terms commonly used to describe the opacity of the atmosphere. Some of these terms and their definitions are

Visibility—A subjective evaluation of the greatest distance in a given direction at which it is just possible to see and identify with the unaided eye in the daytime a prominent dark object against the sky at the horizon, and at night a known, preferably unfocused, moderately intense light source.
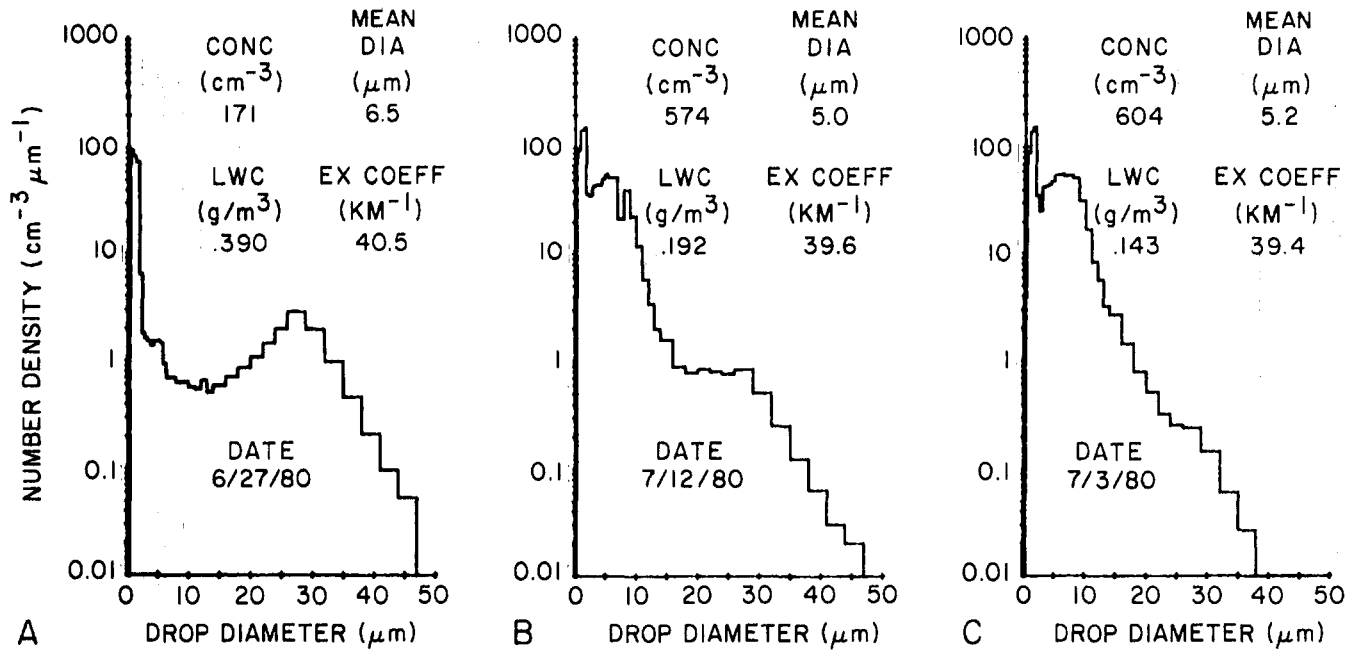
Figure 16-54. Example of three types of drop size distributions in advection fogs at Otis AFB, Mass. [Kunkel, 1981].

Prevailing Visibility—The greatest horizontal visibility that is equaled or surpassed throughout half of the horizon circle. This value is entered in surface weather observations.

Daytime Visual Range—The distance at which the apparent contrast between a specified type of target and its background becomes just equal to the threshold contrast of an observer. Daytime visual range V is a function of the extinction coefficient of the atmosphere k, the threshold contrast of the observer's eyes ε, and the viewing angle. The relationship can be described by Koschmieder's Law [1924]

$$V = \frac{1}{k} \ln \frac{I}{\varepsilon}. \qquad (16.31)$$

Nightime Visual Range—The greatest distance at which a point source of light of a given candle-power can be perceived by an observer under given atmospheric conditions. Nighttime visual range V is a function of extinction coefficient of the atmosphere k, the candle-power of the point source I and the threshold illuminance for the observer's eyes E. The relationship can be described by Allard's Law [1876]

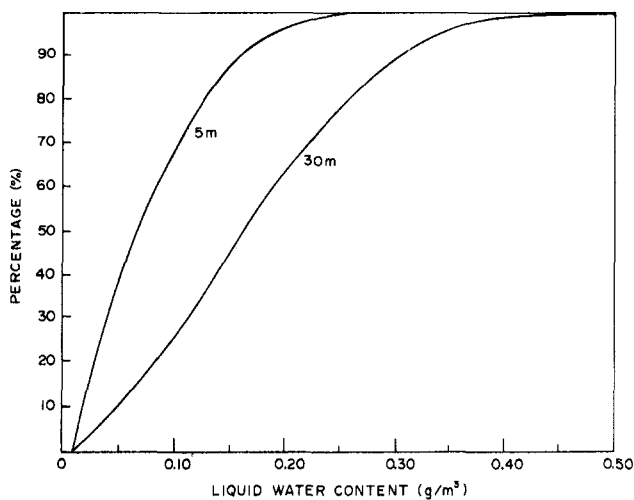$$V^2 = \frac{I}{E} \exp(-kV). \qquad (16.32)$$

Threshold Contrast (ε)—The smallest contrast of luminance that is perceptible to the human eye. The threshold contrast value can vary from 0.005 to 5.0 depending on the observer and the brightness and visual angle of the target. An average threshold contrast of 0.055 is normally used.

Threshold Illuminance (E)—The lowest value of illuminance which the eye is capable of detecting under specified conditions of background luminence and degree of dark adaption of the eye. A value of 10^{-1} lumens per km^2 is normally used.

Extinction Coefficient (k)—A measure of the space rate of extinction of any transmitted light. The extinction coefficient is a function of the concentration N and radius r of particles in the atmosphere; it can be calculated by the following.

Figure 16-55. The percentage of time that the liquid water content at 30 and 5 m above the ground is below a given value [Kunkel, 1981].

$$k = \pi \sum_{i=1}^{n} K_i N_i r_i^2, \qquad (16.33)$$

where K is the scattering area ratio for a given particle size i. K is normally given a value of 2.

16.4.2.2 Variability. The variability of visibility in fog has been the subject of numerous recent studies, such as Chisholm and Kruse [1974a], Chisholm [1974], Chisholm and Kruse [1974b], Brown [1979], and Jiusto and Lala [1980]. The first four papers present analytical results of data collected in AFGL research projects during the last ten years. For example, an automated mesoscale weather network was in operation in eastern Massachusetts from 1972 to 1976 and was followed by the establishment of a weather facility at Otis AFB, Mass. on Cape Cod. All visibility measurements were obtained using forward-scatter-meters (FSM) whose characteristics have been previously described [Muench et al., 1974]. The visibility measurements in this section will be expressed either in terms of atmospheric extinction coefficient $(\times 10^{-4}/m)$ as directly measured by the FSM, or a daytime sensor equivalent visibility (SEV) as defined by George and Lefkowitz [1972]. The daytime SEV is equivalent to the daytime visual range defined in the previous section.

The presentation of the variability of visibility in fog will be divided into three parts: (1) *temporal variability;* (2) *horizontal variability* and (3) *vertical variability.* Measures of variability are the simple correlation coefficient r, and the standardized error of estimation (SE) or persistence error computed from

$$SE = [(1 - r^2) \sigma^2]^{1/2}, \qquad (16.34)$$

where σ^2 is the percent variance of the dependent variable.

Temporal Variability—Chisholm and Kruse [1974a] examined the question of obtaining visibility at an airport with less than three small-volume visibility instruments along a runway and produced an insight into the temporal variability of fog. Figure 16-56 shows the resulting plots of persistence error for a single instrument (W) and a three-instrument mean based on autocorrelations with time lags from 1 to 90 min. They restricted the data to night-time observations to avoid sunrise-sunset effects. The instruments were situated on both sides of the runway. Distances between the central site and the two extremes were 1240 and 1280 m; the distance between the two extreme sites was 2400 m.

The single-station and three-station mean curves are nearly identical for advection fog. They show a rapid increase in persistence errors during the first 10 min and consistently lower persistence errors than the radiation fog cases. The similarity of the single- and three-instrument means validates existence of a higher degree of homogeneity in advection fog. On the other hand, in the radiation fog cases, the single- and three-station means differ widely and have consistently higher persistence errors than advection fog,
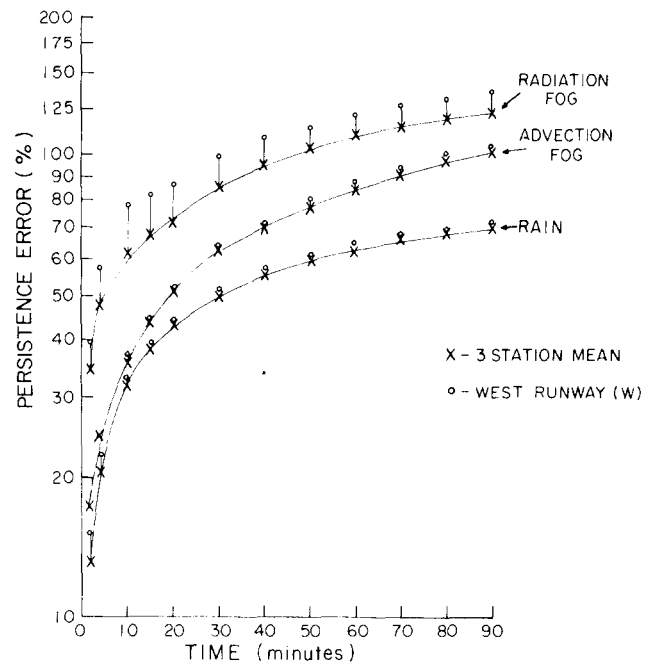
16-50

Figure 16-56. Temporal variability of SEV persistence error as a function of restriction cause [Chisholm and Kruse, 1974a].

indicating more rapid changes in visibility over short distances and time intervals.

Figure 16-57 is a time section of visibility (SEV) observed at the three instruments at Hanscom AFB during a radiation fog. The rapid and erratic fluctuations of visibility in time and space are clearly shown.

A 45-m tower located about 1000 m north of the west runway instrument (W) was also instrumented with forward-
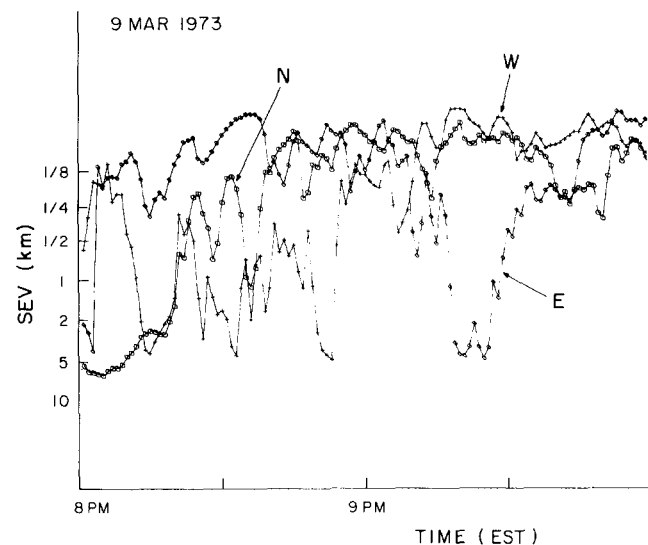

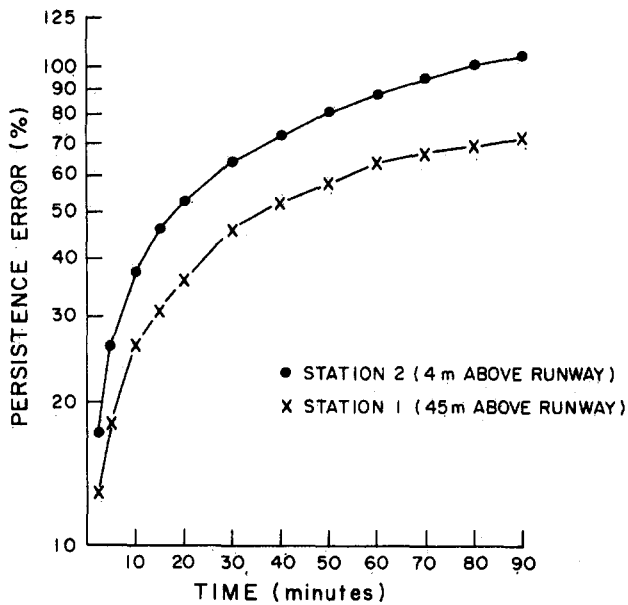Figure 16-57. Short time plot of SEV at three locations along Hanscom AFB runway in a radiation fog episode [Chisholm and Kruse, 1974a].

Figure 16-58. Time dependent persistence error of SEV as a function of sensor height above ground [Chisholm and Kruse, 1974b].

Figure 16-59. Time plot of SEV from two sensors collocated at east end of runway in a radiation fog episode [Chisholm and Kruse, 1974a].

scatter-meters. Figure 16-58 shows for advective fog cases that the persistence error is consistently less at higher levels indicating a greater degree of homogeneity in advection fog with height.

Horizontal Variability—Chisholm and Kruse [1974a] compared simultaneous readings of two forward-scatter-meters separated horizontally by 3 m to obtain a measure of the accuracy and representativeness of the individual sensor observations. They found that the advective and radiation fog variability at this scale is on the order of 8% and 13%, respectively. Figure 16-59 shows a 1-h sample of the simultaneous observations during a period of radiation fog when visibility varied from 10 km to less than 100 m.

Figure 16-60 is a plot of forward-scatter-meter extinction coefficient measurements made at the Otis Weather Test Facility at Otis AFB, Mass., during an advection fog on 5 Nov 1978. For comparative purposes, an extinction coefficient of 30 × 10⁻⁴/m denotes a daytime SEV of approximately 1 km while a reading of 210 × 10⁻⁴/m represents an SEV of about 140 m, assuming a contrast threshold of 0.055. These measurements were made by instruments located at the 30-m level of four towers (A, B, P and Q). Towers P, A, and Q were oriented southeast-northwest at 500-m intervals. Tower B was located about 85 m southwest of Tower A, the center tower of the line. The graph shows the degree of homogeneity that existed over these distances in one particular case.

Chisholm and Kruse [1974a] also evaluated the degree of homogeneity in radiation and advection fogs along a runway (locations W, N, and E; see *temporal variability*) by examining observations at two points on the runway given the conditions at a third. Table 16-36 presents a summary of the two distributions, labeled midpoint and rollout,
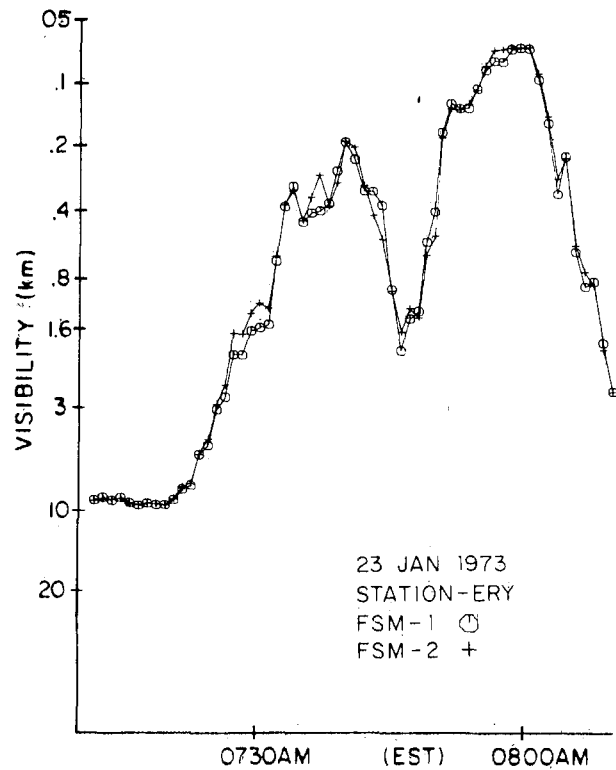
for 5 classes of visibility restriction at the touchdown point. Data from the radiation and advection fogs have been further stratified so that each end of the runway (W and E) becomes a touchdown point. The principal diagonal in each table represents the homogeneous condition, that is conditions at mid- and endpoints of runway are the same as at the touch-
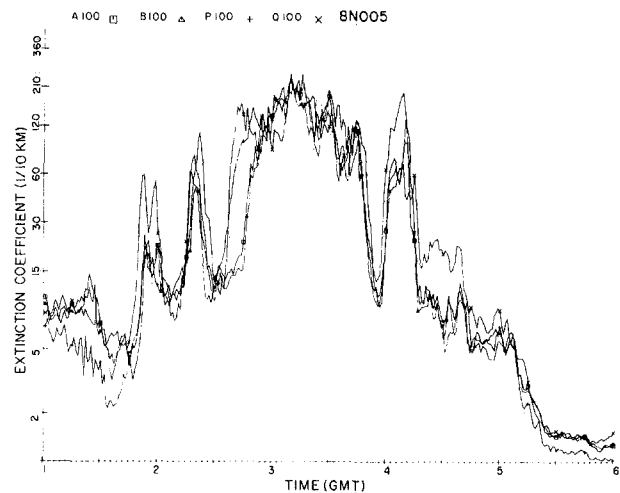

Figure 16-60. Time series of atmospheric extinction coefficient (1-min averages) measured at the 29 m levels at towers A, B, P, and Q on 5 November 1978 during fog.

16-51

Table 16-36. Conditional frequency distribution along Hanscom AFB Runway of equivalent daytime SEV.

Restriction Cause	Touchdown Location	SEV Range (m)	Midpoint Distribution > 1600	800– 1600	400– 800	200– 400	0– 200	Rollout Distribution > 1600	800– 1600	400– 800	200– 400	0– 200
Radiation Fog	W	>1600	80	9	3	5	4	77	8	2	5	7
		800–1600	49	14	12	8	17	54	8	8	8	22
		400–800	23	5	18	21	32	42	12	6	21	20
		200–400	10	*	7	32	50	16	11	23	35	15
		0–200	8	0	7	31	55	9	5	7	42	37
	E	>1600	84	5	3	4	4	84	6	3	3	3
		800–1600	49	10	13	16	11	62	6	7	14	12
		400–800	26	6	8	34	27	24	8	5	40	23
		200–400	23	5	4	24	44	19	3	6	23	49
		0–200	11	15	12	17	45	28	9	6	10	47
Advection Fog	W	>1600	96	4	*	*	0	93	7	*	0	0
		800–1600	16	78	5	1	0	12	78	10	1	0
		400–800	1	18	78	3	0	2	22	63	13	0
		200–400	0	0	10	85	5	0	0	4	79	17
		0–200	0	0	0	24	76	0	0	0	2	98
	E	>1600	98	2	*	*	0	96	4	*	0	0
		800–1600	19	76	5	0	0	20	71	9	0	0
		400–800	0	21	75	3	0	*	25	71	4	0
		200–400	0	0	22	76	2	0	2	16	81	*
		0–200	0	0	0	47	53	0	0	0	44	56
All Restrictions	W	>1600	94	4	1	1	*	90	7	1	1	1
		800–1600	18	74	7	1	*	11	79	8	1	1
		400–800	3	15	76	4	2	5	25	57	12	1
		200–400	2	*	11	73	14	4	3	10	71	12
		0–200	4	0	4	24	68	7	4	5	32	52
	E	>1600	96	3	*	1	*	95	3	1	*	*
		800–1600	23	67	9	1	*	22	66	10	1	1
		400–800	5	17	69	6	3	6	19	64	8	3
		200–400	5	1	19	62	12	6	2	14	62	16
		0–200	6	7	6	28	53	16	5	4	22	53

*less than 1%

down point. The significantly higher variability of the radiation fog is very apparent, for example, with a touchdown visibility between 400 and 800 m the corresponding visibility at the midpoint and rollout are in the same range only 18% and 6% of the time for the West (W) touchdown and 8% and 5% for the East (E) touchdown. For advective fog the midpoint frequencies are in the same range 78% and 76% and rollout frequencies 63% and 57%. Disparity between these results and those reported by Schlatter and Lefkowitz [1968], which showed more variability at airports located at Atlantic City, N.J. and Los Angeles, Calif., can be attributed to different climatic regimes and to different observing systems. The transmissometer used in the Schlatter and Lefkowitz [1968] report was compared with the FSM

by Muench et al. [1974] and was found to have an inherent overall error of ± 20% due to calibration drift and instrument noise as compared to the ± 4% of the FSM.

Figure 16-61 shows a comparison of spatial variability at Hanscom AFB with variabilities reported by Hage and Entrekin [1965] for Kennedy Airport, N.Y., and by Hage and Wilson [1967] for Atlantic City, N.J. Chisholm and Kruse [1974a] imply that a significant part of the variability at Kennedy and Atlantic City is due to use of the transmissometer as a measuring system rather than to natural causes. Figure 16-61 illustrates horizontal variability over distances ranging from 0.4 to 3 km in radiation and advection fog. Figure 16-62 represents a compilation of space correlations in the range 5 to 40 km for station pairs carefully
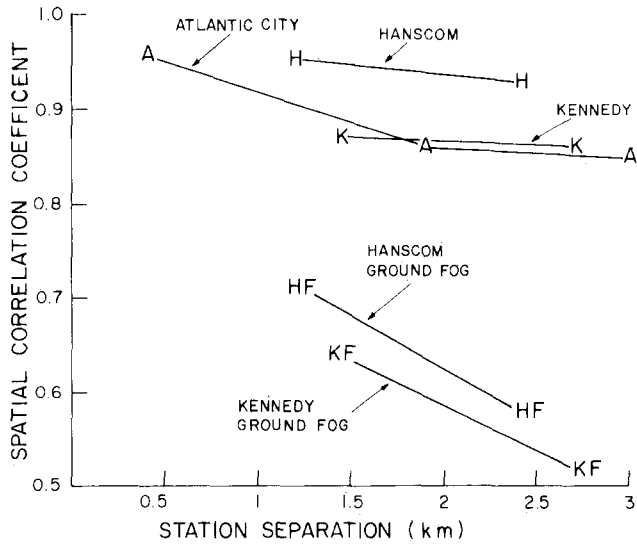
Figure 16-61. Comparison of horizontal variability of SEV at three airport locations [Chisholm and Kruse, 1974a].

selected from the AFGL Mesonetwork to eliminate coastal and hilltop effects and to insure similar elevations. The decay in correlation as a function of station separation is clearly evident in the advection fog and quite dramatic in the case of radiation fog. Because radiation fog rarely is found in the eastern part of the network, the station pairs for this class restriction were limited to 15 km.

Vertical Variability—The AFGL Mesonetwork, in addition to numerous surface weather stations, contained one tower at Hanscom AFB which was instrumented at the 30
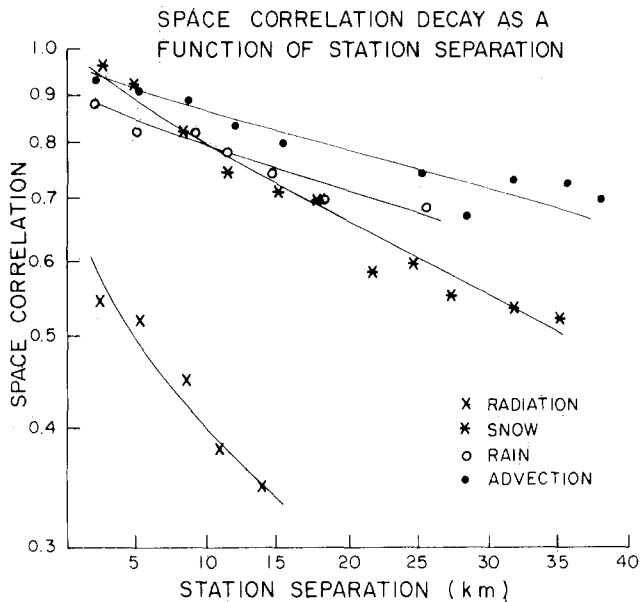
and 45 m levels. Figure 16-63 from Chisholm and Kruse [1974a] shows the cumulative frequency distribution of visibility in advective fogs (and rain cases) at three levels: ground, 30 m, and 45 m. The figure shows a dramatic increase of reduced visibility with height. For example, during advective fog, visibilities (SEV) greater than 400 m occur about 90% of the time at the surface, while at the 45 m level, they occur only 65% of the time.

Figure 16-64 shows a typical time section of the vertical variation of visibility (extinction coefficient) at Otis AFB, Mass., on 5 Nov 1978 during an advection fog. Five levels, from 3 m(X) to 57 m(A200), of visibility were plotted. The striking decrease in visibility (increase in extinction coefficient) with height is readily apparent. Figure 16-65, on the other hand, shows a time section of visibility when a typical ground fog occurred. The same levels of the tower are shown. The striking feature in this figure is the complete reversal of visibility gradient, with the surface instrument (X) recording the lowest visibility.

16.4.2.3 Relationship Between Extinction Coefficient and Liquid Water Content.

A direct relationship exists between the extinction coefficient and the amount of liquid water in a cloud. However, the extinction coefficient in the visible part of the spectrum is also inversely related to the radii of the droplets. In other words, a large-droplet fog with a given liquid water content will yield a lower extinction (higher visibility) than a small-droplet fog with the same liquid water content. Eldridge [1966] suggested that the extinction coefficient (σ) and the liquid water content (W) can be related by the empirical formula
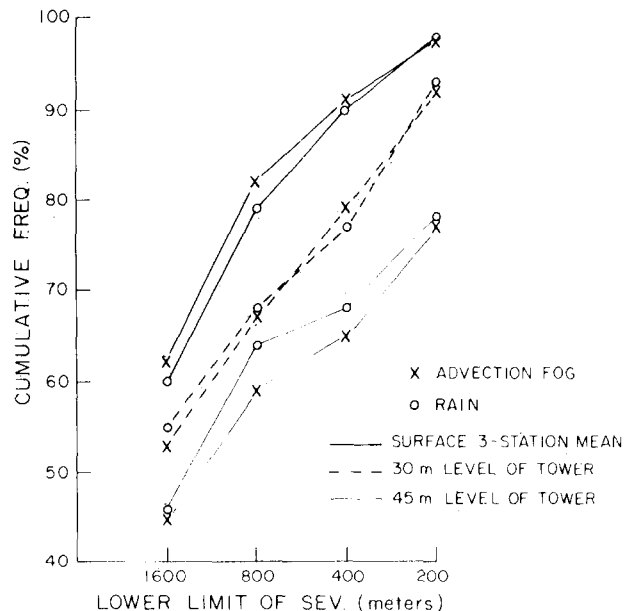

Figure 16-62. Average spatial correlation of SEV in the Hanscom mesonetwork during various types of restrictions [Chisholm and Kruse, 1974b].

Figure 16-63. Cumulative frequency distribution of SEV at three levels above the Hanscom AFB runway [Chisholm, 1974].
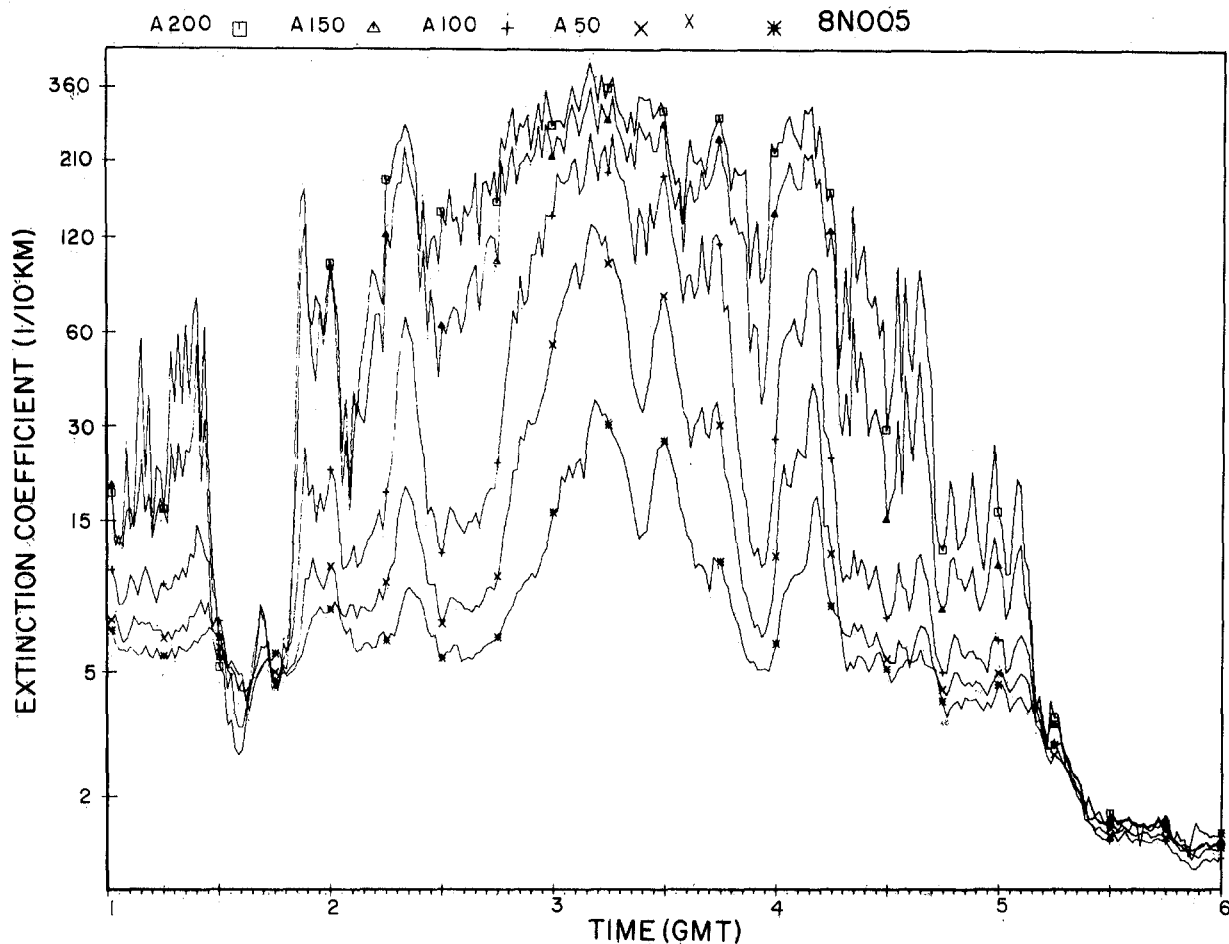
16-53

Figure 16-64. Time series of atmospheric extinction coefficient (1-min averages) measured at the 57-m(A-200), 48-m(A-150), 29-m(A-100) and 16-m (A-50) levels of tower A and at the 3-m (x) level of site x on 5 November 1978 during fog.

$$\sigma = 163W^{0.65}, \qquad (16.35)$$

where σ is in 1/km and W in g/m³. The Eldridge relationship was derived from somewhat questionable drop-size data and would probably hold true only in a highly polluted, foggy environment such as might occur near an industrial area.

Kunkel [1982], using 1525 drop-size distributions from eight advection fog cases, arrived at the following formula:

$$\sigma = 155 \ W^{0.94}. \qquad (16.36)$$

He found, however, that the coefficient varied from 110 in a large-droplet fog with drizzle to 253 in a small-droplet fog and the exponent varied from 0.96 to 1.14. For all practical purposes a linear relationship can be assumed, but the slope will depend on the drop size distribution.

Chylek [1978] found that at a wavelength of 11 μm there is an unambiguous relation between the extinction coefficient and the liquid water content, independent of the size distribution, in fogs with droplets up to 28 μm diameter. That relationship is as follows:

$$\sigma = 128W. \qquad (16.37)$$

Since the relationship is unique to all fogs, one can determine the extinction coefficient at a wavelength of 11 μm from the LWC measurements and vice versa.

16.4.2.4 Modeling of Visibility Distributions.

The Weibull Distribution has been used for visibility

$$\hat{F}(x) = 1 - \exp(-\alpha x^{\beta}), \qquad (16.38)$$

where x stands for visibility, and α and β are parameters. Estimates for α and β are made to minimize the sums of squares of the differences between the model estimates $\hat{F}(x)$ and the cumulative frequencies F(x) of the climatic summaries.

At the University of Central Florida [Somerville et al., 1979] sets of values for α and β have been determined for each of the eight periods of the day in each month at some 22 stations around the world, to make the estimated cumulative distributions $\hat{F}(x)$ fit the data for some 15 visibil-

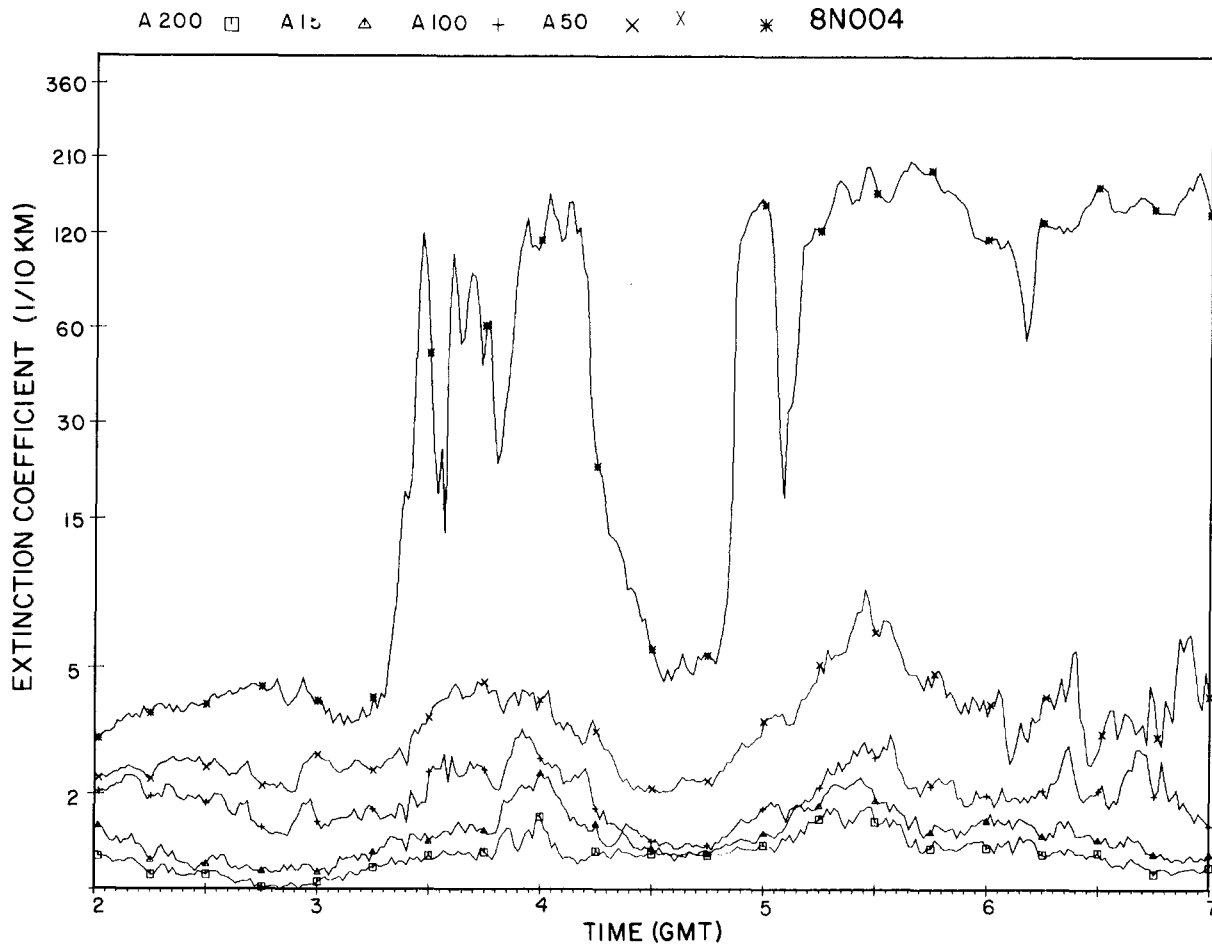A 200 □   A 1⅄ △   A 100 +   A 50 ×   X   ✳ 8N004

Figure 16-65. Time series of atmospheric extinction coefficient at the same levels as shown in Figure 16-64 (observations taken on 4 November 1978 during ground fog).

Table 16-37. A sample of cumulative frequency distribution of visibility in kilometers. (The station is Bedford, Mass., January noontime. Probability estimates were made by the Weibull distribution, with parameter values $\alpha = 0.04679$, $\beta = 0.81856$.)

Visibility (km)	RUSSWO Frequency	Model Probability
0.4	0.018	0.022
0.5	0.028	0.026
0.8	0.034	0.038
1.0	0.053	0.046
1.2	0.056	0.053
1.6	0.072	0.067
2.0	0.094	0.080
2.4	0.099	0.092
3.2	0.116	0.115
4.0	0.135	0.136
4.8	0.146	0.156
6.4	0.184	0.193
8.0	0.221	0.227
9.7	0.254	0.259
16	0.377	0.365

ities (in kilometers) corresponding to those in the climatic summaries.

A simpler method for solving for α and β utilizes the linear relationship between $\ell n(-\ell n[1 - F(x)])$ and ℓnx. This permits a solution for β and ℓnd by linear regression. As an example, at Bedford, Mass., in January at noontime, α and β were found to be 0.04679 and 0.81856, respectively; the resulting visibility probabilities are compared with RUSSWO data in Table 16-37.

CHAPTER 16

REFERENCES

Air Weather Services, "Forecasters' Guide on Aircraft Icing," AWS-TR-80-0001 Scott AFB, Ill., 1980.

Allard, E., *Memoire sur L'intensite et la Portee des Phares,* Paris, Dunod, 1876, quoted in Middleton, W.E., *Vision Through the Atmosphere,* University of Toronto Press, 1963.

Allen, M., Y.L. Yung, and J.W. Waters, " Vertical Transport and Photochemistry in the Terrestrial Mesosphere and Lower Thermosphere (50–120 km)," *J. Geophys. Res.,* **86:** 3617–3627, 1981.

Anonymous, "Lowest Measured Temperature in the Earth's Atmosphere Recorded in U.S. - Sweden Experiments," *Bull. Am. Meteorol. Soc.,* **44:** 806, 1963.

Appleman, H.S., "Occurrence and Forecasting of Cirrostratus Clouds," Tech. Note 140, World Meteorological Organization (WMO), 1961.

aufm Kampe, H.J., and H.K. Weickmann, "Physics of Clouds," *Meteorol. Monographs,* **3:** 182, 1957.

Bannon, B.A. and J.P. Steele, "Average Water Vapor Content of the Air," Geophys. Memoirs No. 102, Meteorological Office, Air Ministry, London, 1960.

Barnes, A.A., "New Cloud Physics Requirements," *Preprints 4th Symp. on Meteorological Observations and Instrumentation,* American Meteorological Society, Boston, Mass., 1978.

Barnes, A.A., "Observations of Ice Particles in Clear Air," *Journal de Recherches Atmospheriques* **14:** 311–315, 1980.

Barnes, A.A., "Ice Particles in Clear Air," *Preprints 8th International Conf. on Cloud Physics,* Clermont-Ferrnad, France, 15–19 July 1980, pp 189–190, AFGL TR-81-0009, AD094444, 1981.

Barnes, A.A., "The Cirrus and Subvisible Cirrus Background," *Preprints 2nd Symp. on Composition of Non-Urban Troposphere,* American Geophysical Union, Williamsburg, Va., May 1982.

Bean, S.J., P.N. Somerville, M. Heuser, "Some Models for Ceiling," AFGL TR-79-0221, ADA078033, 1979.

Beckwith, W.B., "Analysis of Hailstorms in the Denver Network, 1949–1958," *Physics of Precipitation,* edited by H. Weidkman, American Geophysical Union, Washington, D.C., 348–353, 1960.

Bennett, I., "Glaze, Its Meteorology and Climatology, Geographic Distribution and Economic Effects," Tech. Rept. EP-105, Quartermaster Research and Engineering Center, Envir. Prot. Res. Div., Natick, Mass., 1959.

Bertoni, E.A., "Clear Lines-of-Sight from Aircraft," AFCRL 67-0435, AD657801, 1967.

Bertoni, E.A., "Clear and Cloud-Free Lines-of-Sight from Aircraft," AFGL TR-77-0141, ADA046352, 1977a.

Bertoni, E.A., "Clear and Cloud-Free Lines-of-Sight from Aircraft," AFGL TR-77-0141, ADC 015057 1977b.

Best, A.C., "The Size Distribution of Raindrops," *Quart. J. Roy. Meteorol. Soc.,* **76:** 16, 1950.

Boyd, D.W., "Maximum Snow Depths and Snow Loads on Roofs in Canada," Research Paper 142, Div. of Building Research, National Research Council, Ottawa, Canada, 1961.

Brewer, A.W., "Evidence for a World Circulation Provided by Measurement of Helium and Water Vapor Distribution in the Stratosphere," *Quart. J. Roy. Meteorol. Soc.,* **75:** 351–363, 1949.

Brown, H.A., "Preliminary Assessment of an Automated System for Detecting Present Weather," AFGL TR-79-0137, ADA07831, 1979.

Bundy, D.S., "A Two-Year Study of the Probability of Cloud-Free Lines-of-Sight at Columbia, Mo.," Unpublished Masters Dissertation, University of Missouri, Columbia, 1969.

Bussey, H.E., "Microwave Attenuation Statistics Estimated from Rainfall and Water Vapor Statistics," *Proc. IRE,* **38:** 781, 1950.

Changnon, S.A., "Hailstreaks," *J. Atmos. Sci.,* **27:** 109–125, 1970.

Changnon, S.A., "Means of Estimating Areal Hail-Day Frequencies," *J. Wea. Modifica.,* **3:** 154–158, 1971.

Chisholm, D.A., "The Mesoscale Variability of Visibility in Time and Space," Proceedings 5th Conference on Weather Forecasting and Analysis, St. Louis, Mo., American Meteorological Society, Boston, Mass., 1974.

Chisholm, D.A. and H. Kruse, "The Variability of Airfield Visibility: A Preliminary Assessment," AFCRL TR-74-0027, AD777219, 1974a.

Chisholm, D.A. and H. Kruse, "The Variability of Airfield Visibility: A Preliminary Assessment," AFCRL TR-74-0265, AD784791, 1974b.

Chylek, P., "Extinction and Liquid Water Content of Fogs and Clouds," *J. Atmos. Sci.,* **35:** 290–300, 1978.

Cohen, I.D., "Development of a Large Scale Cloud System, 23–27 Mar 78," AFGL TR-81-0127, ADA106417, 1981a.

Cohen, I.D., "Cirrus Particle Distribution Study, Part 8," AFGL TR-81-0316, ADA118715, 1981b.

Cole, A.E., R.J. Donaldson, D. Atlas, A.J. Kantor, R.K. Soberman, and J.E. Manson, "Precipitation, Clouds, and Aerosols," Chapter 5, *Handbook of Geophysics and Space Environments,* AFCRL, 1965.

Cole, A.E. and A.J. Kantor, "Air Force Reference Atmospheres," AFGL TR-78-0051, AD058505, 1978.

Crane, A.K., "Prediction of Attenuation by Rain," *IEEE Trans. Comm.* **COM-28:** 1717–1733, 1980.

Crutcher, H.L. and J.M. Meserve, "Selective Level Heights, Temperatures and Dew Points for the Northern Hemisphere," Naval Weather Service Command, NAVAIR 50-IC-52, U.S. Government Printing Office, Washington, D.C., 1970.

Crutzen, P.A., "A Review of Upper Atmospheric Photochemistry," *Can. J. Chem.,* **52:** 1569–1581, 1974.

Davis, A.R. and D.J. McMorrow, "Stochastic Models for Deriving Instantaneous Precipitation Rate Distributions," USAF Air Weather Service, AWS-TR-76-263, 1976.

deBary, E. and F. Moller, "The Vertical Distribution of Clouds," *J. Appl. Meteorol.,* **2:** 806–808, 1963.

Deirmendjian, D., "Scattering and Polarization Properties of Water Clouds and Hazes in the Visible and Infrared," *Appl. Opt.,* **3:** 187–196, 1964.

Derr, V.E., "A Basic Comparison of Lidar and Radar for Remote Sensing of Clouds," Tech. Rept. ERL 397-WPL 52, Wave Propagation Laboratory, NOAA, Boulder, Colo., 1978.

Deguchi, S. and D.O. Muhleman, "Mesospheric Water Vapor," *J. Geophys. Res.*, **87:** 1343–1346, 1982.

Ehhalt, D.H., L.E. Heidt, R.H. Lueb, and E.A. Martell, "Concentrations of CH_4, CO, CO_2, H_2, H_2O, and NO_2 in the Upper Stratosphere," *J. Atmos. Sci.*, **32:** 163–169, 1975.

Eldridge, R.G., "Haze and Fog Aerosol Distributions," *J. Amos. Sci.*, **23:** 605–613, 1966.

Falls, L.W., "The Beta Distribution: A Statistical Model for World Cloud Cover," NASA TM X-64714, Marshall Space Flight Center, Ala., 1973.

Farmer, C.B., O.F. Raper, B.D. Robbins, R.A. Toth, and C. Muller, "Simultaneous Spectroscopic Measurements of Stratospheric Species O_2, CH_4, CO, CO_2, N_2O, H_2O, HCL, and HF at Northern and Southern Mid-Latitudes," *J. Geophys. Res.*, **85:** 1621–1632, 1980.

Feldman, N.E., "Rain Attenuation Over Earth-Satellite Paths," Science Applications, Inc., Final Report on Contract N00039-79-C-0136 for Naval Electronic Systems Command, ADA075390, 1979.

Fett, R.W., J.J. Bates, W.A. Bohan, R.J. Englebretson, J. Rosenthal, and G.A. Stevenson, *Navy Tactical Applications Guide, Vol. 3, North Atlantic and Mediterranean Weather Analysis and Forecast Applications,* NEPRF Tech. Report 80-07, Monterey, Calif., 1981.

Frederick, R.H., V.A. Meyers, and E.P. Auciello, "Five-to 60-Minute Precipitation Frequency for the Eastern and Central United States," NOAA Tech. Memo. NWS HYDRO-35, 1977.

George, D.M., and M. Lefkowitz, "A New Concept: Sensor Equivalent Visibility," Proceedings International Conference on Aerospace and Aeronautical Meteorology, Washington, D.C., American Meteorological Society, 1972.

Glass, M. and D.D. Grantham, "Response of Cloud Microphysical Instruments to Aircraft Icing Conditions," AFGL TR-8l-0192, ADA112317, 1981.

Grantham, D.D., I.A. Lund, and R.E. Davis, "Estimating the Probability of Cloud-Free Fields-of-View Between Earth and Airborne or Space Platforms," Air Weather Service Tech. Rept. 79-001, 1979.

Gringorten, I.I., "Hailstone Extremes for Design," AFCRL 72-0081, AD743831, 1971.

Gringorten, I.I., "Probability Models of Weather Conditions Occupying a Line or an Area," *J. Appl. Meteorol.*, **18:** 957–977, 1979.

Gringorten, I.I., "Climatic Probabilities of the Vertical Distribution of Cloud Cover," AFGL-TR-82-0078, ADA118753, 1982.

Gringorten, I.I., H.A. Salmela, I. Solomon, and J. Sharp, "Atmosphere Humidity Atlas—Northern Hemisphere," AFCRL 66–621, AD642429, 1966.

Gunn, K.L.S. and T.W.R. East, "The Microwave Properties of Precipitation Particles," *Quart. J. Roy. Meteorol. Soc.*, **80:** 522–545, 1954.

Gunn, K.L.S. and J.S. Marshall, "The Distribution with Size of Aggregate Snowflakes," *J. Meteorol.*, **15:** 542, 1958.

Gutnick, M., "How Dry is the Sky?", *J. Geophys. Res.*, **66:** 2867–2871, 1961.

Hage, N. and H. Entrekin, "Further Studies of Space and Time Variations in Atmospheric Transmission Along Airport Runways," TR7417-143, The Travelers Research Center, Inc., Hartford, Conn., 1965.

Hage, N. and J. Wilson, "Analyses of the Variability of Clouds, Fog, Wind and Rain in the Atlantic City Mesonetwork," TN7481-262, The Travelers Research Center, Inc., Hartford, Conn., 1967.

Hall, G.R., "On the Mechanics of Transition Produced by Particles Passing Through on Initially Laminar Boundary Layer and the Estimated Effect on the LFC (Laminar Flow Control) Performance of the X-21 Aircraft," Northrop Aircraft Report, October 1964.

Hall, W.D. and H.R. Prupacher, "The Survival of Ice Particles Falling from Cirrus Clouds in Saturated Air," *J. Atmos. Sci.*, **33:** 1995–2006, 1976.

Harris, J.E., "The Distribution of Water Vapor in the Stratosphere," *Rev. Geophys. Space Phys.*, **14:** 565–575, 1976.

Haurwitz, B., *Dynamic Meteorology*, McGraw-Hill, New York, 1941.

Heath, E.D., and L.M. Cantrell, "Aircraft Icing Climatology for the Northern Hemisphere," Tech. Rept. 220, Air Weather Service (MAC) USAF, 1972.

Herbstritt, R.L., "Rain Climate Considerations for Domestic Satellites—Continental U.S.," Report R-7301, FCC, Washington, D.C., 1973.

Herman, B.M., "Infrared Absorption, Scattering and Total Attenuation Cross-Sections for Water Spheres," *Quart. J. Roy. Meteorol. Soc.*, **88:** 153–250, 1962.

Heymsfield, A.H., "Cirrus Unicus Generating Cells and the Evolution of Cirriform Clouds, Part I. Aircraft Observations of the Growth of the Ice Phase," *J. Atmos. Sci.*, **32:** 799–808, 1975.

Ho, F.P. and J.T. Riedel, "Precipitable Water over the United States, Vol. II, Semimonthly Mariver," U.S. Dept. of Commerce, NOAA/NWS, Silver Springs, Md., 1979.

Huschke, R.E., H.H. Bailey, R.J. Nelson, and J.P. Bibbo, "An Improved Weather-Attenuation Model for Earth-Satellite Communication Links," Science Applications Inc., Final Report on Contract DAAK80-80-C-0049, U.S. Army Satellite Communications Agency, Ft. Monmouth, N.J., 1982.

Jiusto, J.E. and G.G. Lala, "Thermodynamics of Radiation Fog Formation and Dissipation—A Case Study," *Proceedings 8th International Cloud Physics Conference,* Clermont-Ferrand, France, 15–19 June 1980.

Jones, M.A. and A.L. Sims, "Climatology of Instantaneous Precipitation Rates," AFCRL TR-72-0429, AD748283, 1971.

Jones, M.A. and A.L. Sims, "Climatology of Instantaneous Rainfall Rates," *J. Appl Meteorol.*, **17:** 1135–1140, 1978.

Junge, C.E., *Air Chemistry and Radioactivity*, Academic Press, New York, 1963.

Kantor, A.J. and D.D. Grantham, "A Climatology of Very High Altitude Radar Precipitation Echoes," AFCRL 68-0630, AD681107, 1968.

Kikuchi, K. and A.W. Hogan, "Properties of Diamond Dust Type Ice Crystals Observed in the Summer Season at Amundsen-Scott South Pole Station, Antarctica," *J. Meteorol. Soc. of Japan*, **57:** 180–190, 1979.

Knollenberg, R.G., "Comparative Liquid Water Content Measurements of Conventional Instruments with an Optical Array Spectrometers," *J. Appl. Meteorol.*, **11:** 501–508, 1972.

Koschmieder, H., "Theorie Der Horizontalen Sichtewite," *Beitr. Phys. Atmos.*, **12:** 33–53, 1924. (Cited in Middleton, W.E.K., *Vision Through the Atmosphere*, University of Toronto Press, 1963.)

Kunkel, B., "Comparison of Fog Drop-Size Spectra Measured by Light Scattering and Impaction Techniques," AFGL TR-81-0049, ADA100252, 1981.

Kunkel, B., "Microphysical Properties of Fog at Otis AFB, MA," AFGL TR-82-0026, ADA119928, 1982.

Lamb, K., K.W. Nielson, H.E. Klieforth, and J. Hallett, "Measurements of Liquid Water Content in Winter Conditions Over the Sierra Nevadas," *J. Appl. Meteorol.*, **15:** 763–775, 1976.

Landsberg, H., "Climatology," Chapter XII, in *Handbook of Meteorology*, 1945.

Landsberg, H.E., *World Survey of Climatology*, Vols. I–XV, Elsevier, Amsterdam, The Netherlands, 1974.

Lenhard, R.W., "Precipitation Intensity and Extent," *Journal de Recherches Atmospheriques*, **8:** 375–384, 1974.

Lenhard, R.W. and N. Sissenwine, "Extremes of 1, 12 and 24 Hour Rain for MIL-STD-210B," AFCRL TR-73-0329, AD766210, 1973.

Levin, L.M., "Size Distribution Function for Cloud Droplets and Raindrops," TR-263R, DSNS, Canada, 1954.

Lewis, W., "Meteorological Aspects of Aircraft Icing," *Compendium of Meteorology*, American Meteorol. Society, Boston, Mass., 1951.

Lhermitte, R.M., "Millimeter Wave Doppler Radar," *Preprints 20th Conf. Radar Meteorol.*, American Meteorol. Society, Boston, Mass., 1981.

List, R.J. (ed.), *Smithsonian Meteorological Tables*, Smithsonian Institution Press, Washington, D.C., 1968.

Litvinov, I.V., "The Function of the Distribution of Particles of Liquid Precipitates," *IZV. Acad. Sci.—Geophys.*, **12:** 1474–1483, 1956.

Lo, K.K. and R.E. Passarelli, "The Growth of Snow in Winter Storms: An Airborne Observational Study," *J. Atmos. Sci.*, **39:** 697–706, 1982.

Long, M.J., H.H. Hanks, and R.G. Beebe, "Tropopause Penetrations by Cumulonimbus," AFCRL 65-561, AD621573, 1965.

Lott, G.A., *Precipitable Water Over the United States, Vol. 1, Monthly Means*, U.S. Dept. of Commerce, NOAA/NWS, Silver Springs, Md., 1976.

Ludlum, D.M. (ed.), "Extremes of Snowfall; United States and Canada," *Weatherwise*, **23:** 286–294, 1970.

Lund, I.A., "Haze Free and Cloud-Free Lines-of-Sight Through the Atmosphere," AFCRL 72-0540, AD751264, 1972.

Lund, I.A., "Joint Probabilities of Cloud-Free Lines-of-Sight Through the Atmosphere at Grand Forks, Fargo, and Minot, N. Dak.," AFCRL TR-73-0178, AD763083, 1973.

Lund, I.A. and M.D. Shanklin, "Photogrammetrically Determined Cloud-Free Lines-of-Sight Through the Atmosphere," *J. Appl. Meteorol.*, **11:** 773–782, 1972.

Lund, I.A. and M.D. Shanklin, "Universal Methods for Estimating Probabilities of Cloud-Free Lines-of-Sight Through the Atmosphere," *J. Appl. Meteorol.*, **12:** 28–35, 1973.

Lund, I.A. and E.A. Bertoni, "Some Comparisons Between Probabilities of Cloud-Free Line-of-Sight Estimated from Aircraft and from Sky Cover Observations," AFGL TR-80-0046, ADC021847, 1980.

Lund, I.A., D.D. Grantham, and R.E. Davis, "Estimating Probabilities of Cloud-Free Fields-of-View from the Earth Through the Atmosphere," *J. App. Meteorol.*, **19:** 452–463, 1980.

Lund, I.A., D.D. Grantham, and C.B. Elam Jr., "Atlas of Cloud-Free Line-of-Sight Probabilities", in several parts: *Part 1, Germany*, AFCRL TR-75-0261, ADA013784, 1975. *Part 2, U.S.S.R.*, AFGL TR-77-0005, ADA040705, 1976. *Part 3, U.S.A.*, AFGL TR-77-0188, ADA051112, 1977. *Part 4, Europe*, AFGL TR-78-0276, ADA065167, 1978. *Part 5, North Africa and the Middle East*, AFGL TR-79-0275, ADA088156, 1979.

Marshall, J.S. and W. M. Palmer, "The Distribution of Raindrops with Size," *J. Meteorol.*, **5:** 165, 1948.

Mason, B.J., *The Physics of Clouds*, 2nd Ed., pp 113–121, Clarendon Press, Oxford, England, 1971.

McKay, G.A. and H.A. Thompson, "Estimating the Hazard of Ice Accretion in Canada from Climatological Data," *J. Appl. Meteorol.*, **8:** 927–935, 1969.

McTaggert-Cowan, J.D., G.G. Lala, and B. Vonnegut, "The Design, Construction and Use of an Ice Crystal Counter for Ice Crystal Studies by Aircraft," *J. Appl. Meteorol.*, **9:** 294–299, 1970.

Michaels, D.W., "Noctilucent Cloud Research," *Foreign Sci. Bull.*, **6:** 51–55, Library of Congress, 1965.

Muench, H.S., E.Y. Moroz, and L.P. Jacobs, "Development and Calibration of the Forward-Scatter-Meter," AFCRL TR-74-0145, AD4783270, 1974.

NOC (Naval Oceanography Command), *Guide to Standard Weather Summaries and Climatic Services*, NAVAIR 50-1C-534, Asheville, N.C., 1980.

Pasqualucci, F., B.W. Bertram, R.A. Kropfli, and W.R. Moninger, "A Millimeter Wavelength Dual-Polarization Doppler Radar for Cloud and Precipitation Studies," *J. Clim. Appl. Meteorol.*, **22:** 758–765, 1983.

Pasqualucci, F. and L.J. Miller, "Dual Wavelength Radar Observation in Clouds and Precipitation," *Preprints 20th Conference Radar Meteorology*, American Meteorol. Society, Boston, 1981.

Penndorf, R., "Analysis of Ozone and Water Vapor Field Measurement Data," FAA Tech. Rept., FAA-AEE-78-29, ADA072721, Nov 1978.

Perkins, P.J., *Proceedings, Second Annual Workshop on Meteorological and Environmental Inputs to Aviation Systems,* NASA Conf. Publication 2057: 85–99, 1978.

Plank, V.G., "Hydrometeor Data and Analytical-Theoretical Investigations Pertaining to the SAMS Missile Flights of the 1972–73 Seasons at Wallops Island, Virginia," AFGL TR-77-0149, ADA051192, 1977.

Platt, C.M.R., "Transmission of Submillimeter Waves Through Water Clouds and Fog," *J. Atmos. Sci.,* **27:** 421–425, 1970.

Pochop, L.O. and M.D. Shanklin, "Sky Cover Photograms, A New Technique," *Weatherwise,* **19:** 198–200, 1966.

Rapp, R.R., C. Schutz, and E. Ronriques, "Cloud-Free Line-of-Sight Calculations," *J. Appl. Meteorol.,* **12:** 484–493, 1973.

Riordan, P., "Weather Extremes Around the World," U.S. Army Engineer Topographic Laboratories, Ft. Belvoir, Va., Report ETL-TR-74-5, 1974.

Riordan, P., "Extreme 24-Hour Snowfalls in the United States: Accumulation, Distribution, and Frequency," U.S. Army Engineer Topographic Laboratories, Ft. Belvoir, Va., Special Report ETL-SR-78-4, 1973.

Roach, W.T., "On the Nature of the Summit Areas of Severe Storms in Oklahoma," *Quart. J. Roy. Meteorol. Soc.,* **93:** 318–336, 1967.

Rogers, J.W., A.T. Stair, T.C. Degges, C.L. Wyatt, and K.D. Baker, "Rocketborne Measurement of Mesospheric H_2O in the Auroral Zone," *Geophys. Res. Lett.,* **4:** 366–368, 1977.

Roys, G.P. and E. Kessler, "Measurements by Aircraft of Condensed Water in Great Plains Thunderstorms," NSSL Tech. Note 49, ESSA, U.S. Dept. of Commerce, 1966.

Ryan, R.T., H.H. Blau, P.C. Von Thuna, M.L. Cohen, and G.D. Roberts, "Cloud Microstructure as Determined by an Optical Cloud Particle Spectrometer," *J. Appl. Meteorol.,* **11:** 149–156, 1972.

Schilling, G.F., "Theoretically Permissible Altitudes and Seasons for the Occurrence of Clouds Near the Mesopause," Rand Corp. Paper P-2899, AD435637, 1964.

Schlatter, E. and M. Lefkowitz, "Evaluation of Multi-Transmisometer Systems," RD-68-49, ESSA-Weather Bureau, Atlantic City, N.J., 1968.

Shanklin, M.D. and J.B. Landwehr, "Photogrammetrically Determined Cloud-Free Lines-of-Sight at Columbia, Mo.," Final Report under Contract F19628-68-C-0140, University of Missouri, AFCRL TR-71-0273 AD725758, 1971.

Scholz, T.G., D.H. Ehhalt, L.E. Heidt, and E.A. Martell, "Water Vapor, Molecular Hydrogen, Methane, and Tritium Concentrations Near the Stratopause," *J. Geophys. Res.,* **75:** 3049–3054, 1970.

Sims, A.L. and D.M.A. Jones, "Climatology of Instantaneous Precipitation Rates," AFCRL TR-73-0171, AD760785, March 1973.

Sissenwine, N. and R. Cormier, "Synopsis of Background Material for MIL-STD-210B, Climatic Extremes for Military Equipment," AFCRL-TR-74-0056, AD780508, 1974.

Soberman, R.K., "Noctilucent Clouds," *Sci. Am.,* pp 51–59, June 1963.

Somerville, P.N., and S.J. Bean, "A New Model for Sky Cover," AFGL-TR-79-0219, ADA078368, 1979.

Somerville, P.N., S.J. Bean, and S. Falls, "Some Models for Visibility," AFGL-TR-79-0144, ADA075490, 1979.

Stickel, P.G., and T.A. Seliga, "Cloud Liquid Water Content Comparisons in Rain Using Radar Differential Reflectivity Mesurements and Aircraft Measurements," *Preprints 10th Conference Radar Meteorology,* American Meteorol. Society, Boston, 30 Nov-3 Dec 1981.

Sulakvelidze, G.K., N.Sh. Bibilashvili, and V.F. Lapcheva, "Formation of Precipitation and Modification of Hail Process," Gidrometeorologicheskoe Izdatel'-stvo, Leningrad, Translation by Israel Program for Scientific Translations, Tel-Aviv (No. 1806) 1967.

Suring, R., *Die Wolken,* 2nd Ed., Leipzig, 1941.

Taljaard, J.J., H. vanLoon, H.L. Crutcher, and R.L. Jenne, *Climate of the Upper Air—Southern Hemisphere, Vol. 1, Temperatures, Dew Points and Heights Selected Levels,* U.S. Dept. of Commerce, ESSA, Environmental Data Service, NAVAIR 50-IC-55, 1969.

Tattelman, P., "An Objective Method for Measuring Surface Ice Accretion," *J. Appl. Meteorol.,* **21:** 153–166, 1982.

Tattelman, P. and D.D. Grantham, "A Survey of Techniques for Estimating Short-Duration Precipitation Rate Statistics," AFGL-TR-82-0357, ADA125705, 1982.

Tattelman, P. and I.I. Gringorten, "Estimated Glaze Ice and Wind Loads at the Earth's Surface for the Contiguous United States," AFCRL-TR-73-0646, AD775068, 1973.

Tattelman, P. and K. Scharr, "A Model for Estimating 1-Minute Rainfall Rates," *J. Climate Appl. Meteorol.,* **22:** 1575–1580, 1983.

Thornwaite, C.W., J.R. Mather, D.B. Carter, and C.E. Molineux, "Estimating Soil Moisture and Tractionability Conditions for Strategic Planning," AFCRC TN-58-201 (1 and 2), AD146789, 1958.

U.S. Dept. of Defense, "Military Standard Climatic Extremes for Military Equipment," *MIL-STD-210B,* U.S. Government Printing Office, 1973.

U.S. Weather Bureau, "Rainfall Intensity-Duration-Frequency Curves," Tech. Paper 25, 1955.

U.S. Weather Bureau, *Determination of Snow Loads for Building Construction,* Div. of Climatological and Hydrological Services, Washington, D.C., 1951.

Varley, D.J., I.D. Cohen, and A.A. Barnes, "Cirrus Particle Distribution Study, Part 7," AFGL-TR-80-0324, ADA100269, 1980.

Waters, J.W., J.J. Gustincic, R.K. Kakar, A.R. Kerr, H.K. Roscoe, and P.N. Swanson, "The Microwave Limb Sounder Experiment: Observations of Stratospheric and Mesospheric H_2O in Interhemispheric Survey of Minor Upper Atmospheric Constituents during October-November 1976," NASA Tech. Memo TMX 73630, 1977.

Weiss, R.R., J.D. Locatelli, and P.V. Hobbs, "Simultaneous Observations of Cloud and Precipitation Particles with Vertically Pointing X-Band and K_a-Band Radars," *IEEE Trans. Geosci. Electr., V,* **GE-17:** 151, 1979.

Winner, D.C., "Climatological Estimates of Clock-Hour Rainfall Rates," Air Weather Service Tech. Rept. 202, 1968.